Spectroscopic and Electronic Structure Studies of *met*-Hemerythrin Model Complexes: A Description of the Ferric−Oxo Dimer Bond

Carl A. Brown,[†] Glenn J. Remar,[‡] Ronald L. Musselman,[‡] and Edward I. Solomon*[,†]

Departments of Chemistry, Stanford University, Stanford, California 94305, and Franklin and Marshall College, Lancaster, Pennsylvania 17604

Received November 1, 1994[⊗]

A combination of theoretical and spectral techniques have been used to probe the electronic structure of μ-oxo non-heme Fe dimer complexes which model the active site found in the oxygen carrier hemerythrin. Variable temperature electronic absorption (including single crystal polarized and orientationally averaged), variable temperature magnetic circular dichroism (MCD), and variable temperature resonance Raman spectroscopies have been used to assign all of the spectral features present in these complexes. These spectral studies are complemented by both high spin and broken symmetry SCF−Xα−SW calculations. Together, a description of the highly covalent bonding in these complexes has been generated. The unique UV/vis absorption spectra of the Fe−oxo dimer unit is dominated by low energy intense oxo → Fe^{3+} ligand to metal charge-transfer (LMCT) transitions. These transitions appear at much lower energy than expected due to the presence of very large excited-state antiferromagnetic exchange in the LMCT transitions from the bridging oxo group. The different spin components of these oxo LMCT transitions can be identified from their large temperature dependence exhibited in the different spectroscopies listed above. The observed excited state splittings have been analyzed using a recently developed valence bond configuration interaction (VBCI) model to describe this bridging-ligand charge-transfer excited-state antiferromagnetism and probe specific superexchange pathways in the ground and excited states. This VBCI model indicates an inverted charge-transfer ordering scheme with the in the Fe(III)−O−Fe(III) plane π CT transition lowest in energy. The low energy of these transitions and the high covalency of the Fe(III)−O−Fe(III) bond are also sources of the higher intensity of the ligand field transitions relative to those of monomeric Fe^{3+} complexes. The ligand field excited-state splitting for the $^6A_1 \rightarrow {}^4A_1$ transition, which is ferromagnetic, is analyzed using the Tanabe model of exchange and demonstrates the importance of a mixed π/σ (Fe d_{yz} − Fe d_{z^2}) magnetic exchange pathway. The nature of the Fe−oxo bond in the Fe(III)−O−Fe(III) unit is analyzed and its strength is mainly due to strong σ bonding interactions of the oxo p_z orbital with the 4s and 4p orbitals of the iron. The high stability of the μ-oxo iron dimer bond provides significant insight into differences in the O_2 reactivity among the different binuclear non-heme proteins hemerythrin, methane monooxygenase, and ribonucleotide reductase.

Introduction

The binuclear ferric μ-oxo unit plays a major role in the oxygen reactivity of non-heme iron protein and enzyme systems. These include hemerythrin (Hr), an oxygen transport protein which is found in a number of marine invertebrates, ribonucleotide reductase (RDPR), which converts ribonucleotides to deoxyribonucleotides in DNA synthesis, and methane monooxygenase (MMO), which catalyzes the hydroxylation of methane to methanol in methanotropic bacteria. Hr is the best characterized binuclear non-heme iron protein. The presence of an oxo bridge in its active site, which was initially suggested from spectroscopic analysis,[1,2] was confirmed by the crystal structure of the met (Fe^{3+}−Fe^{3+}) site.[3] This crystal structure of Hr showed that the two Fe(III) ions in the active site are six and five coordinate and bridged by one oxo bridge and two carboxylato (from the glutamates) bridges (Chart 1). The remaining ligation in this structure involves nitrogen (histidine) coordination. The Fe−O−Fe angle is bent at an angle of 135° due to the tribridged structure. The open coordination site on the five-coordinate Fe is labeled X in Chart 1. Exogenous ligands can bind to this coordinatively unsaturated site,[4] and it is at this position (X) that dioxygen resides as peroxide in the oxygenated form of Hr (oxyHr). Single-crystal polarized electronic absorption studies and resonance Raman (rR) studies have shown that the peroxide binds asymmetrically as hydroperoxide[5−8] which appears to hydrogen bond to the oxo bridge.[6,7]

X-ray crystallography and resonance Raman spectroscopy have also shown that the Fe−oxo dimer unit is present in the met form of RDPR[9,10] (Chart 1). However, there are some structural differences between metHr and RDPR. In RDPR, each Fe is six-coordinate and there are only two bridges, one oxo and one carboxylato (from the bridging glutamate). There is also only one nitrogen (histidine) bound to each Fe, and the remaining ligation is oxygen based (water, glutamates, or

[†] Stanford University.
[‡] Franklin and Marshall College.
[⊗] Abstract published in *Advance ACS Abstracts,* December 15, 1994.

(1) Freier, S. M.; Duff, L. L.; Shriver, D. F.; Klotz, I. M. *Arch. Biochem. Biophys.* **1980**, *205*, 449−463.
(2) Schugar, H. J.; Rossman, G. R.; Barraclough, C. G.; Gray, H. B. *J. Am. Chem. Soc.* **1972**, *94*, 2683−2690.
(3) Stenkamp, R. E.; Sieker, L. C.; Jensen, L. H. *J. Am. Chem. Soc.* **1984**, *106*, 618−622.
(4) Garbett, K.; Darnall, D. W.; Klotz, I. M.; Williams, R. J. P. *Arch. Biochem. Biophys.* **1969**, *135*, 419−434.
(5) Kurtz, D. M., Jr.; Shriver, D. R.; Klotz, I. M. *J. Am. Chem. Soc.* **1976**, *106*, 2437−2443.
(6) Shiemke, A. K.; Loehr, T. M.; Sanders-Loehr, J. *J. Am. Chem. Soc.* **1984**, *106*, 4951−4956.
(7) Shiemke, A. K.; Loehr, T. M.; Sanders-Loehr, J. *J. Am. Chem. Soc.* **1986**, *108*, 2437−2443.
(8) Gay, R. R.; Solomon, E. I. *J. Am. Chem. Soc.* **1978**, *100*, 1972−1973.
(9) Sanders-Loehr, J. In *Iron Carriers and Iron Proteins*; Loehr, T. M., Ed.; VCH Press: New York, 1989; pp 373−466.
(10) Nordlund, P.; Sjöberg, B.-M.; Eklund, H. *Nature* **1990**, *345*, 593−598.

0020-1669/95/1334-0688$09.00/0

Chart 1

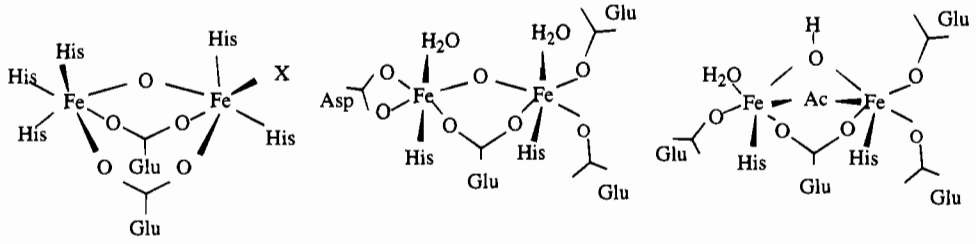

metHr metRDPR metMMOH

aspartates). In RDPR, the binuclear ferrous site reacts with O_2 to form both the oxo-bridged ferric site and a tyrosine radical which is involved in protein reactivity.[11]

In contrast, MMO, whose hydroxylase component (MMOH) contains a binuclear iron site, does not possess an oxo bridge at the met level.[12] A recent crystal structure of the hydroxylase (Chart 1) indicates that the ligand environment of MMOH is more similar to RDPR than Hr, particularly with a greater oxygen coordination.[13,14] As in RDPR, there are only two bridging ligands, one carboxylato and an oxygen based bridge which is assumed to be a hydroxo, since a hydroxo bridge has been shown to be present in the Fe(II)−Fe(III) form.[15,16] The additional acetate (Ac) bridge observed in the structure likely arises from the crystallization buffer.[13] There is also only one nitrogen (histidine) per iron with the remaining ligands oxygen based. In MMOH, the binuclear ferrous site reacts with O_2 to give a high valent oxo intermediate (Compound Q) which oxygenates substrate.[17] Other binuclear non-heme iron systems which may have an Fe-oxo dimer unit, but are less well characterized, include the stearoyl acyl carrier protein Δ-9-desaturase,[18] purple acid phosphatase,[19,20] and ruberythrin.[21]

In order to probe the electronic structure of these binuclear non-heme iron protein systems, a number of spectroscopic studies have been performed (see refs 9 and 22 and references therein). These have shown that the ferric oxo dimer unit in metHr and metRDPR has distinctive spectral features. Among these are low energy oxo → Fe^{3+} charge transfer (CT) transitions and intense ligand field (LF) or d → d transitions.[4,23,24] Intense LF transitions are unexpected because LF transitions in high spin Fe^{3+} monomers are all spin forbidden; i.e., one of the five unpaired electrons of the high spin $S = {}^5/_2$ ground state must flip upon excitation. In addition, the charge transfer transitions from oxygen-based ligands in Fe^{3+} monomers are usually observed to much higher energy.[25] Since the features observed in the protein sites are not present in mononuclear ferric systems, they must be due to the unique electronic structure of the dimeric unit. In addition to excited state spectral studies, the ground state properties of these systems have also been probed.[9,22] Upon formation of the dimer, the ground state splits into six total spin states due to antiferromagnetic exchange coupling between two $S = {}^5/_2$ monomers to give $S_{Tot} = 0, 1, 2, 3, 4, 5$ states. The splitting is described by the ground state J^{GS} of the phenomenological spin Hamiltonian, $H = -2J^{GS}S_A \cdot S_B$. In the oxo-bridged proteins, the J^{GS} value is on the order of -100 cm^{-1} which gives a singlet−triplet splitting of 200 cm^{-1}. A value of -108 cm^{-1} has been reported for RDPR[26] and -134 cm^{-1} for Hr.[27] MMOH has a value (~ -7 cm^{-1}) considerably lower due to the presence of a hydroxo instead of an oxo bridge.[28]

As a complement to protein studies, the synthesis and characterization of synthetic model systems has been an area of active study. Early attempts at modeling the μ-oxo binuclear non-heme iron site involved monooxo-bridged species.[29] After the crystal structure determination of Hr, inorganic complexes that contained the μ-oxo, μ-bis(carboxylato) bridging moieties found in Hr were synthesized.[30,31] These complexes consist of two 6-coordinate Fe^{3+} atoms with three nitrogen based ligands per Fe in conjunction with the oxygen based bridging ligands. To date there are a large number of synthetic non-heme iron model complexes available with varying ligation and bridging moieties. A recent review of these complexes is given in ref 32. The advantage of these synthetic models is that they not only reproduce the structural features of the protein active sites but also offer higher spectral resolution than the proteins.

The first detailed spectral study of an iron oxo dimer model complex focused on the singly bridged $(FeHEDTA)_2O$ complex.[2] In this study two important observations were made about Fe oxo dimers: the increased intensity of the LF transitions and the existence of high energy "dimer" bands not present in monomer spectra. The high energy intense transitions in the absorption spectrum were assigned as simultaneous pair excita-

(11) Bollinger, J. M.; Edmondson, D. E.; Huynh, B. H.; Filley, J.; Norton, J. R.; Stubbe, J. *Science* **1991**, *253*, 292−298.
(12) DeWitt, J. G.; Bentsen, J. G.; Rosenzweig, A. C.; Hedman, B.; Green, J.; Pilkington, S.; Papaefthymiou, G. C.; Dalton, H.; Hodgson, K. O.; Lippard, S. J. *J. Am. Chem. Soc.* **1991**, *113*, 9219−9235.
(13) Rosensweig, A. C.; Frederick, C. A.; Lippard, S. J.; Nordlund, P. *Nature* **1993**, *366*, 537−543.
(14) Nordlund, P.; Dalton, H.; Eklund, H. *FEBS Lett.* **1992**, *307*, 257−262.
(15) DeRose, V. J.; Liu, K. E.; Kurtz, D. M., Jr.; Hoffman, B. M.; Lippard, S. J. *J. Am. Chem. Soc.* **1993**, *115*, 6440−6441.
(16) Thomann, H.; Bernardo, M.; McCormick, J. M.; Pulver, S.; Andersson, K. K.; Lipscomb, J. D.; Solomon, E. I. *J. Am. Chem. Soc.* **1993**, *115*, 8881−8882.
(17) Lee, S.-K.; Fox, B. G.; Froland, W. A.; Lipscomb, J. D.; Münck, E. *J. Am. Chem. Soc.* **1993**, *115*, 6450−6451.
(18) Fox, B. G.; Shanklin, J.; Somerville, C.; Münck, E. *Proc. Natl. Acad. Sci. U.S.A.* **1993**, *90*, 2486−2490.
(19) Que, L., Jr.; Scarrow, R. C. In *Metal Clusters in Proteins*; Que, L., Jr., Ed.; American Chemical Society: Washington, DC, 1988; pp 152−178.
(20) Antanaitis, B. C.; Aisen, P. In *Frontiers in Bioinorganic Chemistry*; Xavier, A. V., Ed.; VCH: New York, 1986; pp 481−493.
(21) LeGall, J.; Prickril, B. C.; Moura, I.; Xavier, A. V.; Moura, J. J. G.; Huynh, B.-H. *Biochemistry* **1988**, *27*, 1636−1642.
(22) Que, L., Jr.; True, A. E. In *Prog. Inorg. Chem.*; Lippard, S. J., Ed.; John Wiley & Sons: New York, 1990; Vol. 38, pp 97−200.
(23) Sanders-Loehr, T. M.; Mauk, A. G.; Gray, H. B. *J. Am. Chem. Soc.* **1980**, *102*, 6992−6996.
(24) Reem, R. C.; McCormick, J. M.; Richardson, D. E.; Devlin, F. J.; Stephens, P. J.; Musselman, R. L.; Solomon, E. I. *J. Am. Chem. Soc.* **1989**, *111*, 4688.
(25) Lehmann, G. *Z. Phys. Chem. Neue Folge* **1970**, *72*, 279−297.
(26) Petersson, L.; Gräsślund, A.; Ehrenberg, A.; Sjöberg, B.-M.; Reichard, P. *J. Biol. Chem.* **1980**, *255*, 6706−6712.
(27) Dawson, J. W.; Gray, H. B.; Hoenig, H. E.; Rossman, G. R.; Schredder, J. M.; Wang, R.-H. *Biochemistry* **1972**, *11*, 461−465.
(28) Fox, B. G.; Hendrich, M. P.; Surerus, K. K.; Andersson, K. K.; Froland, W. A.; Lipscomb, J. D.; Münck, E. *J. Am. Chem. Soc.* **1993**, *155*, 3688−3701.
(29) Murray, K. S. *Coord. Chem. Rev.* **1973**, *12*, 1−35.
(30) Armstrong, W. H.; Spool, A.; Papaefthymiou, G. C.; Frankel, R. B.; Lippard, S. J. *J. Am. Chem. Soc.* **1984**, *106*, 3653−3667.
(31) Wieghardt, K.; Pohl, K.; Gebert, W. *Angew. Chem., Int. Ed. Engl.* **1983**, *22*, 737.
(32) Kurtz, D. M., Jr. *Chem. Rev.* **1990**, *90*, 585−606.

tions (SPE). A SPE corresponds to one photon excitation of ligand field transitions on both iron atoms which become allowed due to the exchange interaction. These transitions should occur at the sum of the energies of the individual LF transitions.[33,34] This assignment seemed justified for (FeHEDTA)$_2$O since the high energy bands appeared at the sums of the energies of the assigned ligand field transitions.[2] In subsequent resonance Raman and polarized absorption studies, these features have been reassigned as oxo $\rightarrow$ Fe^{3+} charge transfer (CT) transitions. Resonance Raman studies on other Fe−oxo dimers determined that the intense low energy absorption present in iron−oxo dimers led to enhancement of the Fe−O−Fe symmetric vibration.[30,35,36] Single-crystal polarized absorption on the HEDTA dimer and on metHr derivatives showed that these bands are polarized along the Fe−O vector, as would be predicted for an oxo $\rightarrow$ Fe^{3+} CT assignment, and that they do not correlate in energy to the sum of LF transitions.[24] The observed increased LF intensity in the (FeHEDTA)$_2$O complex was attributed to exchange relaxation of selection rules to overcome the spin forbiddeness of the high spin Fe^{3+} LF transitions. The existence of spin-allowed transitions in dimers is usually attributed to the exchange coupling of a ground state metal ion to the second metal ion in a LF excited state which, for d^5 dimers, leads to a spin manifold of states of $S = 1, 2, 3, 4$. Thus when the $S = 1$ component of the GS is populated, spin allowed transitions are allowed to the $S = 1$ component of the excited state.

The spin manifold of LF excited states of dimeric transition metal complexes are also split in energy due to exchange interactions in the LF excited state, which can lead to the observance of a number of dimeric transitions for each equivalent monomeric transition.[37,38] We have shown that CT excited states of bridging ligands can also undergo large splittings due to excited state antiferromagnetism.[39,40] The analysis of both LF and CT excited state splittings observed in optical spectroscopy is a sensitive probe of individual superexchange pathways in dimeric systems.[38,39,41]

The present study employs a variety of magneto-optical techniques (single crystal polarized absorption and reflectance, resonance Raman, and magnetic circular dichroism) and theoretical methods (SCF−Xα−SW) to develop a detailed description of the electronic structure of the iron oxo dimer unit. Two model complexes will be considered in detail, [$Fe_2O(O_2CCH_3)_2(Me_3TACN)_2$], a tribridged structure (Fe−O−Fe angle = 120°) which models the coordination found in Hr,[31] and the singly bridged complex [(FeHEDTA)$_2$O] that is more linear with an Fe−O−Fe angle of 165°[2] (Figure 1). An important aspect of this work is the striking temperature dependence of the spectral features which allows definitive spectral assignments. The absorption spectra of each complex has been divided into three energy regions and the spectroscopic results of each energetic region is presented in the Experimental Results section.

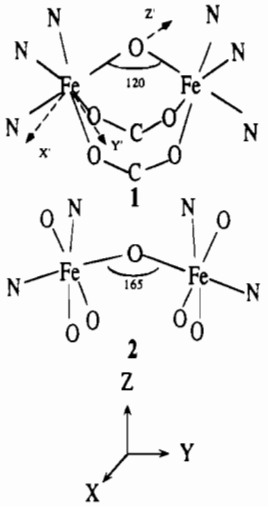

Figure 1. Core atoms and coordinate frame for the tribridged (**1**) and monobridged (**2**) structures. The molecular coordinate frame has *Z* bisecting the Fe−O−Fe angle and the Fe−Fe vector along *Y*. Also included on structure **1** is a coordinate frame used to describe each monomeric unit with *Z'* along the Fe−O bond and *X'* and *Y'* bisecting the other metal−ligand bonds.

The results of the SCF−Xα−SW calculations are then presented. The analysis is divided into three sections: section I addresses the source of intensity of the LF transitions, section II presents the analysis of the LF excited state exchange splittings, and section III concerns the analysis of the CT transitions. Most of the emphasis is placed on the latter section since the CT bands are shown to provide fundamental insight into the iron−oxo dimer bond, the magnetism present in these systems, the effect of perturbations on the Fe−O−Fe bond, and its contributions to reactivity in different binuclear non-heme iron proteins.

Experimental Section

The ClO_4^- salt of [$Fe_2O(O_2CCH_3)_2(Me_3TACN)_2$] (**1**) was prepared according to literature procedures.[42] Dark brown crystals suitable for spectroscopy were obtained (up to 3 mm × 3 mm) by recrystallization in methanol with slow evaporation of solvent (2−3 days). This compound crystallizes in the orthorhombic space group Amam with four symmetry related molecules per unit cell.[42] The dimeric unit has crystallographically defined C_{2v} symmetry with all Fe−Fe vectors parallel, which is ideal for polarized spectroscopy. The molecular coordination system is defined with *z* along the C_{2v} axis {010}, *y* along the Fe−Fe axis {001}, and *x* along the {100} axis (Figure 1). Faces were indexed using a Huber optical two-circle reflection goniometer and by Weissenberg photography. Both (100) and (010) are naturally occurring faces which allow for a complete determination of *x*, *y*, and *z* molecular polarizations. In the (100) face, the two extinction directions are along *y*, dark brown, and *z*, light brown. In the (010) face, the two extinction directions are along *y*, dark brown, and *x*, light green.

Single crystals of (FeHEDTA)$_2$O (**2**) were grown as described previously.[2] The core atoms of this complex are given in Figure 1, using the same coordinate system as **1**. With the Fe−Fe vector aligned along *a**, significant polarization information can also be obtained with these monoclinic crystals ($P2_1/c$). In the hexagonal (001) face, the orange and red directions were used for polarization measurements with the following projections.

$$I_{\{100\}} = I_{red} = 0.037I_x + 0.962I_y + 0.005I_z$$

(33) Dexter, D. L. *Phys. Rev.* **1962**, *126*, 1962.
(34) Schugar, H. J.; Solomon, E. I.; Cleveland, W. L.; Goodman, L. *J. Am. Chem. Soc.* **1975**, *97*, 6442−6450.
(35) Czernuszewicz, R. S.; Sheats, J. E.; Spiro, T. G. *Inorg. Chem.* **1987**, *26*, 2063−2067.
(36) Sanders-Loehr, J.; Wheeler, W. D.; Shiemke, A. K.; Averill, B. A.; Loehr, T. M. *J. Am. Chem. Soc.* **1989**, *111*, 8084−8093.
(37) McCarthy, P. J.; Güdel, H. U. *Coord. Chem. Rev.* **1988**, *88*, 69−131.
(38) Ferguson, J.; Guggenheim, H. J.; Tanabe, Y. *J. Phys. Soc. Jpn.* **1966**, *21*, 692−704.
(39) Tuczek, F.; Solomon, E. I. *Inorg. Chem.* **1993**, *32*, 2850−2862.
(40) Pate, J. E.; Ross, P. K.; Thamann, T. J.; Reed, C. A.; Karlin, K. D.; Sorrell, T. N.; Solomon, E. I. *J. Am. Chem. Soc.* **1989**, *111*, 5198−5209.
(41) Ross, P. K.; Allendorf, M. D.; Solomon, E. I. *J. Am. Chem. Soc.* **1989**, *111*, 4009−4021.
(42) Hartman, J. R.; Rardin, R. L.; Chaudhuri, P.; Pohl, K.; Wieghardt, K.; Nuber, B.; Weiss, J.; Papaefthymiou, G. C.; Frankel, R. B.; Lippard, S. J. *J. Am. Chem. Soc.* **1987**, *109*, 7387−7396.

$$I_{\{010\}} = I_{\text{orange}} = 0.072I_x + 0.005I_y + 0.934I_z \quad (1)$$

Experiments were also performed on single crystals of $[Fe_2O(O_2CCH_3)_2TACN)_2]$, **3**, which were grown as described previously.[43] The same coordinate frame as **1** is used for **3** (Figure 1) since the core atoms are identical in these complexes. Recrystallizing in CH_3CN with slow evaporation over 1−2 days resulted in crystals large enough for optical measurements. These crystals are tetragonal ($I4_1cd$) with the {001} direction along the molecular *z*-axis and have rigorous C_2 site symmetry.[43] Experiments were performed on the (100) face with the following projections of the molecular directions onto the dielectric directions.

$$I_{\{010\}}(\text{molecule 1}) = 0.712I_x + 0.289I_y + 0.00I_z$$

$$I_{\{010\}}(\text{molecule 2}) = 0.289I_x + 0.712I_y + 0.00I_z$$

$$I_{\{001\}}(\text{molecule 1}) = 0.000I_x + 0.000I_y + 1.00I_z$$

$$I_{\{001\}}(\text{molecule 2}) = 0.000I_x + 0.000I_y + 1.00I_z \quad (2)$$

For optical experiments, single crystals of **1** were mounted on quartz disks with phenyl salicylate and hand polished with 9 μm grit polishing paper. (Note these perchlorate salts were found to be heat sensitive and resins requiring sample heating could not be used.) Thicknesses down to 30 μm were obtained by hand polishing. The crystals were washed with toluene and then mounted on quartz disks with grease and masked off with Apiezon Q. For **2**, crystals were mounted using epoxy, and thicknesses down to ~5 μm were obtained using a homemade crystal polishing apparatus. These were mounted as described for **1**. Crystals were aligned with a Vickers polarizing microscope. Glass spectra of **1** were obtained in 2:1 mixtures of ethylene glycol/water, while those of **2** were obtained in a saturated LiCl aqueous solution.[2] Mull spectra were obtained by grinding the compound with an agate mortar and pestle, mixing with polyvinyl siloxane or mineral oil, and placing between two quartz disks.

All single-crystal and some mull/glass absorption measurements were obtained with a MacPherson RS-10 double beam spectrophotometer with modified optics for single-crystal spectroscopy which has been computer interfaced for control and data acquisition. The spectrometer is equipped with a MacPherson Model 2051 1-m monochromator and a Janis Varitemp helium cryostat. A pair of Glan-Taylor polarizers matched from 200 nm to 2.5 μm were used for single-crystal measurements. Three gratings blazed at 3000 Å, 7500 Å, and 1.25 μm were used to cover the spectral region of interest. Detectors used were an extended S-20 photomultiplier tube (2200−8000 Å), a dry-ice cooled S-1 tube (5000−10000 Å), and a Joule−Thompson cooled PbS detector (8500 Å to 2.5 μm). The last detector used a chopped light source and lock-in amplifier. Variable temperature solution spectra were also obtained on an Olis-driven Cary 17 spectrophotometer with the Janis Varitemp cryostat. MCD spectra were taken on a Jasco J500-C spectropolarimeter with Oxford Instruments SM-4: 6 or 7 T superconducting magnets/cryostats.

For resonance Raman experiments, crystals of **1** were ground in an agate mortar and pestle, mixed with K_2SO_4 as an internal standard, and placed in quartz tubes. The room temperature samples were spun to avoid local heating, and the 77 K data were obtained by using a quartz finger dewar with the sample immersed in liquid nitrogen. Spectra were taken with a Spex 1403 double monochromator and a cooled RCA C31034A photomultiplier combined with a Spex digital photometer system or a Princeton Applied Research Model 1455A intensified diode array detector with a Model 1461 OMA interface. A backscattering geometry was used to collect scattered light. Decomposition of samples occurred with a UV laser source, and when this was observed the data were not used.

Polarized, single crystal, specular reflectance spectra were taken along the crystallographic axes of the (010) face of **1**, on the (001) face of **2**, and the (100) face of **3**. The instrument, based on a concept by Anex,[44] is a grating microspectrophotometer consisting of tungsten−halogen and xenon arc light sources, an Instrument SA HR320 0.32-m computer controllable grating monochromator, a Glan−Thompson polarizer, a double-beam reflecting microscope, and a photomultiplier detector. Signal detection is through two Princeton Applied Research 186A lock-in amplifiers, and the instrument is controlled by an Apple IIe computer. Data for each spectral point are collected until the sample mean has a 99% probability of being within 1% of the population mean. The data are then uploaded to a HP 3000 computer for processing. Reflectance is measured relative to a NIST standard second-surface mirror, and Kramers−Kronig transformation of the average of at least three reflectance spectra is performed to obtain standard absorbance values. An effective transition is added in the vacuum-UV region to provide the reflectivity necessary for proper base line behavior throughout the experimental region upon transformation. This adjustment does not affect the energies of the transformed bands, but may affect intensities.

The 1982 QCPE version of the SCF−Xα−SW program[45] was used for the electronic structure calculations. Two calculations were performed, one on a tribridged structure based on **1** with the acetates replaced by formates and NH_3 molecules replacing the Me_3Tacn nitrogen ligands and one on a linear model based on **2** with NH_3 and H_2O molecules replacing the HEDTA ligation. The coordinates of the non-hydrogen atoms of $[(NH_3)_6(O_2CH)_2Fe_2]O$, hereafter designated **1′**, were taken directly from the crystallographic coordinates of **1**, which has C_{2v} symmetry.[42] The coordinates of $[(NH_3)_3(H_2O)_2Fe]_2O$, hereafter designated **2′**, were obtained by using the bond distances of **2** and idealizing the geometry to give octahedral coordination for each side of the dimer with overall C_{2v} symmetry and a linear Fe−O−Fe unit.

Input parameters, including atomic positions, sphere radii and α values for **1′** and **2′** are given as Supplementary Material (Table S1). The calculations were considered to be converged when the largest deviation in the potential between iterations was less than 1×10^{-4}. The α values for the atoms are those determined by Schwarz[46] and those for the inter and outer sphere are weighted by the number of valence electrons. Calculations were performed using averages of Norman radii for the non-metal atoms. The sphere radii for the metal were increased to 2.80 for both **1′** and **2′** to correct for the tendency of the Norman criteria to overestimate the covalency of the metal ion.[47] Spin unrestricted broken symmetry calculations were performed on both structures according to the procedure of Noodleman.[48]

Results

Experimental Results. The 300 and 10 K absorption spectra of **1** and **2** are given in Figure 2. Figure 2B reproduces data obtained previously.[2] These spectra have been divided into three regions with varying intensities and temperature dependencies. Each of these regions will be considered in detail in order of increasing energy and specific assignments will be presented. The most striking features are the intense, low energy bands and their large temperature dependence, particularly in region II. In Figure 2A for **1**, most bands decrease in intensity or disappear altogether upon cooling, except for the most intense peak at 21 000 cm^{-1} which almost doubles in intensity at 10 K. For structure **2** (Figure 2B), the intensity at 21 000 cm^{-1} decreases with decreasing temperature while the band at 24 500 cm^{-1} increases in intensity at low temperature. Also in Figure 2B, the features in region III show variable temperature dependence.

This striking temperature dependence can be understood qualitatively in terms of dimer exchange interactions. Upon formation of the dimer, the ground state splits into six total spin states due to antiferromagnetic coupling between two $S = {}^5/_2$

(43) Spool, A.; Williams, I. D.; Lippard, S. J. *Inorg. Chem.* **1985**, *24*, 2156−2162.
(44) Anex, B. G. *Mol. Cryst.* **1966**, *1*, 1−36.
(45) Cook, M.; Case, D. A *QCPE Program 465* **1991**, *23*, 21−22.
(46) Schwarz, K. *Phys. Rev. B* **1972**, *5*, 2466−2469.
(47) Ross, P. K.; Solomon, E. I. *J. Am. Chem. Soc.* **1991**, *113*, 3246−3259.
(48) Noodleman, L. *J. Chem. Phys.* **1981**, *74*, 5737−5743.

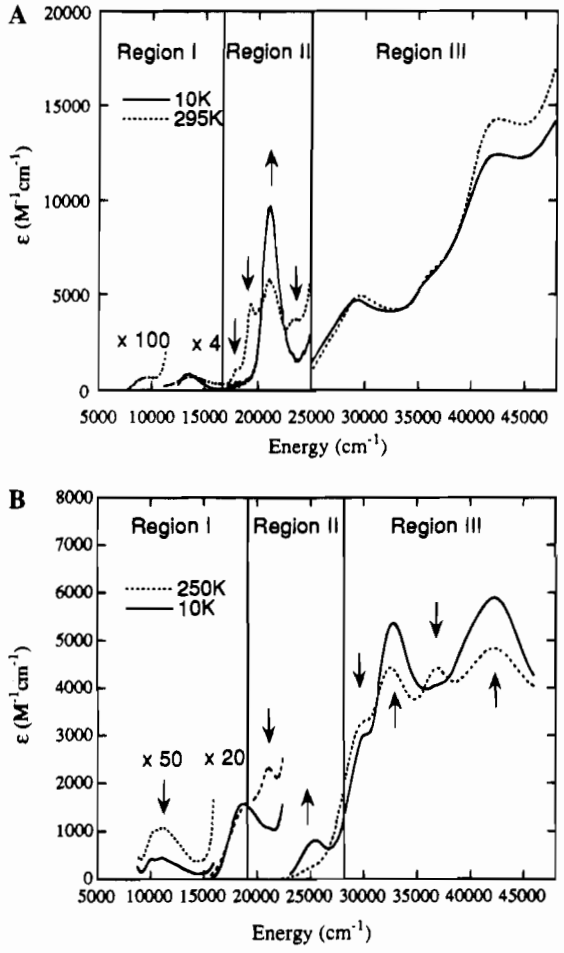

Figure 2. Glass spectra (10 and 300 K) for **1** (A) and **2** (B). The ϵ scale corresponds to the features in region III, and the features in the other two regions have been scaled as indicated. Arrows indicate the change in intensity with decreasing temperature.

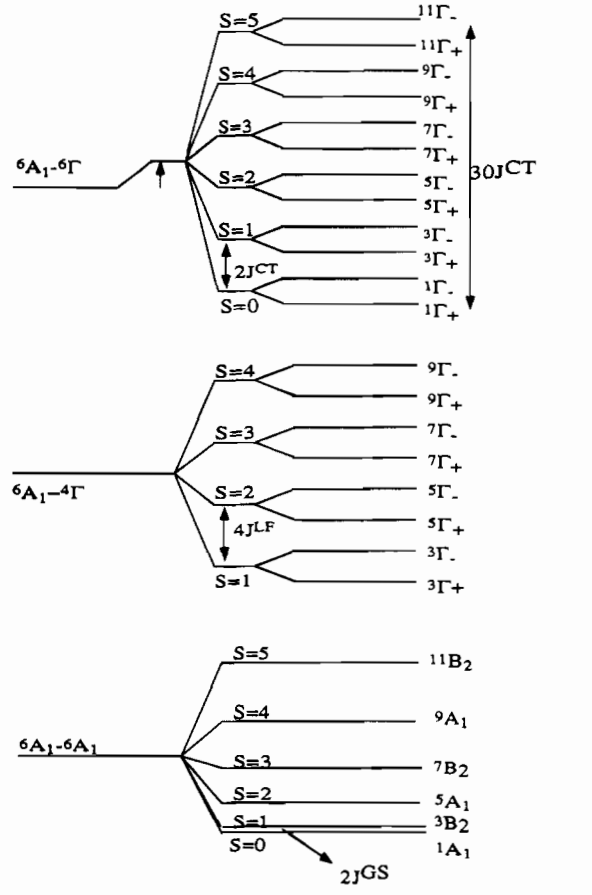

Figure 3. Energy level diagrams giving the GS and excited state ligand field (LF) and charge transfer (CT) spin manifolds.

monomers to give the $S_{Tot} = 0, 1, 2, 3, 4, 5$ states of the spin ladder shown in the bottom half of Figure 3. The splitting is governed by the ground state J^{GS} of the phenomenological spin Hamiltonian, $H = -2J^{GS}S_A \cdot S_B$. Also shown in Figure 3 (middle) are the LF excited states of the dimer obtained when one ion undergoes a quartet ligand field transition resulting in a complex that has an $S = {}^5/_2$ (ground state) ion on one side of the dimer and an $S = {}^3/_2$ (excited state) ion on the other side. These spins couple leading to four spin states ($S_{Tot} = 1, 2, 3, 4$) with an energy splitting described by an excited state J^{LF} value. In the excited state, a matrix element exists that can transfer the excitation to the other side of the dimer leading to symmetric (+) and antisymmetric (−) splittings of each spin component in the excited state. This yields a total of eight possible transitions in the dimer for each monomer LF transition. The symmetry of the dimer states depends on the specific single ion excited state denoted by Γ (Figure 3, middle). The top portion of Figure 3 gives the excited states for a spin-allowed CT transition. The excited states are obtained by coupling a $^6\Gamma$ CT state with the $^6A_1$ GS to yield the 12 excited states shown in Figure 3. At low temperature, when only the $S_{Tot} = 0$ component of the GS is populated, there can be spin allowed ($\Delta S = 0$) transitions for CT transitions but not for LF transitions. Both spin allowed LF and CT transitions can be observed from higher populated S_{Tot} states. From a Boltzmann analysis of the ground spin states using a J^{GS} of −120 and −95 cm^{-1} which are the experimentally determined ground state exchange values for **1** and **2**, respectively,[2,42] only the singlet, triplet, and quintet sublevels of the ground state are significantly populated at temperatures of 300 K and only the singlet state is populated at 4 K.

Region I. The polarized single-crystal absorption spectra of the first observed electronic transitions in **1** and **2** are shown in Figure 4 along with their temperature dependencies. Spectra were also taken down to 4000 cm^{-1}, and no additional absorption associated with the dimeric units was observed. Following Gray[2] and Reem,[24] this transition is assigned as the first ligand field transition expected for high spin Fe^{3+}, $^6A_1 \rightarrow {}^4T_1{}^a$. The weak field Tanabe−Sugano diagram[49] for octahedral d^5 can be used to obtain an expected experimental ordering of LF transitions, i.e. $^4T_1{}^a$, $^4T_2{}^a$, $^4A_1$, ^4E, $^4T_2{}^b$ listed in order of increasing energy. Figure 4A demonstrates that the dominant polarization in **1** is along y, which is parallel to the Fe−Fe vector. Weak intensity is observed for the in plane perpendicular polarized or z spectrum, but none is present along x (perpendicular to the Fe−Fe vector and out of the Fe−O−Fe plane). This transition for **1** in Figure 4A can be fit with a minimum of two bands at 7500 and 9750 cm^{-1}; the higher energy component is more intense with $\epsilon = 13$ M^{-1} cm^{-1} at 10 K. The peak along z is broad and featureless with intensity between 7000 and 10 000 cm^{-1}. The 9750 cm^{-1} band appears to be the only temperature dependent feature in either polarization and increases in intensity with increasing temperature. A plot of the temperature dependence of the intensity of this band is shown in the inset and fit to the theoretical Boltzmann population of the $S = 1$ component of the ground state. Note that the intensity follows the population of the $S = 1$ state with small deviations at high temperature. This deviation can be

(49) Tanabe, Y.; Sugano, S. *J. Phys. Soc. Jpn.* **1954**, *9*, 753−766.

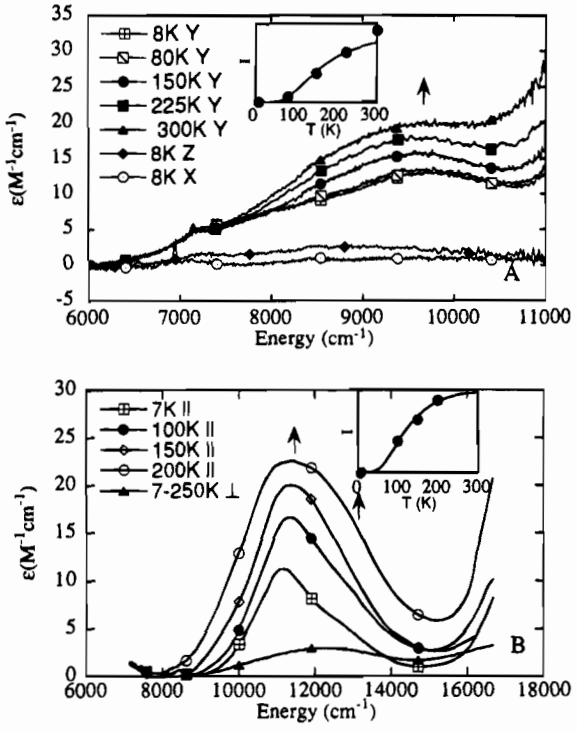

Figure 4. Single crystal polarized data for the $^6A_1 \rightarrow {}^4T_1{}^a$ region of **1** (A) and **2** (B). Inset gives the change in intensity fit to the Boltzmann population of the $S = 1$ component of the ground state.

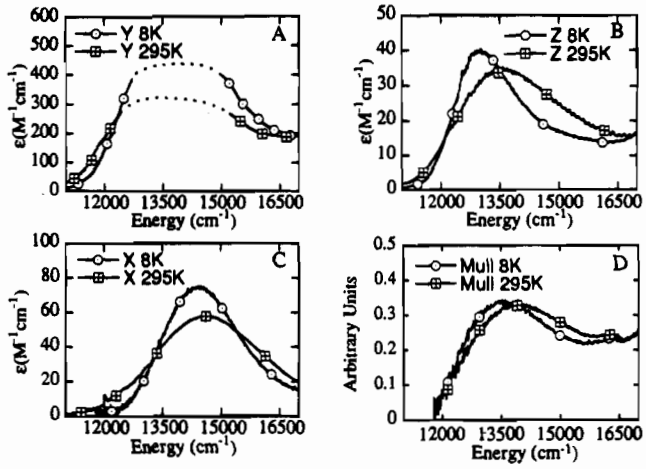

Figure 5. Crystalline absorption data of the $^4T_2{}^a$ region for **1**: *y*-polarized data (A); *z*-polarized data (B); *x*-polarized data (C); orientationally averaged mull data (D). Two spectra corresponding to 8 and 295 K are given in each case. The dotted lines in the spectra of part A indicate the peak is truncated due to stray light effects.

attributed to population of the $S = 2$ state (7.5%) at 300 K. The spectrum of **2** in Figure 4B shows strong parallels with that of **1**. Again most of the intensity is polarized along *y*, with a similar temperature dependence. Two major bands with epsilon values of $\sim$10 M^{-1} cm^{-1} are observed at 11 000 cm^{-1} and 12 100 cm^{-1} from a Gaussian resolution of the spectrum. The splitting of these transitions is smaller than for **1**, and both bands increase in intensity with increasing temperature. A plot of the absorption intensity as a function of temperature is given in the inset of Figure 4B with the fit to the Boltzmann population of a triplet state 190 cm^{-1} above the singlet.[2] The weak temperature-independent intensity, which is perpendicular to the Fe−Fe vector for **2** (predominantly *z*-polarized) appears as a broad band between 9500 and 14 500 cm^{-1}. In summary, the $^6A_1 \rightarrow {}^4T_1{}^a$ transition for both **1** and **2** consists of two parallel polarized bands at 10 K with epsilons of $\sim$10 M^{-1} cm^{-1} and which gain parallel polarized intensity with increasing temperature.

The polarized single crystal spectra for the next higher energy transition in region I for structure **1** are shown in Figure 5A−C at 8 and 295 K. (The corresponding peak in compound **2** is shifted to higher energy and overlaps the bands in region II as will be described later). Similar to the $^6A_1 \rightarrow {}^4T_1{}^a$ transition, the most intense transition is *y* polarized with a lower limit of 450 M^{-1} cm^{-1} for the molar extinction coefficient. Due to the high intensity of the absorption bands, the peak maximum of the parallel polarized band is distorted (i.e. truncated) due to stray light effects. In order to determine the correct shape and temperature dependence of the *y*-polarized peak, the mull spectrum of **1** is given in Figure 5D, which should reflect the parallel polarization that dominates the intensity in this region, and gives a broad peak centered at $\sim$13 500 cm^{-1}. The *z*-polarized spectrum (Figure 5B) shows a lower energy component at $\sim$13 000 cm^{-1} with intensity tailing to higher energy while the *x*-polarized spectrum shows a broad peak centered at $\sim$14 500 cm^{-1}. The transitions observed in *x* and *z* polarization are much weaker with epsilon values at least five times smaller than that observed in the *y* polarization. This region's temperature dependence is less pronounced than that observed for region I. The lower energy component in *z* polarization (Figure 5B) appears to shift intensity to a higher energy component with increasing temperature. This temperature effect is also observed in the mull spectrum given in Figure 5D. The *x*-polarized band at 14 500 cm^{-1} in Figure 5C does not show a significant temperature dependence, only slight broadening with increasing temperature. Since the temperature effects are limited in this region, a quantitative analysis of the temperature dependence has not been performed. On the basis of their low energy, these transitions are assigned as the $^6A_1 \rightarrow {}^4T_2{}^a$ transitions. In summary, these bands are an order of magnitude more intense than the $^6A_1 \rightarrow {}^4T_1{}^a$ transitions, do not show a significant temperature dependence, and vary in energy with Fe−O−Fe angle (i.e. there is a shift to higher energy for compound **2** as has been noted before in Fe−oxo dimers[50]).

Region II. Region II in Figure 2A of **1** dominates the visible absorption spectrum with at least four observable bands (indicated by arrows at 18 000, 19 300, 21 000, and 23 400 cm^{-1}) that show marked intensity variations with temperature. The largest peak at 21 000 cm^{-1} has $\epsilon = 2500$ M^{-1} cm^{-1} at 8 K which decreases to 1500 M^{-1} cm^{-1} at room temperature. The other three peaks are completely eliminated upon cooling to 10 K. The mull data for this region (Figure 6A) is very similar to the absorption spectra in Figure 2 with peaks following the same temperature dependence, but with peak positions shifted from that of the glass/solution spectrum. Note also that there appears to be a shoulder at $\sim$18 500 cm^{-1} in the 8 K mull spectrum.

The polarized single crystal absorption data for this region are presented in Figure 6B−D. The dominant polarization for **1** in region II is *y* (Figure 6B). Again the peak heights are truncated due to stray light effects, and the mull spectrum (Figure 6A) will be used to determine peak positions, shape, and temperature dependence of the predominant *y*-polarized intensity. As described below, there are seven bands required to fit the variable temperature polarized data of **1** in this region. Focusing first on the low temperature data, we observe that the peak energy of the dominant feature in *y* polarization is at 20 500 cm^{-1} (band 4) based on the mull spectrum (Figure 6A). In the 8 K *z*-polarized spectrum in Figure 6C, there are two peaks at 18 400 cm^{-1} (band 2) and 21 500 cm^{-1} (band 5). In the 8 K

(50) Norman, R. E.; Holz, R. C.; Ménage, S.; O'Connor, C. J.; Zhang, J. H.; Que, L., Jr. *Inorg. Chem.* **1990**, *29*, 4629−4637.

Table 1. Polarizations, Energies, and Temperature Dependence of Region II Transitions for **1**

bands	1	2	3	4	5	6	7
energy (cm^{-1})	17 750	18 400	19 100	20 500	21 500	22 000	23 500
polarization	*y*	*z*	*y*, *z*	*y*	*z*	*y*, *z*	*y*, *z*
temp dependence	$S = 2$	$S = 0$	$S = 1$	$S = 0$	$S = 0$	$S = 1$	$S = 2$
assignment	$^4A_1$, ^4E	oxo−CT	$^4A_1$, ^4E	oxo−CT	$^4T_2{}^b$	$^4T_2{}^b$	$^4T_2{}^b$

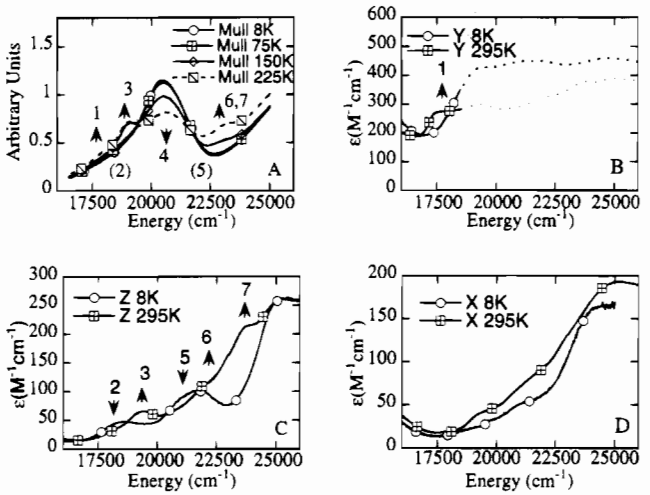

Figure 6. Crystalline absorption data of the $^4A_1$, ^4E region for **1**: the orientationally averaged mull data (A); *y*-polarized data (B); *z*-polarized data (C); *x*-polarized data (D). Four temperatures are shown for the mull and two (8 and 295 K) are given for each polarized spectrum. The dotted lines in (B) indicate that the spectra are truncated due to stray light effects. The seven identifiable bands are labeled numerically according to energy.

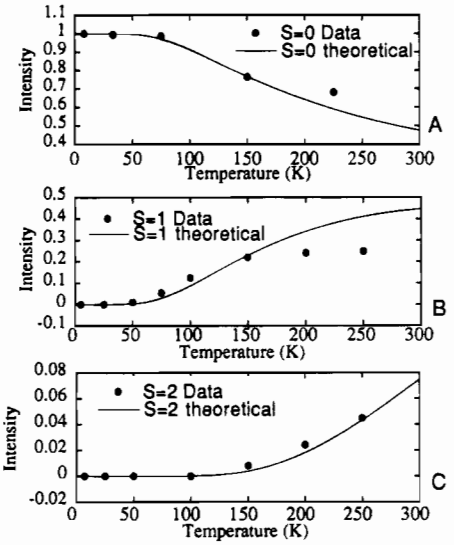

Figure 7. Boltzmann population fits to the intensity of the variable temperature absorption spectra of band 4 (A), band 3 (B), and band 1 (C) in Figure 6 which corresponds to transitions originating from the $S = 0$, $S = 1$, and $S = 2$ components of the ground state, respectively.

x-polarized low temperature spectrum (Figure 6D) there is a featureless rise in intensity to higher energy with no discernible peaks. As the temperature is increased, band 4 at 20 500 cm^{-1} in Figure 6A (mull) loses intensity as do bands 2 and 5 (Figure 6C). Also as the temperature is increased, a new peak starts growing in at ~17 750 cm^{-1} (band 1) in the *y* polarization (Figure 6B). The behavior of the rest of the parallel polarized *y* spectrum is inferred from the mull spectrum in Figure 6A, where at least two bands appear with increasing temperature at ~19 100 cm^{-1} (band 3) and 23 250 cm^{-1} (bands 6 and 7). A band at 19 400 cm^{-1} also appears in the *z*-polarized spectrum in Figure 6C which correlates with band 3 and is at approximately the same energy in the mull. Intensity also increases at 23 000 cm^{-1} in *z* polarization, but consists of two peaks at ~22 000 cm^{-1} (band 6) and ~23 500 cm^{-1} (band 7). While some intensity increases with temperature in the *x*-polarized spectrum (Figure 6D), no clear features are resolved. Table 1 gives the energies of the seven observed transitions, their polarizations, and their temperature dependencies (see below).

Fits of the intensities of bands 1, 3 and 4 to the Boltzmann population of total spin components of the GS are shown in Figure 7. They follow the temperature dependencies expected for transitions involving the $S = 2$, $S = 1$, and $S = 0$ components of the exchange split ground state, respectively (Figure 3). The discrepancy from the theoretical curves can be attributed to overlap of the large number of bands in this region. Quantitative fits could not be performed on bands 2 and 5 due to their low intensity and overlap with other bands, but based on their intensity at low temperature they must also originate from the singlet ground state. Bands 6 and 7 also gain intensity with increasing temperature ($S > 0$), but their association with a specific spin component of the ground state cannot be made from the absorption data.

The variable temperature MCD data for **1** are shown in Figure 8A,B. There are two temperature independent *B*-terms at 18 500

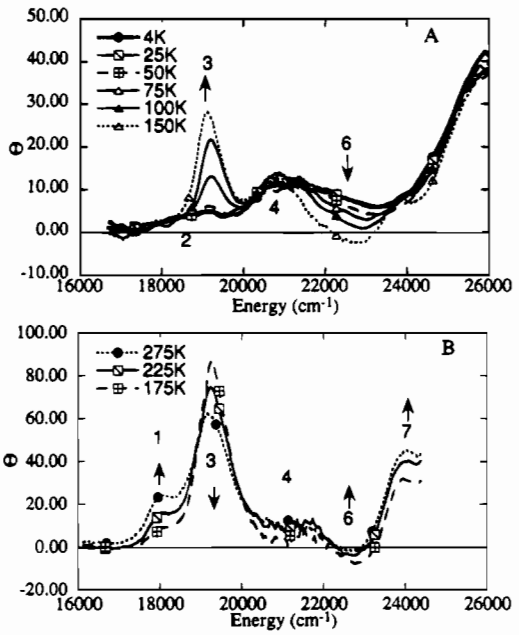

Figure 8. Variable temperature MCD data for **1**: (A) variable temperature data between 4 and 150 K; (B) variable temperature data between 175 and 275 K. Arrows indicate the change in intensity with increasing temperature.

and 20 800 cm^{-1} which correspond to bands 2 and 4. A positive *C*-term at 19 000 cm^{-1}, corresponding to band 3, starts growing in at 50 K which peaks at 175 K and then starts to decrease at higher temperature (Figure 8A,B). A negative *C*-term also appears at 22 000 cm^{-1}, band 6, and follows the same temperature dependence. Two more peaks appear at higher temperatures in Figure 8B, bands 1 and 7, and continue to increase with increasing temperature. The fit of the intensity to the Boltzmann population of the sublevels of the ground state follows that expected for the $S = 1$ and $S = 2$ components, but

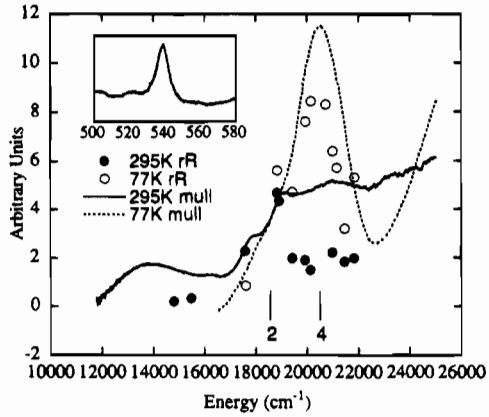

Figure 9. Variable temperature resonance Raman spectra of **1**. The inset shows the Fe−O−Fe vibration at 540 cm^{-1}. The profile is plotted against 77 and 295 K mull spectra.

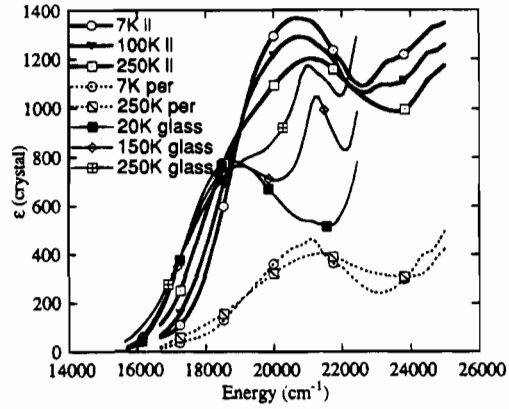

Figure 10. Variable temperature single crystal and glass absorption of **2**. The thicker lines and dotted lines give the parallel and polarized absorption spectra respectively. The thinner lines correspond to aqueous saturated LiCl glass spectra.

with a reduced value for J (~−70 cm^{-1}). This is attributed to hydrogen bonding to the oxo bridge in the H_2O/glycerol glass. This effect has also been observed for oxyHr and in some model complexes.[27,51] Since no monomeric *C*-term behavior is observed (i.e. decreasing intensity with temperature), there appears to be no monomeric impurity as noted earlier.[42] The MCD data demonstrate that bands 6 and 7 correspond to transitions originating from the $S = 1$ and $S = 2$ components of the ground state, respectively.

Resonance Raman profiles were obtained for the Fe−O−Fe symmetric stretch at 540 cm^{-1} (inset) at 77 K and room temperature and are shown in Figure 9. The room temperature profile is very similar to that described previously for structure **3**.[36] From the profiles, two features appear to be enhanced at low temperature, bands 2 and 4, which are the only bands present in this region at 77 K. The enhancement of band 4 decreases with increasing temperature while that of band 2 shows less of a temperature dependence. On the basis of the fact that the Fe−O−Fe symmetric stretch is enhanced by resonance from bands 2 and 4 and that these are transitions from the singlet components of the GS, bands 2 and 4 are assigned as oxo → Fe^{3+} charge transfer (CT) transitions.

Using the preceding data, a clear picture of the types of transitions present in this region has emerged (Figure 6, Table 1). The resonance enhanced singlet transitions, bands 2 and 4, are assigned as oxo → Fe^{3+} charge transfer (CT) transitions. Bands 1, 3, 6, and 7, which all originate from $S > 0$ components of the ground state, are assigned as ligand field transitions. This is supported by the sharpness of these bands, since the expected ligand field transitions in this region ($^4A_1$, ^4E, $^4T_2{}^b$) are LF independent spin flip ($t_{2g}{}^3e_g{}^2 \rightarrow t_{2g}{}^3e_g{}^2$) transitions. Bands 1 and 3, in particular, have widths of ~400 cm^{-1}, based on Gaussian resolution of the mull and solution spectra. This width is almost five times smaller than the width of band 4 (oxo → Fe^{3+} CT) and the $^6A_1 \rightarrow {}^4T_1{}^a, {}^4T_2{}^a$ transitions which all involve an orbital change in the transition. On the basis of their energy, they are assigned to components of the $^6A_1 \rightarrow {}^4A_1$, ^4E transitions. Band 5, although an $S = 0$ transition, does not enhance the Fe−O−Fe stretch and thus is assigned, along with bands 6 and 7, as components of the $^4T_2{}^b$ transition, which is predicted from LF theory to be the next transition in energy.

The results of compound **1** can be extended to the analysis of the spectrum of compound **2** (Figure 10). First considering the glass spectrum, the broad feature at 18 500 cm^{-1} in Figure 10 is assigned as the $^6A_1 \rightarrow {}^4T_2{}^a$ octahedral transition since it shows little temperature dependence (as observed for the same transition in compound **1**) and is the second lowest observed transition energetically. The peak growing in at 20 800 cm^{-1} with increasing temperature is assigned as the next ligand field transitions, $^4A_1$, ^4E, based on its band width, significantly smaller than that of the $^4T_2{}^a$ transition, and its temperature dependence, similar to that observed for the $^4A_1$, ^4E transitions in **1**. The peak splits at 250 K with another component to higher energy which can be associated with population of a higher spin component of the ground state. Alternatively, the polarized single crystal absorption spectra (Figure 10) looks significantly different from the glass spectra. The main intensity in the crystal is along the Fe−Fe vector with a minimum epsilon value of 1200 M^{-1} cm^{-1} at 21 000 cm^{-1} at low temperature. Again stray light truncates the peak of this band but it is clear that the intensity decreases with increasing temperature. The sharp feature assigned as the $^4A_1$, ^4E transition is no longer observed, but the 18 500 cm^{-1} band is still present as a shoulder. On the basis of its temperature dependence and intensity, the peak at 21 000 cm^{-1} in the crystal is assigned as an oxo → Fe^{3+} charge transfer transition. The variable temperature solid mull MCD spectrum of **2** (supplementary Figure S1) does show the temperature dependent $^4A_1$, ^4E transitions, at ~21 000 cm^{-1}. The charge transfer transition in the glass must be shifted to higher energy, thus allowing the LF bands to be easily observed. This shift in bands between the crystal and solution data is attributed to medium effects of the aqueous LiCl solution on the Fe−oxo dimer complex. The intense feature of the glass at ~25 000 cm^{-1} showing singlet temperature dependence in Figure 2B can be assigned as the lowest energy oxo → Fe^{3+} charge transfer transition.

Region III. The Kramers−Kronig transformed absorption from polarized single-crystal specular reflectance data for **1**, **2**, and **3** for the region between 12 000 and 45 000 cm^{-1} are shown in Figure 11A−C. (The raw reflectance data is included in supplementary Figure S2.) The tribridged structures will be analyzed first. Reflectance data could be obtained for only the y (parallel to Fe−Fe) and x (perpendicular to Fe−Fe and out of plane) polarizations of **1** (010 face). In order to estimate the z-polarized spectrum in this region, data for complex **3** (where the Me_3Tacn ligand has been replaced by Tacn) was also obtained which has mixed x and y polarizations along the {010} direction with the solid line giving $0.5y$ and $0.5x$ when the two crystallographically inequivalent sites are averaged. Spectra taken along the {001} direction, on the other hand, give a pure z-polarized spectrum. Due to the lower intensity in the visible

(51) Oberhausen, K. J.; Richardson, J. F.; Buchanan, R. M.; McCusker, J. K.; Webb, R. J.; Hendrickson, D. N. *Inorg. Chem.* **1992**, *31*, 1125−1127.

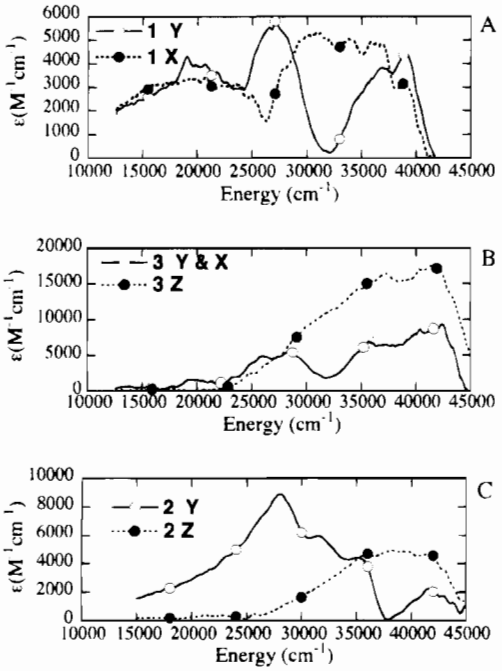

Figure 11. Single crystal polarized absorption data for **1** (A), **3** (B), and **2** (C) obtained from Kramers–Kronig transformed specular reflectance.

region and the fitting procedure used, the absorption data is most accurate in region III at energies greater than 25 000 cm^{-1}. The first major features in region III for **1** and **3** in Figure 11A,B are two predominantly parallel polarized peaks between 25 000 and 30 000 cm^{-1}. They overlap in the pure parallel polarization in Figure 11A for compound **1**, but in the data given in Figure 11B for compound **3**, the peaks are resolved at 26 000 and 28 800 cm^{-1}. The other significant parallel polarization transitions in **1** and **3** are between 34 000 and 44 000 cm^{-1} where two to three bands are observed. (Note that the intensity drop at 40 000 cm^{-1} in Figure 11A is due to the limit of data obtained.) The perpendicular intensity (x in Figure 11A) starts increasing above 25 000 cm^{-1} with an intense peak at 30 000 cm^{-1} and a series of peaks following to higher energy. Comparison between Figure 11A,B indicate that there are z-polarized transitions above 30 000 cm^{-1} with greater intensity than x. On the basis of their polarization, the two lower energy parallel polarized peaks are assigned as oxo → Fe^{3+} CT transitions following Reem[24] since the oxo–Fe vector has the largest projection along the Fe–Fe vector. These peaks are also present in the solution data (Figure 2A) with the higher energy band at 29 000 cm^{-1} more intense in solution due to contributions from overlapping perpendicular bands.

For the monobridged structure in Figure 11C, following Reem[24] the polarized data also show that the predominant intensity between 20 000 and 34 000 cm^{-1} in region III is parallel polarized. There are three lower energy parallel polarized peaks at 28 000, 31 500, and 35 000 cm^{-1} and additional parallel intensity between 40 000 and 45 000 cm^{-1}. Perpendicular polarized intensity (mainly z) grows in at higher energy (between 30 000 and 35 000 cm^{-1}) and a series of peaks are observed above 35 000 cm^{-1}. Again, on the basis of their parallel polarization, the three bands between 25 000 and 35 000 cm^{-1} are assigned as oxo → Fe^{3+} CT transitions.

One important feature to note is the temperature dependence of the features of **2** shown in Figure 2B with some bands (29 000, 36 500 cm^{-1}) decreasing in intensity with decreasing temperature and other bands showing the opposite temperature dependence (32 500 and 42 500 cm^{-1}). This temperature dependence for **2** has been noted previously.[2] The temperature dependence of the absorption spectrum for **1** in region III of Figure 2A is not as pronounced. Differences between the spectra of the tribridged (compounds **1** and **3**) and monobridged (compound **2**) complexes and the temperature dependence of the intensity of the bands of regions II and III are addressed in the analysis section.

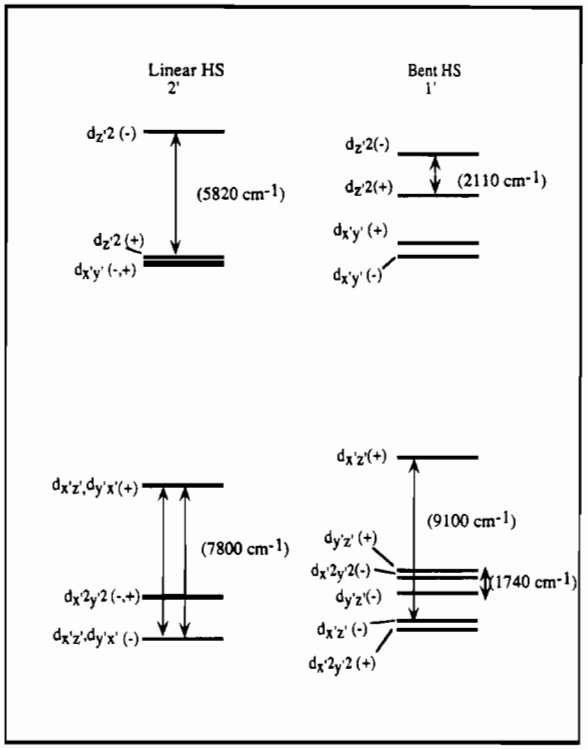

Figure 12. High spin unoccupied d-orbital splitting for **2′** (left) and **1′** (right) obtained from SCF–Xα–SW calculations. Orbitals are labeled according to their predominant Fe character. The (+) and (−) labels are used to differentiate symmetric and antisymmetric combinations of the monomer orbitals.

SCF–Xα–SW Calculations. To further elucidate the electronic structure of the Fe(III)–O–Fe(III) unit, both full symmetry and broken symmetry spin unrestricted SCF–Xα–SW calculations on the linear, **2′**, and bent (Fe–O–Fe angle = 120°), **1′**, structures have been performed. The high spin (HS) $S = 5$ or ferromagnetic state is calculated in full C_{2v} symmetry. This is the only pure spin state that can be described by a single determinant and will be considered first. Due to the spin unrestricted nature of these calculations, spin up and spin down electrons occupy different spatial orbitals. For HS d^5 dimers the occupied 10 spin up orbitals are stabilized in energy below the unoccupied spin down orbitals by ~6 eV and are significantly mixed with ligand character as has been calculated before for Fe–S clusters.[52] This inverted bonding scheme for d^5 Fe has also been observed in Fe monomers and probed experimentally.[53] We will focus on the higher energy spin down orbitals since these orbitals are mainly metal in character. Energy level diagrams for **2′** and **1′** giving the 10 unoccupied d orbitals obtained from these calculations are shown in Figure 12. The coordinate frame used to describe the Fe wave functions corresponds to the primed notation given in Figure 1 which orients the z'-axis along the Fe–oxo bond with x' and y' bisecting the equatorial Fe–ligand bonds. The oxo wave

(52) Noodleman, L.; Baerends, E. J. *J. Am. Chem. Soc.* **1984**, *106*, 2316–2327.
(53) Butcher, K. D.; Didziulis, S. V.; Briat, B.; Solomon, E. I. *J. Am. Chem. Soc.* **1990**, *112*, 2231–2242.

Table 2. High Spin Unoccupied d Orbitals

A. Structure **2′**

level	occ	spin	orbital	energy (eV)	oxo	Fe	H_2O	NH_3	NH_3	H1	H2	H3	H4	H5	H6	H7
$30B_2$	0.0	↓	$d_{z'^2}(-)$	−4.960	5	74	2	8	9	0	0	0	0	0	0	0
$32A_1$	0.0	↓	$d_{z'^2}(+)$	−5.682	2	71	2	8	15	0	0	0	0	0	0	1
$22A_1$	0.0	↓	$d_{x'y'}(-)$	−5.710	0	70	5	22	0	1	1	1	1	0	0	0
$24B_1$	0.0	↓	$d_{x'y'}(+)$	−5.734	1	69	4	23	0	1	1	1	1	0	0	0
$31A_1$	0.0	↓	$d_{y'z'}(+)$	−7.025	17	80	1	1	0	0	0	0	0	0	0	0
$23B_1$	0.0	↓	$d_{x'z'}(+)$	−7.031	17	80	1	1	0	0	1	0	0	0	0	0
$29B_2$	0.0	↓	$d_{x'^2-y'^2}(-)$	−7.698	0	90	9	0	0	0	0	0	0	0	0	0
$304A_1$	0.0	↓	$d_{x'^2-y'^2}(+)$	−7.708	0	90	9	0	0	0	0	0	0	0	0	0
$21A_2$	0.0	↓	$d_{x'z'}(-)$	−7.996	0	98	0	0	0	0	0	0	0	0	0	0
$28B_2$	0.0	↓	$d_{y'z'}(-)$	−7.996	0	98	0	0	0	0	0	0	0	0	0	0

B. Structure **1′**

level	occ	spin	orbital	energy (eV)	oxo	Fe	O-Ace	NH_3	NH_3	C1	H1	H2	H3	H4	H5	H6
$30B_2$	0.0	↓	$d_{z'^2}(-)$	−2.837	6	74	3	8	9	0	0	0	0	0	0	0
$34A_1$	0.0	↓	$d_{z'^2}(+)$	−3.053	5	74	5	4	11	0	0	0	0	0	0	0
$26B_1$	0.0	↓	$d_{x'y'}(+)$	−3.332	0	70	9	19	0	0	1	0	0	0	0	0
$22A_2$	0.0	↓	$d_{x'y'}(-)$	−3.437	0	72	7	20	0	0	0	0	0	0	0	0
$25B_1$	0.0	↓	$d_{x'z'}(+)$	−4.402	23	72	2	2	0	0	0	0	0	0	0	0
$33A_1$	0.0	↓	$d_{y'z'}(+)$	−5.077	10	83	0	3	3	0	0	0	0	0	0	0
$29B_2$	0.0	↓	$d_{x'^2-y'^2}(-)$	−5.276	0	93	5	1	1	0	0	0	0	0	0	0
$28B_2$	0.0	↓	$d_{y'z'}(-)$	−5.339	1	91	6	0	2	0	0	0	0	0	0	0
$21A_2$	0.0	↓	$d_{x'z'}(-)$	−5.535	0	97	2	0	0	0	0	0	0	0	0	0
$32A_1$	0.0	↓	$d_{x'^2-y'^2}(+)$	−5.632	0	95	1	1	0	3	0	0	0	0	0	0

functions are denoted as either p_π or p_σ, with the p_π divided into in plane (y) and out of plane (x). In this HS calculation the 10 d orbitals arise from symmetric (+) and antisymmetric (−) combinations of the five monomer Fe d orbitals on each side of the dimer and are so labeled in Figure 12. The charge distribution and energies of these orbitals are given in Table 2. For the linear structure (Figure 12, left), there is an energy splitting between the symmetric and antisymmetric combinations of the d orbitals, particularly the $d_{x'z'}$, $d_{y'z'}$ which are π antibonding to the oxo and $d_{z'^2}$ orbitals which are involved in σ antibonding with the oxo bridge. This splitting has also been predicted previously based on qualitative MO theory.[54] The contour plots of the wave functions for these linear (**2′**) Fe−oxo HS orbitals are given in Figure 13. Figure 13A shows the antisymmetric combination of the Fe $d_{z'^2}$ orbitals (level $30B_2$ in Table 2) which undergo a strong σ antibonding interaction with the oxo $p_{z'}$ orbital. This leads to its destabilization and thus is the highest level, $d_{z'^2}$ (−), in Figure 12 (left). Figure 13B shows that the $d_{z'^2}$ (+) combination (level $32A_1$ in Table 2A) also undergoes an antibonding interaction but with the oxo 2s orbital. The π antibonding interaction between the symmetric combination Fe $d_{y'z'}$ orbitals and oxo $p_{y'}$ orbital (level $31A_1$ Table 2A) is shown in Figure 13C, while Figure 13D gives the antisymmetric combination of the Fe $d_{y'z'}$ orbitals (level $28B_2$ in Table 2A) which is nonbonding to the oxo $p_{y'}$ orbital. The corresponding contour plots for the Fe $d_{x'z'}$ orbital (levels $23B_1$ and $21A_2$ in Table 2A) are identical to Figure 13C,D and are not shown.

Both Hoffmann[55] and Kahn[56] have shown that the ground state J value is proportional to the energetic difference between the symmetric and antisymmetric components of the d orbitals. In our results for the linear HS case, the splittings between the +/− combinations of the π ($d_{x'y'}$, $d_{y'z'}$) and σ ($d_{z'^2}$) orbitals are very similar, 7800 and 5820 cm^{-1} respectively (Figure 12, left). The magnitude of the orbital splitting is an indicator of the effectiveness of the pathway for superexchange. Thus the π pathways ($Fe(d_{x'z'}) - O(p_{x'})-Fe(d_{x'z'})$, $Fe(d_{y'z'})-O(p_{y'})-Fe(d_{y'z'})$) in the linear calculation are predicted to be more efficient at coupling than the σ pathway ($Fe(d_{z'^2})-O(p_{z'})-Fe(d_{z'^2})$), but all three make significant contributions. This is in contrast to a recent study using extended Huckel calculations which found the sigma pathway to be negligible in linear Fe−oxo dimers.[57] While extended Huckel calculations have been used with great success to obtain insight into exchange coupling between metals,[55] SCF−Xα−SW calculations should give a more quantitative description of transition metal electronic structure.[58−60]

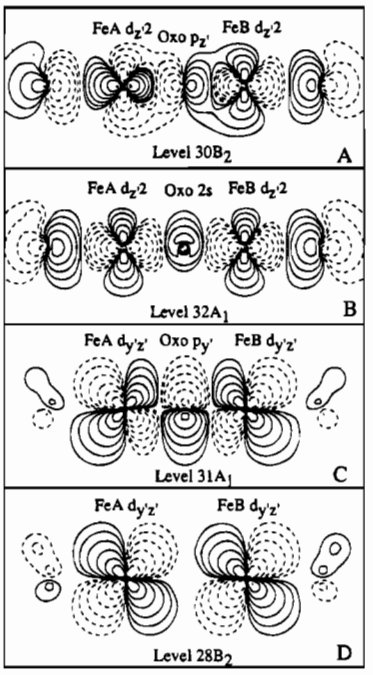

Figure 13. High spin contour plots of the $d_{z'^2}(-)$ orbital (A), $d_{z'^2}(+)$ orbital (B), $d_{yz}(+)$ orbital (C) and $d_{yz}(-)$ orbital (D) of the linear structure **2′**.

Upon bending in the yz plane for the bent structure **1′**, the splitting of the out of plane π [$d_{x'z'}(+)$ and $d_{x'z'}(-)$] stays

(54) Dunitz, J. D.; Orgel, L. E. *J. Chem. Soc.* **1953**, 2594−2596.
(55) Hay, P. J.; Thibeault, J. C.; Hoffmann, R. *J. Am. Chem. Soc.* **1975**, *97*, 4884−4899.
(56) Kahn, O.; Briat, B. *J. Chem. Soc., Faraday Trans* **1976**, *72*, 268−281.
(57) Hotzelmann, R.; Wieghardt, K.; Flörke, U.; Haupt, H.-J.; Weatherburn, D. C.; Bonvoisin, J.; Blondin, G.; Girerd, J.-J. *J. Am. Chem. Soc.* **1992**, *114*, 1681−1696.

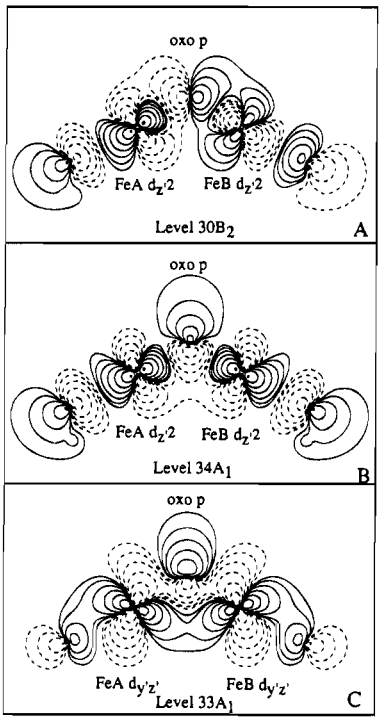

Figure 14. High spin contour plots of the $d_{z^2}(-)$ orbital (A), $d_{z^2}(+)$ orbital (B), and $d_{yz}(+)$ orbital (C) of the bent structure **1′**.

approximately the same (9100 cm^{-1}) with the in plane π [$d_{y'z'}$-(+) and $d_{y'z'}(-)$] and σ[$d_{z^2}(+)$ and $d_{z^2}(-)$] orbital splittings decreasing to 2110 and 1740 cm^{-1}, respectively (Figure 12 right). The contours of structure **1′** also show significant differences from the linear dimer. Parts A and B of Figure 14 show the antisymmetric (level $30B_2$ in Table 2B) and symmetric (level $34A_1$ in Table 2B) combinations of the d_{z^2} orbitals which still undergo antibonding interactions with the oxo bridge. The (−) combination is antibonding with an oxo p orbital oriented along the Fe−Fe axis (Figure 14A), and the (+) combination interacts with one lobe of an oxo p orbital along the C_2 axis (Figure 14B). Figure 14C illustrates the mixed nature of the symmetric combination of $d_{y'z'}$ orbitals (level $33A_1$ in Table 2B) which undergoes a mainly antibonding interaction with the oxo p orbital along the C_2 axis. The antisymmetric (−) component of $d_{y'z'}$ orbital (level $28B_2$ in Table 2B) is nonbonding and is not shown. The out of Fe−O−Fe plane $d_{x'z'}$ orbitals (level $25B_1$ and $21A_2$ in Table 2B) are mostly unaffected by bending and give contours similar to **2′** (Figure 13C,D). One might expect, on the basis of a total decrease in energetic splittings for in plane π and σ orbital pathways, that the GS J value would decrease upon bending. This is not observed experimentally. Recently,[57] a mixed $\pi-\sigma$ (Fe($d_{y'z'}$)−O($p_{y'}$)−Fe(d_{z^2})) pathway which becomes efficient upon bending was invoked to account for the magnetic properties of mixed metal dimers. When the Fe−O−Fe angle is bent, the Fe $d_{z^2}(+)$ orbitals can mix with $d_{y'z'}(+)$ also of A_1 symmetry, changing their energies and thus masking the (+)/(−) splitting. A method of approximating this interaction is given in ref 57. As shown below, the BS calculation gives a detailed description of this mixed $\pi-\sigma$ pathway.

Broken symmetry calculations allow one to treat exchange coupling by considering two linked monomer units of equal and opposite spin density.[48] In the broken symmetry calculation, the full symmetry C_{2v} is lowered to C_s and spin up and spin down densities are allowed to localize on either side of the dimer. This gives a more accurate representation of two spin-coupled ferric centers than the above fully delocalized MO

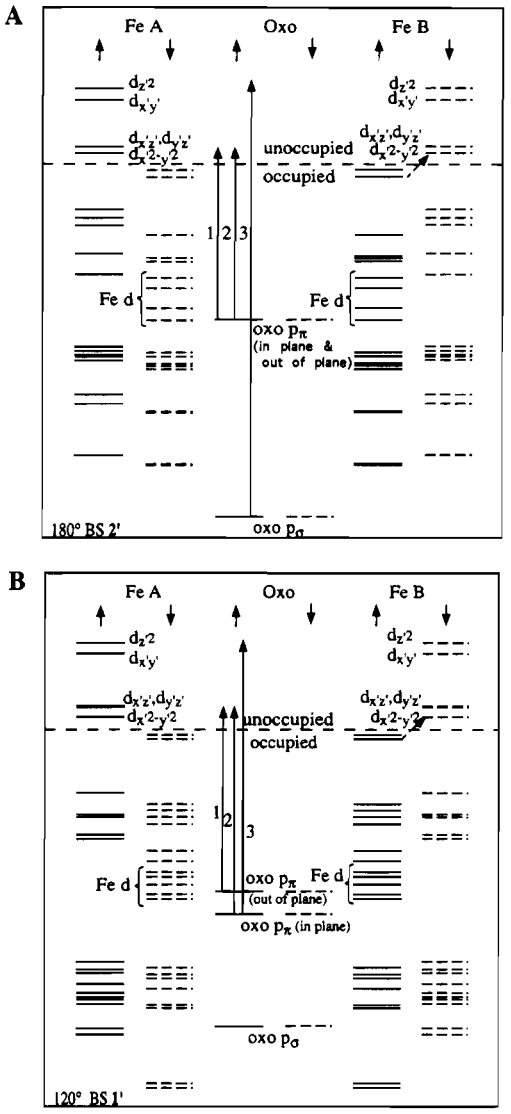

Figure 15. Broken symmetry orbital splitting diagrams for structures **2′** (A) and **1′** (B). The orbitals are separated as to where the predominant electron density residues, i.e. on the left side of the dimer, FeA; in the middle, oxo; or on the right side of the dimer, FeB. The spin up/spin down separation exhibited in these spin unrestricted calculations is also illustrated with the spin up orbitals denoted by solid lines and the spin down orbitals denoted by broken lines. Arrows illustrate the three lowest energy oxo → Fe^{3+} CT transitions.

calculations. The one-electron energy diagrams obtained for the broken symmetry calculations of **2′** and **1′** are given in parts A and B of Figure 15, respectively. In Figure 15, the levels are grouped as to where their spin density is localized, either on the left (FeA), right (FeB) or middle (oxo) of the molecule. Both calculations give the Fe unoccupied d orbitals highest in energy with the corresponding occupied d orbitals stabilized by ~6 eV. This is due to the spin-polarized nature of these calculations as discussed above. The charge distributions and energies are given in Table 3 for the unoccupied d orbitals (spin up on FeA and spin down on FeB) and the oxo π orbitals for the broken symmetry calculations of **2′** and **1′**. The occupied d orbitals which should be paired with the spin down orbitals are more mixed in character due to their exchange stabilization and these orbitals are labeled Fe d in the middle of Figure 15A,B. The splitting of the unoccupied d orbitals in Figure 15A and 15B gives the expected orbital splitting for a C_{4v} strong axial LF distorted octahedral monomer. The Fe d_{z^2} orbital is highest in energy due to the strong oxo σ bond along z', and the Fe $d_{x'z'}$, $d_{y'z'}$ orbitals are nearly degenerate in energy and

Table 3. Broken Symmetry Orbitals

A. Structure **2′**

level	occ	spin	orbital[a]	energy (eV)	oxo	FeA	FeB	H_2O	H_2O	NH_3	NH_3	NH_3	NH_3	H1	H1′	H2	H2′	H3
62A′	0.0	↓	$d_{z'^2}$	−5.328	3	2	71	0	2	0	8	0	12	0	0	0	0	0
31A′	0.0	↑	$d_{z'^2}$	−5.328	3	71	2	2	0	8	0	12	0	0	0	0	0	0
23A″	0.0	↑	$d_{x'y'}$	−5.724	0	70	0	5	0	22	0	0	0	1	0	1	0	1
46A″	0.0	↓	$d_{x'y'}$	−5.724	0	0	70	0	5	0	22	0	0	0	1	0	1	0
45A″	0.0	↓	$d_{x'z'}$	−7.518	9	1	86	0	0	2	0	0	0	0	0	0	0	0
22A″	0.0	↑	$d_{x'z'}$	−7.518	9	86	1	0	0	0	2	0	0	0	0	0	0	0
61A′	0.0	↓	$d_{y'z'}$	−7.522	9	1	87	0	0	1	1	0	0	0	0	0	0	0
30A′	0.0	↑	$d_{y'z'}$	−7.522	9	87	1	0	0	1	1	0	0	0	0	0	0	0
60A′	0.0	↓	$d_{x'^2-y'^2}$	−7.684	0	0	90	0	9	0	0	0	0	0	0	0	0	0
29A′	0.0	↑	$d_{x'^2-y'^2}$	−7.684	0	90	0	9	0	0	0	0	0	0	0	0	0	0
38A″	1.0	↓	p_π(op)	−13.643	34	45	4	1	2	6	2	1	0	0	0	0	0	2
15A″	1.0	↑	p_π(op)	−13.643	34	4	45	2	1	2	6	0	1	0	0	0	0	1
50A′	1.0	↓	p_π(ip)	−13.653	35	44	4	1	1	5	2	1	0	1	0	0	0	2
19A′	1.0	↑	p_π(ip)	−13.653	35	4	44	1	1	2	5	0	1	0	1	0	0	0
39A′	1.0	↓	p_σ	−20.586	51	25	23	0	0	0	0	0	0	0	0	0	0	0
8A′	1.0	↑	p_σ	−20.586	51	23	25	0	0	0	0	0	0	0	0	0	0	0

B. Structure **1′**

level	occ	spin	orbital[a]	energy (eV)	oxo	FeA	FeB	O-Ace	O-Ace	NH_3	NH_3	NH_3	NH_3	C	H1	H2	H2′	H3
32A′	0.0	↑	$d_{z'^2}$	−3.116	4	73	1	4	0	6	0	11	0	0	0	0	0	0
64A′	0.0	↓	$d_{z'^2}$	−3.116	4	1	73	0	4	0	6	0	11	0	0	0	0	0
24A″	0.0	↑	$d_{x'y'}$	−3.442	0	70	0	8	0	20	0	0	0	0	0	0	0	0
48A″	0.0	↓	$d_{x'y'}$	−3.442	0	0	70	0	8	0	20	0	0	0	0	0	0	0
23A″	0.0	↑	$d_{x'z'}$	−5.079	12	83	2	1	0	1	0	0	0	0	0	0	0	0
47A″	0.0	↓	$d_{x'z'}$	−5.079	12	2	83	0	1	0	1	0	0	0	0	0	0	0
31A′	0.0	↑	$d_{y'z'}$	−5.141	8	77	8	1	1	1	1	0	2	0	0	0	0	0
63A′	0.0	↓	$d_{y'z'}$	−5.141	8	8	77	1	1	1	1	2	0	0	0	0	0	0
30A′	0.0	↑	$d_{x'^2-y'^2}$	−5.535	0	91	0	5	1	1	0	0	0	1	0	0	0	0
62A′	0.0	↓	$d_{x'^2-y'^2}$	−5.535	0	0	91	1	5	0	1	0	0	1	0	0	0	0
40A″	1.0	↓	p_π(op)	−10.697	14	44	2	16	12	3	0	0	0	8	0	0	0	0
16A″	1.0	↑	p_π(op)	−10.697	14	2	44	12	16	0	3	0	0	8	0	0	0	0
18A′	1.0	↑	p_π(ip)	−11.842	48	9	33	2	3	0	1	0	1	1	1	0	1	0
50A′	1.0	↓	p_π(ip)	−11.842	48	33	9	3	2	1	0	1	0	1	1	1	0	0
11A′	1.0	↑	p_σ	−15.001	51	19	26	0	0	1	1	0	0	0	0	0	0	0
43A′	1.0	↓	p_σ	−15.001	51	26	19	0	0	1	1	0	0	0	0	0	0	0

[a] Key: op = out of plane; ip = in plane.

above the Fe $d_{x'^2-y'^2}$. There is a small energy splitting in the $d\pi(d_{x'z'},d_{y'z'})$ set for **1′** of 500 cm^{-1}. As shown in Table 3A for structure **2′**, there are only three d orbitals: $d_{z'^2}$ (level 62A′), $d_{x'z'}$ (level 45A″), and $d_{y'z'}$ (level 61A′) localized on FeB (Figure 15A right) which are involved in bonding with the oxo bridge. (Levels 31A′, 22A″, and 30A′ in Table IIIA are the equivalent unoccupied spin up d orbitals localized on FeA, i.e. Figure 15A left.) These $d_{x'z'}$, $d_{y'z'}$ and $d_{z'^2}$ orbitals are also the only unoccupied d orbitals which have any delocalization, i.e. with FeA character mixed into a predominantly FeB orbital. The delocalization and oxo character of these orbitals reflect the effectiveness of these orbitals as superexchange pathways. From the orbital breakdown given in Table 3A, the delocalization is very similar for these three orbitals but the $d_{x'z'}$ and $d_{y'z'}$ orbitals have more oxo p character. Therefore all should be effective for exchange with the π pathways slightly better as was predicted from the +/− splitting in the high spin calculations above.

The occupied bonding out of plane oxo p_π orbitals, levels 15A″ and 38A″ in Table 3A, in plane oxo p_π orbitals, levels 19A′ and 50A′ in Table 3A, and oxo p_σ orbitals, levels 8A′ and 39A′, correspond to the spin up/spin down oxo p orbitals labeled in the center of Figure 15A. The p_π orbitals are similar in energy with significant Fe character in each indicating a covalent π bond. Table 3B for the bent structure **1′** shows that again there are three d orbitals: $d_{z'^2}$ (level 64A′), $d_{x'z'}$ (level 47A″), and $d_{y'z'}$ (level 63A′) localized on FeB (Figure 15B right) which are involved in bonding to the oxo bridge. The equivalent spin up unoccupied d orbitals localized on FeA are 32A′, 23A″, and 31A′ (Table 3B). Note that in the coefficients of Table 3B, level 63A′ ($d_{y'z'}$ for FeB) is more delocalized than the other d orbitals and this is evidence that the in plane pathway is still effective for exchange (due to π/σ mixing, *vide infra*). The oxo π orbitals for **1′**, levels 40A″ and 16A″ (Table 3B) for the out of plane p_π and levels 50A′ and 18A′ (Table 3B) for the in plane p_π, are split in energy with the out of plane p_π orbital highest in energy and delocalized over the oxo, iron, and acetate oxygens. This is due to mixing of orbitals of the same symmetry very close in energy. The in plane p_π orbital is stabilized due to the increased delocalization in **1′** and the σ-bonding interaction it picks up with the $d_{z'^2}$ orbital. The oxo p_σ orbital, levels 43A′ and 11A′ (Table 3B), is still stabilized below the π orbitals but not as much as the linear case since some σ-bonding interaction has been lost. These oxo p orbitals are labeled in the center of Figure 15B.

One of the advantages of BS−SCF−Xα−SW calculations is that they allow for a reasonable estimate of the ground state exchange parameter J (usually approximately a factor of 2 higher than experiment).[52,58,59] While the broken symmetry state is not a pure spin state and cannot be equated with the $S = 0$ ground state, the contributions of the pure spin states has been determined using spin projection techniques[58] which leads to the following relation:

$$J = (E_{HS} - E_{BS})/-S_{max}^2 \quad (3)$$

E_{HS} and E_{BS} are the energies corresponding to the high spin

(58) Noodleman, L.; Norman, J. G., Jr. *J. Chem. Phys.* **1979**, *70*, 4903−4906.
(59) Noodleman, L.; Case, D. *Adv. Inorg. Chem.* **1992**, *38*, 423.

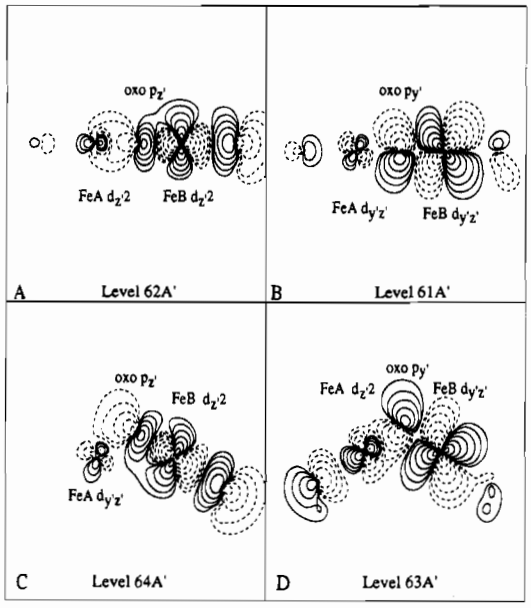

Figure 16. Broken symmetry contour plots of the Fe d orbitals. (A) gives the FeB $d_{z'^2}$ orbital of **2'**. (B) gives the FeB $d_{y'z'}$ orbital of **2'**. (C) gives the FeB $d_{z'^2}$ orbital of **1'**. (D) gives the FeB $d_{y'z'}$ orbital of **1'**.

(HS) or ferromagnetic $S_{max} = 5$ calculation and broken symmetry calculation, respectively. Values of J for **1'** and **2'** are obtained as -260 and -230 cm^{-1}, respectively. These values are within the range expected for these calculations and reflect the observed experimental trend with the experimental J values of -120 and -95 cm^{-1} for **1** and **2** respectively. These BS−SCF−Xα−SW calculations can be used to gain further insight into individual orbital pathway contributions to these J's and provide a basis for an analysis of the CT spectrum in section III of the analysis.

The contour plots of the BS−SCF−Xα−SW d orbital wave functions, Figure 16, provide insight into the orbital interactions involved in the antiferromagnetic coupling of the ground state. Level 62A' (Table 3A) for the linear structure **2'** is shown in Figure 16A and illustrates the Fe($d_{z'^2}$)−oxo($p_{z'}$)−Fe($d_{z'^2}$) σ pathway in the BS calculation which is strongly antibonding. This is to be compared to the contours in parts A and B of Figure 13 for the HS calculation for **2'** which also show the Fe($d_{z'^2}$)−oxo($p_{z'}$)−Fe($d_{z'^2}$) interactions. The BS calculation shows that the electron density localized is on one Fe as expected for an antiferromagnetically coupled dimer. The $d_{y'z'}$ π interaction in the linear structure (level 61A' in Table 3A) is given in Figure 16B which is applicable for both the Fe π $d_{y'z'}$ and $d_{x'z'}$ pathways. Note these contours parallel those for the linear HS calculation in Figure 13C,D, but again the BS calculations allow for the localization of electron density. These three d orbitals, Fe $d_{x'z'}$, Fe $d_{y'z'}$, and Fe $d_{z'^2}$, are the only ones that interact with the bridging oxo ligand or have delocalization (Table 3A) and thus are the main pathways for exchange. The contour plots shown for the bent structure **1'** (Figure 16C,D) show some major differences in exchange pathways compared to those for **2'**. Level 64A' (Table 3B), which is the highest energy orbital in Figure 15B (right), shows the $d_{z'^2}$ orbital of FeB antibonding to the oxo $p_{z'}$, which is also antibonding with the $d_{y'z'}$ π orbital on FeA (Figure 16C). This gives a clear representation of the mixed π/σ pathway which could only be inferred in the HS calculation above. Figure 16D shows that a mixed π/σ pathway also occurs for level 63A' (Table 3B) with the FeB $d_{y'z'}$ antibonding to oxo $p_{y'}$, which then antibonds with the $d_{z'^2}$ of FeA. From Table 3B, this pathway has significant delocalization and oxo character. This delocalization stabilizes the oxo p_y orbital (levels 18A' and 50A', Table 3B) due to the increased bonding interactions. The out of plane Fe($d_{x'z'}$)−O($p_{x'}$)−Fe($d_{x'z'}$) orbital (level 47A'' in Table 3B) is similar to that observed for the linear case (Figure 16B) and is not shown. In summary, the important BS−SCF−Xα−SW Fe−oxo interactions (Figure 16) are the σ(Fe($d_{z'^2}$)−O($p_{z'}$)−Fe($d_{z'^2}$)) and π (Fe($d_{x'z'}$)−O($p_{x'}$)−Fe($d_{x'z'}$), Fe($d_{y'z'}$)−O($p_{y'}$)−Fe($d_{y'z'}$)) interactions in the linear dimer (**2'**), with these interactions still present but reduced upon bending the Fe−O−Fe angle to 120°. The other major superexchange pathways in **1'** involve the mixed pathways Fe($d_{y'z'}$)−O($p_{y'}$)−Fe($d_{z'^2}$) and Fe($d_{z'^2}$)−O($p_{z'}$)−Fe($d_{y'z'}$).

Transition state calculations have been performed for comparison to the excited state absorption data. These calculations involve exciting half an electron from a donor orbital into an acceptor orbital and have been shown to take into account the effects of electronic relaxation.[60] Table 4 presents the results of transition state calculations on **1'** and **2'** with the orbital designations corresponding to the C_{4v} monomer coordinate frame in Figure 1. An estimate of lowest energy LF $^4T_1$ transition energies can also be obtained from these calculations. From the wave functions for the $^4T_1$ (see section 1 of Analysis), the $^4T_1$ is a multiconfigurational state. Only one component is described by a single determinant and thus accurately described in these calculations. It involves the transition from the $^6A_1$ GS to the z component of the $^4T_1$ state and is formally a $d_{x'y'} \rightarrow d_{x'^2-y'^2}$ transition. This transition is shown by the dotted arrow in Figure 15A,B for the BS calculations. The energies of these transitions are 7240 and 5040 cm^{-1} for **2'** and **1'**, respectively. These are somewhat lower than observed experimentally but show the correct experimental trend in energy. The BS oxo → Fe charge transfer transitions were also calculated in the transition state formalism to obtain an initial energy ordering. Since the charge transfer intensity depends on metal/ligand overlap of the orbitals involved in the transition, only those pairs of orbitals which have good overlap were considered. For **2'** these are the out of plane oxo $p_\pi \rightarrow$ Fe $d_{x'z'}$ (levels 38A'' and 45A''), in plane oxo $p_\pi \rightarrow$ Fe $d_{y'z'}$ (levels 50A' and 61A'), and oxo $p_\sigma \rightarrow$ Fe $d_{z'^2}$ (levels 39A' and 62A'). For **1'** these are the out of plane oxo $p_\pi \rightarrow$ Fe $d_{x'z'}$ (levels 40A'' and 47A''), in plane oxo $p_\pi \rightarrow$ Fe $d_{y'z'}$ (levels 50A' and 63A'), in plane oxo $p_\pi \rightarrow$ Fe $d_{z'^2}$ (levels 50A' and 64A'), oxo $p_\sigma \rightarrow$ Fe $d_{y'z'}$ (levels 43A' and 63A'), and oxo $p_\sigma \rightarrow$ Fe $d_{z'^2}$ (levels 43A' and 64A'). The lowest energy oxo charge transfer transitions are given by solid arrows, labeled 1−3 in Figure 15A,B. For the linear calculation on **2'** (Figure 15A), the energies of transitions 1 and 2, corresponding to oxo $p_\pi \rightarrow$ Fe $d_{x'z'}$, Fe $d_{y'z'}$ transitions, are at 55 430 and 55 130 cm^{-1}. Oxo $p_\sigma \rightarrow$ Fe $d_{z'^2}$ (arrow 3) is calculated to be very high in energy at 132 250 cm^{-1}. In the bent BS calculation on **1'**, the lowest energy oxo → Fe^{3+} transition, the out of plane $p_\pi \rightarrow$ $d_{x'z'}$ (arrow 1 in Figure 15B) is predicted to be at 47 963 cm^{-1}, and the second lowest energy transition, the in plane $p_\pi \rightarrow d_{y'z'}$ (arrow 2 in Figure 15B), is predicted to be at 58 880 cm^{-1}. The next transition (arrow 3), the oxo $p_\pi \rightarrow$ Fe $d_{z'^2}$ transition, is predicted to be at ~74 335 cm^{-1}. The other two transitions predicted to have intensity are at much higher energy, 84 090 and 99 315 cm^{-1} (Table 4). A carboxylate to iron transition is also calculated for **1'**, at an energy of 29 000 cm^{-1} (Table 4).

From the experimental results in sections II and III, the lowest energy oxo → Fe^{3+} CT transition is observed at ~21 000 cm^{-1}. As has been previously discussed,[47] these BS−SCF−Xα−SW calculated transition state energies for bridging ligand CT transition in dimers are much higher than observed experimentally when the bridging ligand provides effective superexchange

(60) Slater, J. C. *The Calculation of Molecular Orbitals*; John Wiley & Sons: New York, 1979.

Table 4. Transition State Calculation for **1′** and **2′** (cm^{-1})

BS Calculation				
spin forbidden transitions				
donor		acceptor	**1′**	**2′**
$d_{x'^2-y'^2}$		$d_{x'y'}$	5036	7240
charge transfer transitions				
donor[a]		acceptor	**1′**	**2′**
oxo p_π(op)*	→	$d_{x'z'}$	47 960	55 130
oxo p_π(ip)*	→	$d_{y'z'}$	58 880	55 540
oxo p_π(ip)*	→	$d_{z'^2}$	74 335	no overlap
oxo p_σ	→	$d_{y'z'}$	84 090	no overlap
oxo p_σ	→	$d_{z'^2}$	99 315	132 250
carboxylate	→	$d_{x'^2-y'^2}$	29 000	- - -
HS Calculation				
charge transfer transitions				
donor[a]		acceptor	**1′**	**2′**
oxo p_π(op)*	→	$d_{x'z'}(-)$	36 980	45 400
oxo p_π(op)*	→	$d_{x'z'}(+)$	43 690	49 770
oxo p_π(ip)*	→	$d_{y'z'}(-)$	49 450	46 060
oxo p_π(ip)*	→	$d_{y'z'}(+)$	50 370	50 590
oxo p_π(ip)*	→	$d_{z'^2}(+)$	67 160	no overlap
oxo p_π(ip)*	→	$d_{z'^2}(-)$	68 750	no overlap
oxo p_σ	→	$d_{z'^2}(-)$	91 100	122 160
oxo p_σ	→	$d_{z'^2}(+)$	89 340	126 980
oxo p_σ	→	$d_{y'z'}(-)$	78 430	no overlap
oxo p_σ	→	$d_{y'z'}(+)$	77 480	no overlap

[a] Key: op = out of plane; ip = in plane.

pathways. This can be contrasted to the predicted energy of the carboxylate CT transitions at 29 000 cm^{-1} which is very close to that observed for Fe^{3+} monomers[61] and to the out of plane perpendicular polarized transitions in Figure 11A, which can be assigned to acetate CT transitions. This discrepancy for CT transitions of bridging ligands which provide superexchange pathways has been attributed to excited state antiferromagnetism (ESAF) in the charge transfer states.[39] This ESAF will be addressed in the Analysis section using a valence bond configurational interaction (VBCI) approach.[39]

The VBCI model requires the transition state energies of the oxo → Fe^{3+} CT transitions from the HS calculation ($^{11}B_2 \rightarrow {}^{11}\Gamma$ transitions) which are listed in Table 4. In all cases for the CT transition state calculations in high symmetry, the donor orbitals are the spin down components of the oxo p orbitals which can give spin-allowed transitions to the unoccupied d orbitals (Table 2). For example, in **2′**, transitions from the out of plane oxo p_π orbital to the symmetric (Table 2A, level 23 B_1) and antisymmetric (Table 2A, level 21A_2) combinations of the $d_{x'z'}$ orbitals are calculated at 45 400 (−) and 50 590 cm^{-1} (+). Transitions from the in plane p_π orbital and p_σ orbital for **2′** are also included in Table 4. In **1′** the same transitions as described above for **2′** were calculated, as well as transitions involving the in plane oxo p_π and oxo p_σ to Fe $d_{z'^2}$ and Fe $d_{y'z'}$ respectively (Table 4). The results of these HS transition state calculations will be used to gain insight into excited state exchange (part III of the analysis).

In conclusion, the SCF−Xα−SW linear and bent calculations, in both full symmetry and broken symmetry, give the major pathways for exchange. In the linear case there is a dσ−dσ (Fe($d_{z'^2}$)−O($p_{z'}$)−Fe($d_{z'^2}$)) and two dπ (Fe($d_{x'z'}$)−O($p_{x'}$)−Fe($d_{x'z'}$), Fe($d_{y'z'}$)−O($p_{y'}$)−Fe($d_{y'z'}$)) pathways with the orbital energy splittings from the HS calculations predicting the π pathways to be somewhat more efficient at exchange coupling than the σ pathway. This is confirmed in the BS calculations based on oxo character and delocalization in these unoccupied Fe d orbitals (Table 3). Upon bending, the out of plane π interaction remains unchanged, but the dσ can interact with the in plane dπ orbital. These interactions are most clearly present in the contour plots of the BS orbitals (Figure 16C,D). The calculated BS transition state energies are too high due to the neglect of ESAF, and before an energy ordering and assignment is applied to the charge transfer transitions, the effects of ESAF will have to be explicitly considered.

Analysis

I. Ligand Field Transitions: Dimer Intensity Mechanisms. There are several important features to note in the ligand field transitions of the Fe(III)−O−Fe(III) moiety of structures **1** and **2**. First, the intensity of these transitions is at least an order of magnitude greater than what is normally found for spin forbidden, Laporté forbidden octahedral ligand field transitions in monomeric complexes.[62] The ε values of LF transitions in octahedral high spin ferric complexes with oxygen ligation range from 0.1 to 1.0 M^{-1} cm^{-1},[25] while these LF bands in the Fe−O−Fe dimers have ε values >10 M^{-1} cm^{-1} for the $^6A_1 \rightarrow {}^4T_1{}^a$ transition (Figure 4A,B) and >200 M^{-1} cm^{-1} for $^6A_1 \rightarrow {}^4T_2{}^a$ transition (Figures 5 and 10). Thus the $^6A_1 \rightarrow {}^4T_2{}^a$ transition is an order of magnitude more intense than the $^6A_1 \rightarrow {}^4T_1{}^a$ transition. This intensity increase is also not observed in HS ferric monomers.[62] Another striking feature is the temperature dependence of these transitions. The $^6A_1 \rightarrow {}^4T_1{}^a$ transition for **1** and **2** increases in intensity by a factor of two with increasing temperature (Figure 4A,B). The $^6A_1 \rightarrow {}^4A_1$, ^4E for **1** (Figure 6A and Table 1) and for **2** (Figure 10) and the $^6A_1 \rightarrow {}^4T_2{}^b$ for structure **1** (Figure 6A and Table 1) show new bands appearing with population of higher spin components of the GS. On the other hand, the $^6A_1 \rightarrow {}^4T_2{}^a$ transition (Figures 5 and 10) exhibits little temperature dependence. There is also an effect of low symmetry on these spectra, particularly in the splitting of the $^6A_1 \rightarrow {}^4T_1{}^a$ into two distinct bands which exhibit different properties for structures **1** (Figure 4A) and **2** (Figure 4B). The most intense transition in **1** is the highest in energy of the two transitions and is the only temperature dependent feature (Figure 4A). The most intense transition in **2** is the lowest of the two observed transitions, and both bands are temperature dependent (Figure 4B). There is also an energy dependence of the $^4T_2{}^a$ transition energy when the Fe−O−Fe angle is bent on going from **2** to **1**. The stronger field of the HEDTA ligation of **2** blue shifts these ligand field transitions compared to **1**, but the $^4T_2{}^a$ transition in **2** is shifted to higher energy than is expected based on qualitative LF arguments.[50]

There are two intensity mechanisms that can be effective for spin forbidden electronic transitions in a dimer. One is a mechanism which overcomes the spin selection rule through the exchange interaction. This was suggested in ref 2; however, this mechanism cannot account for the high intensity observed at low temperature when only the $S = 0$ component of the GS is occupied and all transitions are still spin forbidden in the dimer. The second intensity mechanism, single-site spin−orbit (SO) coupling is generally used to overcome the spin forbiddeness of transitions in monomers and has spin selection rules of $\Delta S = 0, \pm 1$.[63,64] Qualitatively this mechanism can account for low temperature intensity, however, an additional feature in the dimer has to be present to make SO coupling much more

(61) Zhang, Y.; Gebhard, M. S.; Solomon, E. I. *J. Am. Chem. Soc.* **1991**, *113*, 5162−5175.
(62) Holt, S.; Dingle, R. *Acta Chem. Scand.* **1968**, *22*, 1091−1096.
(63) Vala, M.; Rivoal, J. C.; Badoz, J. *Mol. Phys.* **1975**, *30*, 1325−1344.
(64) Gebhard, M. S.; Deaton, J. C.; Koch, S. A.; Millar, M.; Solomon, E. I. *J. Am. Chem. Soc.* **1990**, *112*, 2217−2231.

efficient and quantitatively explain the increased intensity relative to a monomer at low temperature.

The transition moment integral for a transition from the $^6A_1$ GS to a $^4\Gamma$ excited state[65] is

$$\langle {}^6A_1 M_S|M_q|{}^4\Gamma M_S'\theta'\rangle = \frac{\langle {}^6A_1 M_S|H_{SO}|{}^4T_1 M_S''\theta''\rangle\langle {}^4T_1 M_S''\theta''|M_q|{}^4\Gamma M_S'\theta'\rangle}{(E({}^4T_1) - E({}^6A_1))} + \frac{\langle {}^6A_1 M_S|M_q|{}^6T_1 M_S''\theta''\rangle\langle {}^6T_1 M_S''\theta''|H_{SO}|{}^4\Gamma M_S'\theta'\rangle}{(E({}^6T_1) - E({}^4\Gamma))} \quad (4)$$

where M_S, M_S', and M_S'' are the spin components of the $^6A_1$, $^4\Gamma$, and $^6T_1$ or $^4T_1$ states, θ, θ', and θ'' are the orbital components of the $^6A_1$, $^4\Gamma$, and $^6T_1$ or $^4T_1$ states, H_{SO} is the spin–orbit operator, and M_q is the electric dipole operator. Equation 4 contains the sum of two terms, the first involves SO mixing quartet ligand field character (from the $^4T_1$ excited state) into the sextet ground state, and the second involves SO mixing sextet charge transfer character (from a $^6T_1$ excited state) into the quartet ligand field excited states. The effects of each will be analyzed in turn.

The first term involves three components. The energy denominator corresponds to the experimentally observed $^6A_1 \rightarrow {}^4T_1{}^a$ transition energy. Since this transition in **1** and **2** is at a similar energy to that observed in ferric monomers,[25] the energy denominator cannot account for increased intensity. The first matrix element in the numerator involves spin–orbit coupling of the GS with the $^4T_1$ state, which is the only state allowed to mix into the $^6A_1$ GS by group theory.[66] This component also should not change from the monomer to dimer. The second matrix element in the numerator of the first term involves the electric dipole operator inducing a transition from the $^4T_1$ component SO mixed into the GS to the ligand field excited state ($^4\Gamma$). The irreducible tensor method can be used to separate this integral between two states into one-electron orbital components.[67] This requires the many electron wave functions for the ligand field states under consideration. The $^4T_1{}^a$ and $^4T_2{}^a$ transitions will be considered in detail since these transitions are observed experimentally and have clearly identifiable $S = 0$ intensity as described above. The many electron wave functions for the $^6A_1$ GS and $^4T_1{}^a$, $^4T_2{}^a$ ligand field excited states are[68]

$$|{}^6A_1\rangle = |yz,xz,xy,z^2,x^2 - y^2\rangle$$

$$|{}^4T_1{}^a,x\rangle = \frac{1}{2}|yz,\overline{yz},xz,xy,z^2\rangle - \frac{\sqrt{3}}{2}|yz,\overline{yz},xz,xy,x^2 - y^2\rangle$$

$$|{}^4T_1{}^a,y\rangle = -\frac{1}{2}|yz,xz,\overline{xz},xy,z^2\rangle - \frac{\sqrt{3}}{2}|yz,xz,\overline{xz},xy,x^2 - y^2\rangle$$

$$|{}^4T_1{}^a,z\rangle = -|yz,xz,xy,\overline{xy},z^2\rangle$$

$$|{}^4T_2{}^a,yz\rangle = \frac{\sqrt{3}}{2}|yz,\overline{yz},xz,xy,z^2\rangle + \frac{1}{2}|yz,\overline{yz},xz,xy,x^2 - y^2\rangle$$

$$|{}^4T_2{}^a,xz\rangle = \frac{\sqrt{3}}{2}|yz,xz,\overline{xz},xy,z^2\rangle - \frac{1}{2}|yz,xz,\overline{xz},xy,x^2 - y^2\rangle$$

$$|{}^4T_2{}^a,xy\rangle = -|yz,xz,xy,\overline{xy},x^2 - y^2\rangle \quad (5)$$

where the bar indicates that the orbital contains a spin down electron; otherwise, the electron is spin up. The matrix elements involving the electric dipole operator can be reduced as described in Griffith:[67]

$$\langle {}^4T_1 M_s''\theta''|M_q|{}^4\Gamma M'\theta'\rangle = \delta_{S''S''M''M'}[-1]^{T_1+\theta''} V\begin{bmatrix} T_1 & \Gamma & T_1 \\ -\theta'' & \theta' & n \end{bmatrix}\langle {}^4T_1||m||{}^4\Gamma\rangle \quad (6)$$

The double bars indicate reduced matrix elements. The phase factors and the V coefficient can be evaluated,[67] the latter to determine which components are group theoretically allowed. For example, a transition from the $^4T_1(x)$ component of the GS to the $^4T_1(y)$ excited state is z-polarized, and from inspection of the many electron wave functions in eq 5, this corresponds to the transition of a spin down electron from d_{yz} to d_{xz} ($^4T_1(y) \rightarrow {}^4T_1(x)$ is also z polarized and corresponds to a $d_{xz} \rightarrow d_{yz}$ transition). From the above observed experimental polarization in Figure 4, the $^6A_1 \rightarrow {}^4T_1{}^a$ transition is polarized predominantly along the Fe–oxo axis, i.e. the monomer z-axis. Therefore, only z-polarized transitions need to be considered. For the $^4T_1 \rightarrow {}^4T_1$ component of the $^6A_1 \rightarrow {}^4T_1{}^a$ transition, the two group theoretically allowed z-polarized one electron transitions involve $d_{yz} \rightarrow d_{xz}$ and $d_{xz} \rightarrow d_{yz}$. These same transitions are predicted for the $^4T_1 \rightarrow {}^4T_2$ component of the $^6A_1 \rightarrow {}^4T_2{}^a$ LF transition.

Finally the effect of the large anisotropic covalency of the iron–oxo bond on the intensity of these transitions in the dimer relative to a ferric monomer is considered. The coefficients of mixing from the BS–SCF–Xα–SW calculations in the Results section can be used to estimate the covalency in the orbitals under consideration. For these formally d → d transitions to have intensity, there must be some ligand character mixed into these orbitals from covalency.[69] The ligand orbital which mixes into both the donor and acceptor wave functions must be the same to give nonzero transition intensity.[70] This latter condition is not met. The d_{xz} (levels 47A″ and 23A″ in Table 3B) and d_{yz} (levels 63A′ and 31A′ in Table 3B) orbitals have significant oxo π character, but the oxo p_x and p_y orbitals are orthogonal. The $d_{xz} \rightarrow d_{yz}$ one electron transition is therefore predicted to have no z-polarized intensity and therefore cannot lead to intensity enhancement of the $^6A_1 \rightarrow {}^4T_1{}^a$, $^4T_2{}^a$ transitions in the dimer.

It should also be noted that these LF transitions are a combination of strong field configurations (e.g. t^4e, t^3e^2, t^2e^3).[65] An estimate of this breakdown for structure **1** from diagonalizing the Tanabe–Sugano matrices[49] with experimental estimates of the LF parameters ($Dq = 1290$ cm^{-1}, $B = 600$ cm^{-1}, $C = 2000$ cm^{-1}) is as follows:

$$^4T_1{}^a = -(0.984)^4T_1(t^4e^1) - (0.144)^4T_1(t^3e^2) + (0.101)^4T_1(t^2e^3)$$

$$^4T_2{}^a = (0.889)^4T_2(t^4e^1) - (0.374)^4T_2(t^3e^2) - (0.261)^4T_2(t^2e^3) \quad (7)$$

If the additional strong field configurations (t^3e^2, t^2e^3) are considered in the above analysis utilizing eq 6, this mechanism still cannot account for the intensity increase. While covalency

(65) Deaton, J. C.; Gebhard, M. S.; Solomon, E. I. *Inorg. Chem.* **1989**, *28*, 877–889.
(66) Schroeder, K. A. *J. Chem. Phys.* **1962**, *37*, 1587–1591.
(67) Griffith, J. S. *The Irreducible Tensor Method for Molecular Symmetry Groups*; Prentice-Hall, Inc.: Englewood, Cliffs, NJ, 1962.
(68) Meltzer, R. S. Thesis, University of Chicago, 1968.
(69) Ballhausen, C. J.; Liehr, A. D. *J. Mol. Spectrosc.* **1958**, *2*, 342–360.
(70) Avoird, A. V. D.; Ros, P. *Theor. Chim. Acta (Berl.)* **1966**, *4*, 13–21.

is necessary to observe intensity, the specific anisotropic covalency of the oxo bridge, which is unique in these dimers, cannot account for the increased intensity using only the first term of eq 4, which is usually dominant in monomer high spin d^5 complexes.

The second term in eq 4 will now be considered as a possible source of the increase in intensity of dimer LF transitions relative to these transitions in the monomer and of the difference between the $^6A_1 \rightarrow {}^4T_1{}^a$ and $^6A_1 \rightarrow {}^4T_2{}^a$ intensity. The energy denominator will make a marked contribution to the dimer intensity over that of the monomer. The charge transfer transitions of oxygen-coordinated monomeric ferric complexes start at approximately 39 000 cm^{-1}.[25] In contrast, the first assigned charge transfer band in these iron oxo dimers occurs at ~21 000 cm^{-1} (Figures 6 and 10 and Table 1). Using 10 000 cm^{-1} as an approximate $^6A_1 \rightarrow {}^4T_1{}^a$ transition energy and 15 000 cm^{-1} for the $^6A_1 \rightarrow {}^4T_2{}^a$ transition, the energy denominator alone (with the dipole strength a function of these terms squared) will account for a factor of 7 increase for the $^4T_1{}^a$ and a factor of 16 increase for the $^4T_2{}^a$ transition relative to the monomer. Another contribution to the second term in eq 4 is the electric dipole matrix element (first integral in numerator) for the $^6A_1 \rightarrow {}^6T_1$ charge transfer transitions which SO mix into the spin forbidden LF transitions. These CT transitions account for the parallel polarization of the LF transitions in the dimer, as we have found the low energy oxo $\rightarrow Fe^{3+}$ CT transitions to be parallel polarized (*vide infra*) and this polarization mixes into the LF dimer states. The remaining contribution, the second integral in the second term of eq 4 involves SO coupling between the $^6T_1$ CT state and each specific ligand field excited state. The matrix elements of SO coupling can be reduced according to Griffith:[67]

$$\langle {}^6T_1 M_s'' \theta'' | H_{so} | {}^4\Gamma M_s' \theta' \rangle = \bar{V} \begin{pmatrix} {}^5/_2 & {}^3/_2 & 1 \\ -M_s'' & M_s' & i \end{pmatrix} V \begin{pmatrix} T_1 & \Gamma & T_1 \\ -\theta'' & \theta' & -i \end{pmatrix} \times \sum_i (-1)^{i+1+5/2-M''} [-1]^{T_1+\theta''} \langle {}^6T_1 || \sum_{k=1}^{n} su(k) || {}^4\Gamma \rangle \quad (8)$$

The V coefficients are tabulated in ref 67 and $\bar{V}$ is equivalent to a $3-j$ symbol with the spin operator transforming as 1 with complex components of $(-1, 0, 1)$. This $3-j$ symbol is evaluated using ref 71. The reduced matrix element $\langle {}^6T_1 || \sum_{k=1}^{n} su(k) || {}^4\Gamma \rangle$ spin–orbit operator is written as a sum of the k one-electron operators. Since the energy denominator already accounts for much of the increased intensity, it is necessary to evaluate this reduced matrix element to determine if it is nonzero for the CT transitions of interest. The states in this reduced matrix element are a combination of the specific orbital configurations, i.e. $^6T_1$ ($t_1{}^5t_2{}^q e^p$) and $^4\Gamma$ ($t_2{}^{q'} e^{p'}$) where p, q, p', and q' are the electron occupancy of the d orbitals and t_1 is the ligand based orbital involved in the CT transition. The reduced matrix element in eq 8 can be simplified into a monoelectronic matrix element using the irreducible tensor method as described in Griffith.[67] Each strong field configuration (t^4e, t^2e^2, t^2e^3) mixed into the $^4\Gamma = {}^4T_1$ and $^4T_2$ states was considered. Since the lowest energy CT transitions which will lead to the energy denominator enhancement of intensity in eq 4 involve transitions to the t_2 d orbitals, only the $t_1{}^5t_2{}^4e^2$ CT configuration [oxo p (t_1) $\rightarrow$ Fe d (t_2) transition] is considered. Converting the reduced matrix element between states in eq 8 to monoelectronic reduced matrix elements between orbitals with eqs 10.14 and 10.17 of Griffith[67] gives

Table 5. One-Electron Wave Functions Describing Oxo Covalency

t_2 Metal Antibonding Orbitals
$|xz\rangle^* = (1-\beta^2)^{1/2} d_{xz} - \beta p_x$
$|yz\rangle^* = (1-\beta^2)^{1/2} d_{yz} - \beta p_y$
$|xy\rangle^* = d_{xy}$

e Metal Antibonding Orbitals
$|z^2\rangle^* = (1-\alpha^2)^{1/2} d_{z^2} - \alpha p_z$
$|x^2-y^2\rangle^* = d_{x^2-y^2}$

t_1 Ligand Bonding Orbitals
$|x\rangle = \beta d_{xz} + (1-\beta^2)^{1/2} p_x$
$|y\rangle = \beta d_{xz} + (1-\beta^2)^{1/2} p_y$
$|z\rangle = \alpha d_{xz} + (1-\alpha^2)^{1/2} p_z$

$$\langle (t_1{}^5t_2{}^4e^2)^6T_1 || \sum_{k=1}^{n} su(k) || (t_1{}^6t_2{}^4e^1)^4T_1 \rangle = \sqrt{2} \langle {}^1/_2 e || su || {}^1/_2 t_1 \rangle \quad (9a)$$

$$\langle (t_1{}^5t_2{}^4e^2)^6T_1 || \sum_{k=1}^{n} su(k) || (t_1{}^6t_2{}^4e^1)^4T_2 \rangle = \sqrt{2} \langle {}^1/_2 e || su || {}^1/_2 t_1 \rangle \quad (9b)$$

$$\langle (t_1{}^5t_2{}^4e^2)^6T_1 || \sum_{k=1}^{n} su(k) || (t_1{}^6t_2{}^3e^2)^4T_1 \rangle = -({}^1/\sqrt{2}) \langle {}^1/_2 t_2 || su || {}^1/_2 t_1 \rangle \quad (9c)$$

$$\langle (t_1{}^5t_2{}^4e^2)^6T_1 || \sum_{k=1}^{n} su(k) || (t_1{}^6t_2{}^3e^2)^4T_2 \rangle = ({}^1/\sqrt{2}) \langle {}^1/_2 t_2 || su || {}^1/_2 t_1 \rangle \quad (9d)$$

$$\langle (t_1{}^5t_2{}^4e^2)^6T_1 || \sum_{k=1}^{n} su(k) || (t_1{}^6t_2{}^2e^3)^4\Gamma \rangle = 0 \quad (9e)$$

These monoelectronic reduced matrix elements in eq 9a–d can be evaluated as described in section 13.4 of Piepho and Schatz.[72] The LCAO wave functions that are used are given in Table 5 where again, only the anisotropic covalency of the Fe–oxo bond is considered based on the z polarization of these oxo $\rightarrow$ Fe CT transitions. Note that while the preceding analysis is given in terms of O symmetry, the anisotropic nature of the oxo covalency require wave functions of C_{4v} symmetry. Upon evaluating these monoelectronic reduced matrix elements with the wave functions given in Table 5, the following are obtained:

$$\langle {}^1/_2 e || su || {}^1/_2 t_1 \rangle = 0 \quad (10a)$$

$$\langle {}^1/_2 t_2 || su || {}^1/_2 t_1 \rangle = -\sqrt{10}\beta(1-\beta^2)^{1/2}\zeta_{Fe} + \sqrt{10}\beta(1-\beta^2)^{1/2}\zeta_{oxo} \quad (10b)$$

Thus eq 10a, which involves the $p_{z'}$ and d_{z^2} orbitals, goes to 0, while eq 10b, which involves the $p_{x',y'}$ and $d_{x'z',y'z'}$ orbitals, is nonzero. The nonzero term in eq 10b becomes important only through the effects of covalency. (In the limit of no covalency $\beta = 0$ and eq 10b goes to 0). From this analysis, both $^4T_1{}^a$ and $^4T_2{}^a$ are enhanced, through mixing with higher energy strong field components as described in eq 7. Since $^4T_2{}^a$ contains a higher percentage of $t_2{}^3e^2$ character, it is preferentially enhanced. Squaring the ratio of the $t_2{}^3e^2$ coefficients for $^4T_2$ and $^4T_1$ leads

(71) Rotenberg, M.; Bivins, R.; Metropolis, N.; Wooten, J. K., Jr. *The 3-j and 6-j Symbols*; The Technology Press: Cambridge, MA, 1959.

(72) Piepho, S. B.; Schatz, P. N. *Group Theory in Spectroscopy*; John Wiley and Sons: New York, New York, 1983.

to another factor of 9 increase of intensity of the $^6A_1 \rightarrow {}^4T_2$ transition over $^6A_1 \rightarrow {}^4T_1$.

The second term in eq 4 therefore will make SO coupling the dominant intensity gaining mechanism due to the high covalency of the Fe−oxo bond and to the existence of low energy parallel polarized oxo → Fe^{3+} charge transfer transitions. The high covalency of this unit mixes metal and oxo character, thus enabling the SO coupling between quartet LF and sextet CT transitions to be non-zero from the evaluation of eq 8. The higher covalency also leads to these CT transitions being at low energy which provides for more efficient mixing. This mechanism also preferentially enhances the $^4T_2{}^a$ transition over the $^4T_1{}^a$ as is observed experimentally.

Since SO coupling is the source of the low temperature intensity, the temperature dependence for the $^4T_1{}^a$ transitions (Figure 4) could also be due to SO effects, as it has been found that the SO intensity of spin forbidden bands in a ferric monomer is dependent on the M_S value.[65] When the $S = 1$ component of the GS is populated (Figure 3), there could be a difference in intensity compared to the $S = 0$ component due to the SO intensity of the monomer M_S components of the $S = 1$ state. This mechanism was tested using the transition moments of the M_S monomer components derived in ref 65. The S_{Tot} GS components were divided into their respective monomer M_S components using $3 - j$ symbols:[73] In this analysis, only $S_{Tot} = 0, 1, 2$ were considered. The $3 - j$ symbols were evaluated using ref 71, and the combination of the M_S values on each Fe needed to give the S_{Tot} were obtained. The total intensity for S_{Tot} was calculated by summing the moments for the individual monomer M_S components on each iron and multiplying by the factor from $3 - j$ symbols. This calculated intensity corresponds to all of the SO intensity from the S_{Tot} component of the GS. This analysis predicts that the z polarized intensity from each S_{Tot} component is identical, i.e. that the total intensity from the $S = 0$ component of the GS from SO coupling is identical to the total intensity from the $S = 1$ and $S = 2$ components. Thus no temperature dependence is predicted from the single site SO mechanism in eq 4 in the dimer.

The temperature dependence of the intensity of the LF transitions must then be due to exchange relaxation of spin selection rules. The LF dimer excited states in Figure 3 are obtained by coupling the $S = {}^5/_2$ GS of one Fe with the $S = {}^3/_2$ of the other Fe which has undergone a spin forbidden LF transition. Thermal population of the triplet and quintet components of the GS leads to spin allowed transitions in Figure 3, $^3B_2 \rightarrow {}^3\Gamma$ and $^5A_1 \rightarrow {}^5\Gamma$ for each LF excited state $^4\Gamma$. The dimer selection rules can be obtained to correlate with the polarization of the observed triplet and quintet transitions. The symmetries of the LF dimer states are obtained by coupling two monomer transitions using the general approach described in ref 74. In this case the idealized dimer symmetry was assumed to be D_{4h} and the monomer site symmetry for ions A and B to be C_{4v}.

The selection rules for $^4T_1$, $^4T_2$, $^4A_1$, and ^4E monomer excited states of one Fe coupled to the $^6A_1$ GS of a second Fe are given in Table 6. Note that the O states are split in C_{4v} monomer symmetry. In particular, the $^4T_1$ splits into $^4A_2$ and ^4E states, the $^4T_2$ splits into $^4B_2$ and ^4E states, and the ^4E split into the ^4Eu and ^4Ev states. The leftmost columns give the selection rules for D_{4h} dimer symmetry. As described above, the majority of the temperature dependent intensity is observed along y (parallel polarized). In D_{4h} symmetry, the only y-polarized transition occurs for $^5A_{1g} \rightarrow {}^5A_{2u}$, where the $^5A_{2u}$ derives from the $^4A_1$ or ^4Eu C_{4v} monomer excited state. Thus D_{4h} dimer symmetry does not account for the y-polarized triplet intensity observed for the $^6A_1 \rightarrow {}^4T_1{}^a$ transition in Figure 4. The symmetry is then lowered to C_{2v}, which is the crystallographically imposed site symmetry of **1**, and these C_{2v} selection rules are shown in the middle of Table 6. For the $^6A_1 \rightarrow {}^4T_1{}^a$ transition (Figure 4A), only one band increases in intensity with increasing temperature, and from a Boltzmann analysis, it is mainly from the $S = 1$ component of the GS (Figure 4A, inset). Inspection of the C_{2v} selection rules in Table 6 yields one y (parallel polarized) $S = 1$ transition for the $^4T_1$ derived pair states ($^3B_2 \rightarrow {}^3A_1$). The observed y-polarized temperature dependent feature can be assigned to this $^3B_2 \rightarrow {}^3A_1$ transition. Referencing this dimer transition to the corresponding C_{4v} monomer transition, the $^3A_1$ dimer excited state is derived from the ^4E low symmetry split component of the monomer $^4T_1$ excited state. Since there is no temperature dependence observed for the $^6A_1 \rightarrow {}^4T_2{}^a$ transition (Figure 5), the exchange

Table 6. Dimer Selection Rules

Selection Rules for $^4T_1$ and $^4T_2$

D_{4h} (C_{4v} monomer source)	GS		C_{2v}	GS		C_2	GS	
	$^3A_{2u}$	$^5A_{1g}$		$^3B_2$	$^5A_1$		^3B	^5A
$^4T_1$ Dimer States								
$^3A_{1u}$ ($^4A_2$)	–	–	$^3A_2$	x	–	^3A	x,y	–
$^5A_{1u}$ ($^4A_2$)	–	–	$^5A_2$	–	–	^5A	–	z
$^3A_{2g}$ ($^4A_2$)	–	–	$^3B_1$	–	–	^3B	z	–
$^5A_{2g}$ ($^4A_2$)	–	–	$^5B_1$	–	x	^5B	–	x,y
^3E_u (^4E)	–	–	$^3A_1$	y	–	^3A	x,y	–
			$^3B_1$	–	–	^3B	z	–
^5E_u (^4E)	–	x,z	$^5A_1$	–	x	^5A	–	z
			$^5B_1$	–	z	^5B	–	x,y
^3E_g (^4E)	x,z	–	$^3A_2$	x	–	^3A	x,y	–
			$^3B_2$	z	–	^3B	z	–
^5E_g (^4E)	–	–	$^5A_2$	–	–	^5A	–	z
			$^5B_2$	–	y	^5B	–	x,y
$^4T_2$ Dimer States								
$^3B_{1u}$ ($^4B_2$)	–	–	$^3B_2$	z	–	^3B	z	–
$^5B_{1u}$ ($^4B_2$)	–	–	$^5B_2$	–	y	^5B	–	x,y
$^3B_{2g}$ ($^4B_2$)	–	–	$^3A_1$	y	–	^3A	x,y	–
$^5B_{2g}$ ($^4B_2$)	–	–	$^5A_1$	–	z	^5A	–	z
^3E_u (^4E)	–	–	$^3A_1$	y	–	^3A	x,y	–
			$^3B_1$	–	–	^3B	z	–
^5E_u (^4E)	–	x,z	$^5A_1$	–	x	^5A	–	z
			$^5B_1$	–	z	^5B	–	x,y
^3E_g (^4E)	x,z	–	$^3A_2$	x	–	^3A	x,y	–
			$^3B_2$	z	–	^3B	z	–
^5E_g (^4E)	–	–	$^5A_2$	–	–	^5A	–	z
			$^5B_2$	–	y	^5B	–	x,y

Selection Rules for $^4A_1$ and ^4E

D_{4h} (C_{4v} monomer source)	GS		C_{2v}	GS		C_2	GS	
	$^3A_{2u}$	$^5A_{1g}$		$^3B_2$	$^5A_1$		^3B	^5A
$^4A_1$ Dimer States								
$^3A_{2u}$ ($^4A_1$)	–	–	$^3B_2$	z	–	^3B	z	–
$^5A_{2u}$ ($^4A_1$)	–	y	$^5B_2$	–	y	^5B	–	x,y
$^3A_{1g}$ ($^4A_1$)	–	–	$^3A_1$	y	–	^3A	x,y	–
$^5A_{1g}$ ($^4A_1$)	–	–	$^5A_1$	–	z	^5A	–	z
^4E Dimer States								
$^3A_{2u}$ (^4E_u)	–	–	$^3B_2$	z	–	^3B	z	–
$^5A_{2u}$ (^4E_u)	–	y	$^5B_2$	–	y	^5B	–	x,y
$^3A_{1g}$ (^4E_u)	–	–	$^3A_1$	y	–	^3A	x,y	–
$^5A_{1g}$ (^4E_u)	–	–	$^5A_1$	–	z	^5A	–	z
$^3B_{2u}$ (^4E_v)	–	–	$^3A_2$	x	–	^3A	x,y	–
$^5B_{2u}$ (^4E_v)	–	–	$^5A_2$	–	–	^5A	–	z
$^3B_{1g}$ (^4E_v)	–	–	$^3B_1$	–	–	^3B	z	–
$^5B_{1g}$ (^4E_v)	–	–	$^5B_1$	–	x	^5B	–	x,y

(73) Zare, R. N. *Angular Momentum*; John Wiley and Sons: New York, New York, 1988; p 50.
(74) Hirst, L. L.; Ray, T. *Proc. R. Soc. London, A* **1982**, *384*, 191−203.

mechanism does not contribute to the spectra. The greatly enhanced $^4T_2{}^a$ SO intensity described above masks any additional intensity due to exchange. The $^4A_1$, ^4E transition in Figure 6A and Table 1 does not exhibit marked temperature dependence. Band 1 exhibits $S = 2$ temperature dependence and is only observed in y polarization. Band 3, which is an $S = 1$ transition, is both y and z polarized (Figures 6B,C). Inspection of Table 6 leads to the assignment of band 1 as a $^5A_2 \rightarrow {}^5B_2$ (y) transition and band 3 as $^3B_2 \rightarrow {}^3B_2$ (z) and $^3B_2 \rightarrow {}^3A_1$ (y) transitions. All of these dimer transitions can originate from either a $^4A_1$ or ^4Eu C_{4v} monomer excited state, with the dimer selection rules derived from both states accounting for the polarization of the observed temperature dependent features. From the second section of the Analysis, bands 1 and 3 in Table 1 can be assigned to components of the $^4A_1$ excited state, since the ^4Eu cannot account for the excited state exchange splitting. No definitive assignment is made for the $^4T_2{}^b$ transitions (bands 6 and 7 of Table 1) since these transitions overlap the oxo-CT manifold and not all features are resolved. This group theoretical analysis thus yields the observed polarization of temperature dependent intensity for structure **1** in C_{2v} symmetry. The exchange mechanism accounts for increased intensity based on the exchange coupling relaxation of the spin selection rules.

A formalism developed by Tanabe et al.[38] to describe ligand field excited state splitting (*vide infra*) can also be used to predict LF dimer intensity, for the spin flip transitions $^4A_1$, ^4E. If this is done, the ratio of $(S = 2)(S = 1)$ is predicted to be 30:7.[38] While there are errors in determining the area of these transitions due to overlapping features, from a Gaussian resolution of the solution spectrum and accounting for Boltzmann population, the observed intensity ratio of bands 1 and 3 (Figure 6A) is only 1.5:1. Therefore the SO intensity mechanism described in eq 5 also makes a large contribution to their intensity and parallel polarization.

For **2**, the $^4T_1{}^a$ LF region shows two transitions which have temperature dependent intensity (Figure 4B), as opposed to one transition observed above in **1**. The most intense transition and the transition that has the most temperature dependence (the low energy feature in Figure 4B) can be assigned to the $^3B_2 \rightarrow {}^3A_1$ dimer transition observed in **1** which was referenced as arising from the monomer ^4E excited state. The reason that it is observed at lower energy in **2** can be understood in terms of low symmetry splitting (see below). To account for the second temperature dependent feature, the dimer symmetry must be lowered to C_2, which is closer to the molecular symmetry of structure **2** (strictly C_1). Due to inequivalent equatorial bonds, the mirror plane is removed with the molecular C_2 still along the z-axis. The dimer selection rules for C_2 symmetry are shown in the last column of Table 6. When the symmetry is lowered, two additional y-polarized $S = 1 \rightarrow S = 1$ features are predicted, both involving $^3B \rightarrow {}^3A$ transitions. With respect to the C_{4v} monomer, one arises from the $^4A_2$ component of the low symmetry split $^4T_1$ and the other from the symmetric dimer component of the ^4E. On the basis of the low symmetry analysis below, the higher energy transition can be assumed to derive from the $^4A_2$ transition of the C_{4v} monomer.

Having used selection rules to assign the temperature dependence of these bands, we can now extend this analysis to the C_{4v} splitting for the octahedral monomer states. The broader more temperature dependent feature assigned to the $^6A_1 \rightarrow {}^4E$ component of the $^6A_1 \rightarrow {}^4T_1{}^a$ transition is lowest in energy for structure **2** and highest in energy in structure **1**. This can be accounted for by a description of this tetragonal splitting in terms of orbital splittings:[75]

$$\Delta(^4T_1) = {}^4E - {}^4A_2 = \delta + (3/4)\mu \tag{11}$$

where

$$\delta = E(d_{x'z'},d_{y'z'}) - E(d_{x'^2-y'^2}) \tag{12}$$

and

$$\mu = E(d_{x'y'}) - E(d_{z'^2}) \tag{13}$$

The ^4E level is highest in eq 11 when this splitting is positive. Using the results of BS−Xα−SW calculations (Table 3), we obtain the orbital energy differences δ and μ. In structure **2′**, δ and μ are 1322 and −3193 cm^{-1}, respectively, and in structure **1′**, they are 3426 and −2628 cm^{-1} (Table III). Equation 11 yields splittings of −1072 cm^{-1} (for **2′**) and 1455 cm^{-1} (for **1′**). While these splittings are less than what are observed experimentally, they do predict the observed reversal of the ^4E compared to the $^4A_2$. The energy reversal partially derives from the decrease in splitting of the $E(d_{x'y'}) - E(d_{z'^2})$, component upon bending. Some of the strong σ-antibonding interaction for the linear dimer is lost, and thus the $d_{z'^2}$ orbital is less destabilized.

This analysis can be extended to the $^4T_2{}^a$ transition, to determine the ordering of the low symmetry split C_{4v} components: $^4B_2$ and ^4E. In this case the splitting of the $^4T_2{}^a$ is described by[75]

$$\Delta(^4T_2) = {}^4E - {}^4B_2 = \delta - (3/4)\mu \tag{14}$$

where δ and μ are defined in eqs 12 and 13. The results of BS−Xα−SW calculations predict energy splittings of 3716 cm^{-1} for **2′** and 5397 cm^{-1} for **1′**. Therefore the ^4E component of the low symmetry split LF excited states will be observed at higher energy in both cases. This can be contrasted with the behavior of the low symmetry components of the $^4T_1{}^a$ described above. The behavior of the low symmetry components of these transitions thus accounts for differences between the $^4T_1{}^a$ and $^4T_2{}^a$ upon bending the Fe−O−Fe angle.

In summary, analysis of the two lowest energy ligand field transitions in these complexes has demonstrated that there are two sources of intensity gaining mechanisms in the dimer: enhanced spin−orbit coupling and a dimer exchange mechanism. The increase in intensity over the monomer at low temperature derives from the highly covalent oxo−Fe^{3+} bond in the dimer which provides low energy CT transitions and allows for significant mixing of Fe and oxo centers, thus making SO coupling of these sextet CT into the quartet LF states more efficient. This SO mechanism also accounts for the observed parallel polarization of transitions from the $S = 0$ components of the ground state at low temperature. The dimer exchange mechanism accounts for the increasing intensity with increasing temperature observed in these complexes. The selection rules for dimeric transitions also account for the polarization of the triplet and quintet transitions. The dimer exchange effect is masked in the $^4T_2{}^a$ transition due to its greater SO-induced intensity from the low energy oxo → Fe CT transitions.

II. Ligand Field Transitions: Dimer Exchange Splittings. The assignment of the sharp features in region II for structures **1** and **2** to different spin components of the same ligand field transition gives an experimental determination of the excited state ligand field exchange splitting. In particular the $^6A_1 \rightarrow {}^4A_1$, ^4E (bands 1 and 3, Table 1, Figure 6) and $^6A_1 \rightarrow {}^4T_1b$ (bands 6 and 7, Table 1, Figure 6) for structure **1** are assigned

(75) Goode, D. H. *J. Chem. Phys.* **1965**, *43*, 2830−2839.

Table 7. Coefficients Derived for Individual Ligand Field Excited State Pathways

	antiferro pathways			ferro pathways				linear antiferro pathways	
excited state	$J_{x'z'-x'z'}$	$J_{y'z'-z'^2}$	$J_{z'^2-y'z'}$	$J_{x'z'-z'^2}$	$J_{z'^2-x'z'}$	$J_{x'z'-y'z'}$	$J_{y'z'-x'z'}$	$J_{y'z'-y'z'}$	$J_{z'^2-z'^2}$
$^6A_1{}^4A_1$ (J_{ES}/J_{GS})	1.39	0.69	0.69	0.69	0.69	1.39	1.39	1.39	1.04
$^6A_1{}^4E_u$ (J_{ES}/J_{GS})	1.47	1.53	1.53	1.53	1.53	1.47	1.47	1.47	1.06

to triplet/quintet pairs. The $^6A_1 \rightarrow {}^4A_1$, ^4E for **2** also shows features assigned as a triplet and quintet (Figure 10). This striking energetic splitting can be resolved due to the sharpness of these features. The analysis of excited state splittings in these ligand field transitions gives insight into relative efficiencies of individual orbital exchange pathways in the Fe−O−Fe dimers.

The $^6A_1 \rightarrow {}^4A_1$, ^4E transition of structure **1** will be considered first. The observed spin state ordering with the $S = 2$ transition 1350 cm^{-1} below the $S = 1$ gives an effective excited state J^{LF} of 220 cm^{-1}, with the plus sign indicative of *ferromagnetism* in this excited state. Ferromagnetism has also been observed in the excited LF states of natural sapphires (i.e. Fe^{3+}/Al_2O_3).[76] The observed ferromagnetism implies that the orbital pathways involved in superexchange are significantly perturbed in this ligand field excited state. In high spin ferric dimers, the ground state J_{GS} has contributions from 25 orbital pathways involving all combinations of the five half-occupied d orbitals on each iron. This is described in eq 15,[38]where A and B refer to the

$$J^{GS} = J_{AB}(^6A_{1g}\,{}^6A_{1g}) = \frac{1}{25}\sum_{ij} J_{A_iB_j} \qquad (15)$$

two Fe atoms and i and j to their respective d orbitals. Most of these pathways will be ferromagnetic or 0 since they involve orbitals which do not overlap the bridging oxo or the pathway involves orthogonal p orbitals on the oxo bridge. Only a few key pathways have good overlap with the oxo bridge and promote strong antiferromagnetism. These antiferromagnetic pathways are described in the results of the SCF−Xα−SW calculations.

In order to probe the origin of the excited state splitting, the Tanabe model[38] of LF excited state exchange has been employed. This model was specifically developed to explain the LF dimer spectra of spin flip transitions which can be described using a spin Hamiltonian formalism. It has been applied mainly to the analysis of d^5 (Mn) and d^3 (Cr) systems where these spin flip transitions can be observed.[37] In this model new expressions for the excited state J values are derived. This has been done for the $^4A_1$, ^4E transition in d^5 systems, in particular for $^4A_1$ and the low symmetry split components of the ^4E, the ^4Ev and ^4Eu. In section I of the analysis, the ^4Ev case was ruled out as a possible assignment for these transitions based on its polarization, but $^4A_1$ and ^4Eu were indistinguishable from the selection rules. Therefore, since $^4A_1$ and ^4Eu assignments are possible, both states need to be considered in the application of the Tanabe model to the LF excited state splitting in order to gain insight into specific orbital pathways.

The equation of the excited state J values in terms of individual orbital pathways for each of these possible assignments can be determined from ref 38. From these expressions, the weighting coefficients for specific orbital pathways in the excited state relative the ground state are obtained. These ratios of the weighting coefficients define whether the contributions of these pathways are expected to increase or decrease upon excitation.[77]

The results of BS−SCF−Xα−SW calculations indicate that the antiferromagnetic pathways are the two π pathways and the σ pathway in the linear dimer, with the mixed π/σ pathways of $FeA(d_{y'z'})$ − $O(p_{y'})$−$FeB(d_{z'^2})$ and $FeA(d_{z'^2})$−$O(p_{z'})$−$FeB(d_{y'z'})$ (where the prime notation refers to the monomer coordinate frame in Figure 1) becoming important in the bent structure. The important ferromagnetic pathways are also assumed to involve these orbitals ($d_{x'z'}$, $d_{y'z'}$, $d_{z'^2}$) which have significant oxo character, but in pathways which involve orthogonal orbitals on the oxo bridge. The ferromagnetic orbitals are therefore Fe-($d_{x'z'}$)−Fe($d_{y'z'}$), Fe($d_{y'z'}$−Fe($d_{x'z'}$), Fe($d_{z'^2}$)−Fe($d_{x'z'}$), and Fe($d_{x'z'}$)−Fe($d_{z'^2}$).

The coefficients for these pathways derived for the $^6A_1 \rightarrow {}^4A_1$ and $^6A_1 \rightarrow {}^4Eu$ transition in the dimer are given in Table 7. To account for the observed ferromagnetism in the excited state, the coefficient of a strong antiferromagnetic pathway needs to decrease with a concomitant increase for a ferromagnetic pathway. While the coefficients for the $^6A_1 \rightarrow {}^4A_1$ transition both decrease and increase, those for the $^6A_1 \rightarrow {}^4Eu$ transition all increase. Since the ferromagnetic and antiferromagnetic pathways should be of the same order of magnitude (based on individual J values experimentally determined for other complexes),[41,78] these coefficients for the $^6A_1 \rightarrow {}^4Eu$ transition cannot account for the observed ferromagnetism. Bands 1 and 3 in Figure 6 can therefore be assigned to the $^6A_1 \rightarrow {}^4A_1$ transition, whose predicted change in orbital pathway J values upon excitation can account for their observed ferromagnetism. This is consistent with the results of previous studies which found the $^6A_1 \rightarrow {}^4A_1$ transition in Mn(II) dimers to be an order of magnitude more intense than the $^6A_1 \rightarrow {}^4E$ transition.[77]

An analysis of the $^6A_1 \rightarrow {}^4A_1$ coefficients provides insight into the relative strength of these pathways. The nine antiferromagnetic pathways and presumed important ferromagnetic-pathways are listed in Table 7 with their weighting coefficients. The mixed $FeA(d_{y'z'})$−$O(p_{y'})$−$FeB(d_{z'^2})$, $FeB(d_{y'z'})$−$O(p_{y'})$−$FeA(d_{z'^2})$, $FeA(d_{z'^2})$−$O(p_{z'})$−$FeB(d_{y'z'})$, and $FeB(d_{z'^2})$−$O(p_{z'})$−$FeA(d_{y'z'})$ antiferromagnetic pathways all show a decrease in their weighting coefficients from 1 to 0.69. The other antiferromagnetic pathways $Fe(d_{x'z'})$−$O(p_{x'})$−$Fe(d_{x'z'})$ and $Fe(d_{y'z'})$−$O(p_{y'})$−$Fe(d_{y'z'})$ increase in their coefficients from 1 to 1.39 while $FeA(d_{z'^2})$−$O(p_{z'})$−$FeB(d_{z'^2})$ increases to 1.04. The increase to 1.39 also occurs for the $FeA(d_{x'z'})$−$FeB(d_{y'z'})$ and $FeB(d_{x'z'})$−$FeA(d_{y'z'})$ ferromagnetic pathways with the other ferromagnetic pathways under consideration showing a decrease from 1 to 0.69. As stated above, the ferromagnetism of the $^4A_1$ excited state requires strong antiferromagnetic pathways to decrease and ferromagnetic pathways to increase. This occurs for the mixed π/σ antiferromagnetic pathways and the $Fe(d_{x'z'})$−$Fe(d_{y'z'})$ ferromagnetic pathways. Thus the J values for one or all of these interactions should make significant contributions to the total J_{GS}. This demonstrates the importance of the mixed $d\pi$−$d\sigma$ pathway as mediators of antiferromagnetic exchange as had been indicated by the BS−SCF−Xα−SW calculations and earlier considerations.[57]

Bands 5, 6, and 7 which are assigned to components of the $^6A_1 \rightarrow {}^4T_2{}^b$ transition also give an energy splitting in the excited state. Note that due to overlapping transitions, precise energies cannot be determined, but on the basis of estimates of the

(76) Ferguson, J.; Fielding, P. E. *Aust. J. Chem.* **1972**, *25*, 1371−1385.
(77) Ferguson, J.; Güdel, H. U.; Krausz, E. R.; Guggenheim, H. J. *Mol. Phys.* **1974**, *28*, 893−904.
(78) Dubicki, L. *Aust. J. Chem.* **1972**, *25*, 739−746.

difference in energy of bands 6 (triplet) and 7 (quintet), a J^{LF} of -495 is predicted for this ligand field excited state. Since this transition also involves an orbital change it is not analyzed in detail, but unlike for the $^4A_1$ transition, the individual J_{AB} pathways contributions to the singlet/triplet splitting are expected to be more efficient in the excited state and give the stronger observed antiferromagnetic coupling.

This analysis can now be applied to the absorption spectrum of **2** in Figure 10. The fact that with increasing temperature a shoulder grows in (21 600 cm^{-1}) to higher energy in this complex for the $^4A_1$ transition in the glass spectrum implies that this LF excited state exhibits antiferromagnetism in the more linear structure ($J_{LF} \sim -250$ cm^{-1}). As the Fe−O−Fe unit becomes linear the mixed $\pi-\sigma$ pathways are no longer as efficient as antiferromagnetic pathways for exchange. Instead the pure π and σ interactions should be dominant. From inspection of Table 7 for the $^4A_1$ excitation, the ratio of coefficients for the Fe($d_{z'^2}$)−Fe($d_{z'^2}$) and Fe($d_{y'z'}$)−Fe($d_{y'z'}$) pathways increase to 1.04 and 1.37 respectively. Thus antiferromagnetism is enhanced in the $^4A_1$ ligand field excited state in a more linear structure.

In summary, the ligand field transitions observed in region II clearly demonstrate an energetic splitting corresponding to different S_{Tot} components of the ES. This splitting can be observed due to their smaller bandwidth compared to the $^4T_1{}^a$ and $^4T_2{}^a$ transitions. An analysis of the $^4A_1$, ^4Eu transitions in the Tanabe formalism leads to an assignment of these features as $^6A_1 \rightarrow {}^4A_1$ transitions, which undergo excited state ferromagnetism in the bent structure. This analysis show that the strong individual antiferromagnetic contributions in the ground state are reduced in the excited state and these pathways are the $\pi-\sigma$ pathways. The observed ferromagnetism versus antiferromagnetism in the excited state splitting between structures **1** and **2** is due to the importance of these mixed pathways upon bending.

III. Oxo → Fe^{3+} Charge-Transfer Transitions: Excited-State Exchange. The unique low energy intense "dimer" transitions in region III (Figure 2A,B) are a spectral fingerprint of ferric oxo dimers,[2,24,36] since these features are not present in corresponding monomer Fe^{3+} spectra. The $[(EDTA)Fe^{3+}(H_2O)]^-$ monomer spectrum has only one broad band present at 38 700 cm^{-1},[79] while for Fe^{3+} doped into Al_2O_3 (with a concentration <0.02 which does not allow for significant pair formation) the absorption envelope begins at ~40 000 cm^{-1}.[25] Since the "dimer" bands appeared to be too low in energy to be assigned as monomeric CT transitions and too intense to be spin forbidden monomer ligand field transitions, they were originally assigned as simultaneous pair excitations (SPE) which overcame the spinforbiddeness of these transitions, but as discussed above, more recently have been assigned as oxo → Fe^{3+} CT transitions.[24] There are a number of interesting features to note about these oxo CT transitions. These transitions occur at much lower energy than those observed in monomeric complexes. Also, the temperature dependence exhibited by these transitions is very striking. This is clearest in the lowest energy CT transitions for **1** (21 500 cm^{-1} feature in Figure 2A) and for the transitions of **2** in Figure 2B (region II, the band at 25 000 cm^{-1}, and region III). As for the LF transitions (see Analysis, above), this temperature dependence arises from the Boltzmann population of components of the GS spin manifold and indicates that singlet CT transitions occur at much lower energy than the corresponding triplet. Another feature to note is the number of transitions exhibited in these spectra, particularly the presence of two low energy singlet CT transitions close in energy (split by 2100 cm^{-1}) in the spectrum of **1** [bands 2 (Figure 6C) and 4 (Figure 6A) and Table 1]. The BS−SCF−Xα−SW transition state calculations predict the oxo → Fe^{3+} CT transitions to occur at much higher energy than is observed experimentally (Table 5). This is in contrast to the carboxylate → Fe^{3+} CT transitions which are predicted from transition state calculations to be at 29 000 cm^{-1} (Table 5), where they are observed experimentally (the out of plane perpendicular polarized transitions in Figure 11A).

We begin by considering the oxo → Fe^{3+} CT assignment without the inclusion of dimer effects. From a BS−SCF−Xα−SW calculation on the bent (Fe−O−Fe angle = 120°) structure **1′**, we obtain the following energy ordering of the oxo → Fe^{3+} CT spectrum: the out of plane oxo $p_\pi \rightarrow$ Fe $d_{x'z'}$ transition is predicted to be lowest in energy, the in plane oxo $p_\pi \rightarrow$ Fe $d_{y'z'}$ next lowest and the in plane oxo $p_\pi \rightarrow$ Fe $d_{z'^2}$ transition next, as labeled in Figure 15B, center. The latter transition only has intensity in structures with a bent Fe−O−Fe angle which allows the oxo p_π and p_σ orbitals to overlap the Fe $d_{z'^2}$ and Fe $d_{y'z'}$ orbitals respectively. While this CT ordering is derived from the calculation on **1′** with an Fe−O−Fe angle of 120°, it could also be applied for structure **2** (with an angle of 165°) where the latter overlap will also occur, but to a lesser extent. This is similar to the qualitative assignment developed previously from a monomer CT analysis.[24] This CT assignment based on transition state calculations does not, however, account for the observed experimental features: in particular, the number of CT transitions (five in the spectrum of **2** in Figure 2B [regions II and III]), their temperature dependence, or their low energy.

The features described above can be explained based on a model which allows for a large antiferromagnetic splitting in the CT excited states. When one iron site of the dimer undergoes a CT transition, the resulting $^6\Gamma$ state couples with the other iron to produce an excited state spin manifold (Figure 3, top). The excited state, though, now contains an $S = 0$ component, derived from a single ion ligand → metal spin-allowed $^6A_1 \rightarrow {}^6\Gamma$ CT transition. The existence of an $S = 0$ component in the excited state allows for the possibility of spin-allowed transitions at low temperature. A qualitative estimate of the relative value of the charge transfer excited state exchange (J_{CT}) to the ground state (J_{GS}) can be obtained by considering the orbital interactions involved. The contour plot of the $d_{y'z'}$ orbital of FeB in the broken symmetry calculation of **2′** (Figure 16B) is used as an example. Following excitation from the oxo $p_{y'}$ orbital to the FeB $d_{y'z'}$ orbital, the unpaired electron on the oxo bridge now has direct overlap with the unpaired electron on the FeA $d_{y'z'}$ orbital. Since the ground state exchange coupling of metal electrons occurs indirectly through the bridging ligand, this excited state exchange with direct overlap should be much larger. With a large value of excited state antiferromagnetism (J_{CT}), the singlet CT transitions should be greatly stabilized in energy, thus accounting for the low energy of these observed transitions.

The symmetry of the S_{Tot} components in the excited state spin manifold can be obtained from a previously developed transition dipole vector coupling (TDVC) model.[8] For a high spin C_{4v} Fe^{3+} monomer, each oxo CT transition is predicted to have A_1 symmetry. In the C_{2v} dimer, the resulting dimer excited states have A_1 and B_2 symmetry (corresponding to the sym/antisym combinations of CT transitions to each iron) for each spin state.[40] Figure 3 gives the predicted 12 dimer CT transitions for each monomer CT transition. On the basis of the ground state J value, only transitions originating from the $S = 0$, 1, or 2 states are predicted to have any intensity from 4 to

(79) Schugar, H. J.; Hubbard, A. T.; Anson, F. C.; Gray, H. B. *J. Am. Chem. Soc.* **1969**, *91*, 71−77.

Scheme 1

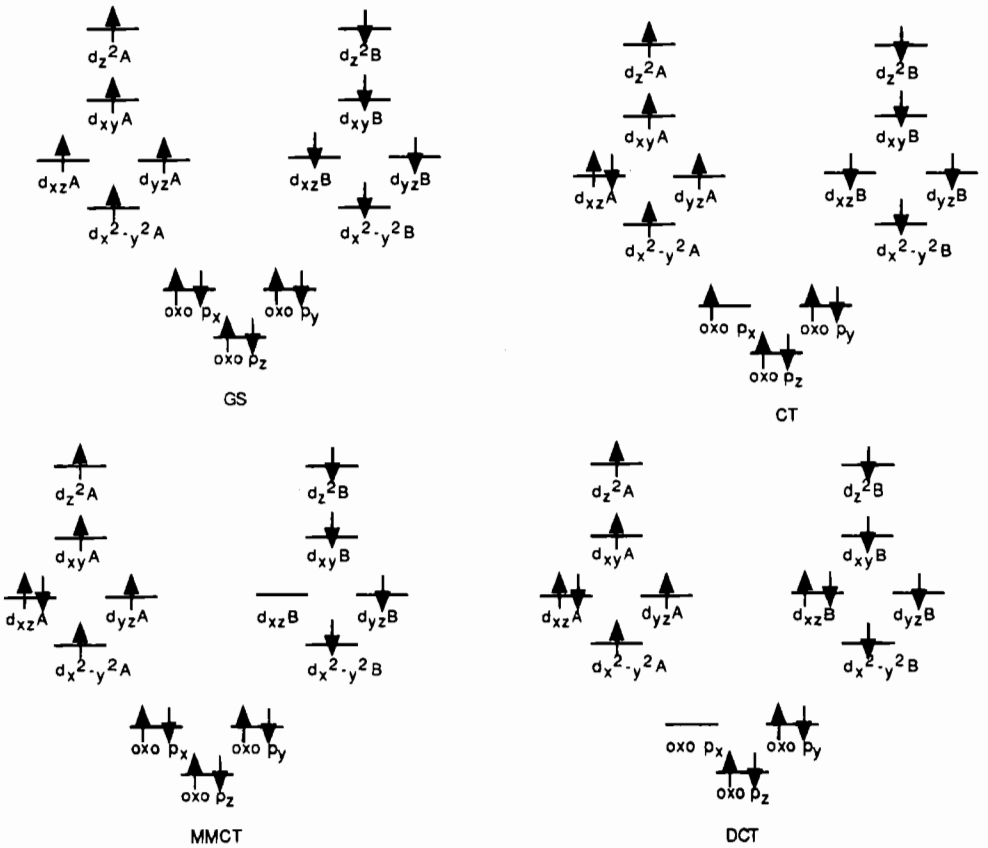

300 K. Only singlet and triplet behavior is observed experimentally. From the symmetry of the CT excited states, there should be one parallel to the Fe−Fe vector polarized transition (y) and an in plane perpendicular polarized transition (z) for each S_{Tot} transition, i.e. $^1A_1 \rightarrow {}^1B_2$ is parallel polarized and the $^1A_1 \rightarrow {}^1A_1$ is perpendicular polarized, and the $^3B_2 \rightarrow {}^3A_1$ is parallel polarized and the $^3B_2 \rightarrow {}^3B_2$ is perpendicular polarized. The TDVC model also provides an estimate of the relative intensities of these transitions as described below:[80]

$$\frac{I_Z}{I_Y} = \frac{(\bar{M}_1 + \bar{M}_2)^2}{(\bar{M}_1 - \bar{M}_2)^2} = \frac{\cos^2(\varphi/2)}{\sin^2(\varphi/2)} \qquad (16)$$

where $\bar{M}_1$ and $\bar{M}_2$ are the two dipoles corresponding to oxo CT transitions to either of the iron sites and φ is the angle between these two dipoles (in this case the Fe−O−Fe angle). Thus the parallel polarized features are predicted to be much more intense than the perpendicular polarized transitions, i.e. 3 times more intense for **1** with an angle of 120° and 50 times more intense for **2** with an angle of 165°. This TDVC model of exchange split dimer CT transitions thus accounts for the temperature dependence, number of transitions, and charge transfer splitting. A more quantitative description is given below.

In order to obtain quantitative insight into the observed CT excited state antiferromagnetism (ESAF) and thus make spectral assignments, a recently developed valence bond configuration interaction (VBCI) model will be employed. This model is similar to the cluster CI model applied in solid state materials.[81,82] In this VBCI formalism, starting from localized orbitals, delocalization is introduced through CI with metal to metal charge transfer (MMCT) states and is thus analogous to the Anderson theory of superexchange.[31] In the VBCI model, these MMCT states do not mix directly into the ground state; they instead CI mix into the bridging ligand to metal CT (LMCT) excited states which can then CI mix into the ground state. This mixing into the CT states is different for different spin states and thus accounts for the experimentally observed excited state antiferromagnetism (ESAF). The VBCI formalism also provides a model to relate the energy and splitting of oxo CT transitions to the ground state antiferromagnetism observed in these oxo bridged dimers.

A brief description of the VBCI analysis is given below and applied to the CT transitions observed in these systems. For simplicity, a linear dimer with C_{2v} molecular symmetry will be considered first, and then the analysis extended to a bent Fe−O−Fe dimer where new interactions can occur due to orbital mixing. The orbitals which will be the focus of this analysis are based on the atomic Fe d and oxo p orbitals of the Fe−O−Fe fragment. The relevant states are illustrated in Scheme 1. The $^1A_1$ ground state configuration is depicted first and shows the half-occupied d orbitals of interest and the filled oxo p orbitals. A LMCT transition, the oxo $p_x \rightarrow$ FeA d_{xz} CT is given next. Though there are six possible spin states which can be achieved (Figure 3); only the $M_S = 0$ state is shown. Also since each transition can be to either side of the dimer, the CT transition can produce states of A_1 and B_2 symmetry. The two other singlet states that can be reached from the LMCT state are a MMCT and double charge transfer, DCT, state (Scheme 1). The MMCT final state corresponds to a $d_{xzB} \rightarrow d_{xzA}$ MMCT transition. The DCT state is the singlet obtained from two oxo $p_x \rightarrow d_{xz}$ CT transitions. Note that the MMCT

(80) Solomon, E. I.; Tuczek, F.; Root, D. E.; Brown, C. A. *Chem. Rev.* **1994**, *94*, 827−856.
(81) Zaanen, J.; Sawatzky, G. A. *Can. J. Phys.* **1987**, *65*, 1262−1271.
(82) Shen, Z.; Allen, J. W.; Yeh, J. J.; Kang, J.-S.; W., E.; Spicer, W.; Lindau, I.; Maple, M. B.; Dalichaouch, Y. D.; Torikachvili, M. S.; Sun, J. Z.; Geballe, T. H. *Phys. Rev. B* **1987**, *36*, 8414−8428.

and DCT final states consist of two spin coupled $S = 2$ monomer units. Therefore the only spin components of the MMCT and DCT excited state spin manifold are $S = 0, 1, 2, 3, 4$.

Matrices can be set up to describe the configuration interaction among these states which leads to the LMCT excited state and GS antiferromagnetism. There are three oxo CT transitions which are predicted to have intensity based on overlap in the linear structure: $p_x \rightarrow d_{xz}$, $p_y \rightarrow d_{yz}$, and $p_z \rightarrow d_{z^2}$. Each of these can mix into the GS and for the linear case should not mix with one another. Three matrices will be required to obtain a complete description of the CT spectrum and estimate GS and excited state J values. The $^1A_1$ GS can have charge transfer transitions to states of $^1B_2$ (parallel polarization) and $^1A_1$ (perpendicular polarization) symmetry. Matrices of all $^1A_1$ and $^1B_2$ states are necessary to describe this CT spectrum, and the $^1A_1$ matrix will be needed to account for the $^1A_1$ GS stabilization. Since some of the necessary matrix elements will be obtained from HS calculations (see below), the high spin $^{11}B_2$ matrix also needs to be determined. The high spin component of the GS is $^{11}B_2$, and its energy separation from the $^1A_1$ GS is $30J$. This difference will be used to obtain estimates of J. In order to set up these matrices, the wave functions for each state need to be determined. Using Clebsh–Gordon coefficients, the wave functions for GS, CT, MMCT, and DCT states can be written in terms of slater determinants.[83] The coefficients for coupling two spin $^5/_2$'s are given in Rotenberg[71] or can also be determined from ref 84. These GS wave functions are listed in the supplementary material. The CT wave functions can be constructed by replacing the filled d orbital with the oxo p orbital which now contains the unpaired electron. Wave functions similar to those for the GS are obtained, but the delocalization of the CT excitation also needs to be taken into account.[39] The MMCT and DCT states are constructed by coupling two $S = 2$ monomer halves, d^6–d^4 or d^4–d^4. The appropriate Clebsh–Gordon coefficients for coupling two spin 2's are listed in ref 85, and functions similar to those derived by Glerup are obtained.[83]

The CI matrix for states of $^{11}B_2$ symmetry is given by:

$$\begin{vmatrix} 0 - E & h_{d_{xz}p_x} & h_{d_{yz}p_y} & h_{d_{z^2}p_z} \\ h_{d_{xz}p_x} & \Delta_{p_x-d_{xz}} - E & 0 & 0 \\ h_{d_{yz}p_y} & 0 & \Delta_{p_y-d_{yz}} - E & 0 \\ h_{d_{z^2}p_z} & 0 & 0 & \Delta_{p_z-d_{z^2}} - E \end{vmatrix} = 0 \quad (17)$$

where the diagonal elements denote the zeroth order CT energies (Δ) and $h_{d_ip_j}$ is the off-diagonal element of mixing. The subscripts are used to differentiate elements involving different orbitals, i.e. $\Delta_{p_x-d_{xz}} \equiv p_x \rightarrow d_{xz}$, etc. The energy of the GS is zero with no bonding (i.e. no CI). Note that no MMCT or DCT states exist in the $S_{Tot} = 5$ matrix; thus this component of the GS will not be as stabilized as the lower spin states where these additional states occur. Using the wave functions described above and assuming all $h_{d_ip_j}$ are initially equal, the mixing of the CT states into the GS can be determined. This off-diagonal element is defined in eq 18. The $h_{d_ip_j}$ depends on metal ligand

$$\langle {}^{11}B_2{}^{GS}|H|{}^{11}B_2{}^{CT}\rangle = 3\sqrt{2}\langle d_{iA}|h|p_j\rangle \equiv 3\sqrt{2}h_{d_{iA}p_j} = 3\sqrt{2}h_{d_{iB}p_j} \equiv h_{d_ip_j} \quad (18)$$

overlap and thus bonding. The Hamiltonian H is given by a sum of one-electron operators $h(i)$ and the electron–electron repulsion e^2/r_{ij}. Numerical values for the diagonal Δ and off-diagonal $h_{d_ip_j}$ elements now need to be determined. These parameters can be obtained from MO theory and a justification by relating VB to MO calculations is given in ref 39. The HS ($S = 5$) $M_S = 11$ wave function is identical to the VB high

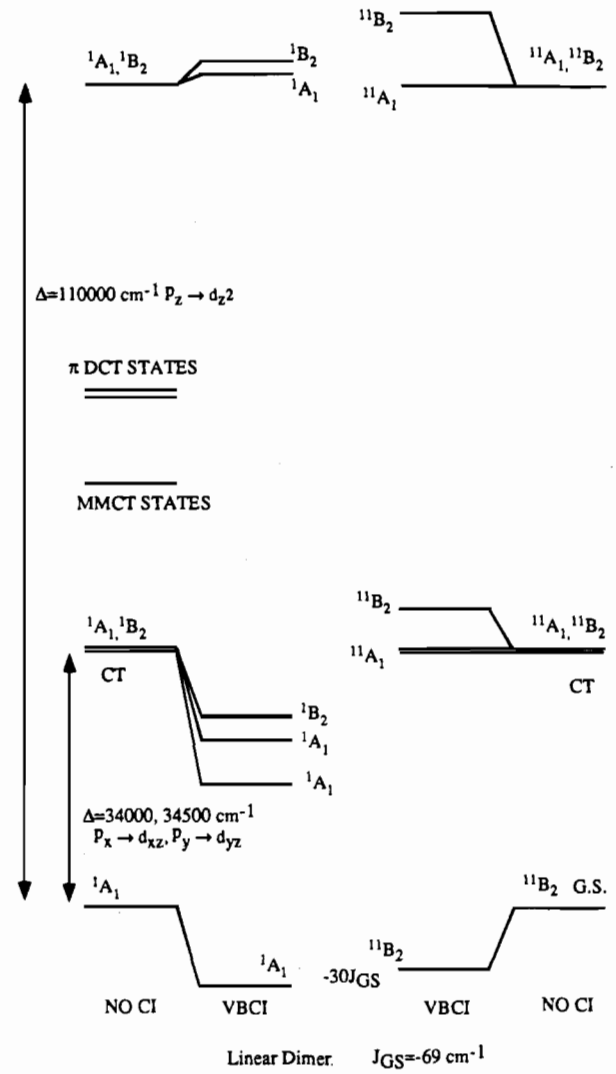

Figure 17. Energy level diagram giving the results of the VBCI analysis on the linear structure **2′**. The $S = 0$ singlet states are shown on the left side of the diagram (both $^1A_1$ and $^1B_2$), and the $S = 5$ states are shown on the right (both $^{11}B_2$ and $^{11}A_1$).

Table 8. VBCI Matrix Elements (cm^{-1})

VBCI	**2′** (linear)	**1′** (bent)
$h_{d_{xz}p_x}$	10 710	10 710
$h_{d_{yz}p_y}$	11 054	9 200
$h_{d_z^2p_z}$	18 570	15 500
$h_{d_z^2p_y}$	- - -	4 850
$h_{d_{yz}-p_z}$	- - -	8 060
$\Delta_{p_x-d_{xz}}$	34 000	33 000
$\Delta_{p_y-d_{yz}}$	34 500	41 000
$\Delta_{p_z-d_z^2}$	110 000	81 000
$\Delta_{p_y-d_z^2}$	- - -	60 000
$\Delta_{p_z-d_{yz}}$	- - -	70 500
U_{xz-xz}	56 450	56 450
U_{yz-yz}	56 450	56 450
$U_{z^2-z^2}$	56 450	56 450
U_{yz-z^2}	- - -	41 450
U_{z^2-yz}	- - -	71 540
DCT_{xz}	68 000	66 000
DCT_{yz}	69 000	82 000
DCT_{z^2}	220 000	162 000

(83) Glerup, J. *Acta Chem. Scand.* **1972**, *26*, 3775–3787.
(84) Melvin, M. A.; Swamy, N. V. V. J. *Phys. Rev.* **1957**, *107*, 186–189.
(85) Heine, V. *Group Theory in Quantum Mechanics*; Pergamon: London, 1959; p 432 ff.

spin state and thus provides a correct description of this state.[55,58] The corresponding HS CT states can also be shown to be equivalent to those from MO theory.[39] Therefore, the energies from the HS MO calculation (Table 5) can be used in this VB formalism.

From the $^{11}B_2$ GS, transitions to states of either $^{11}B_2$ or $^{11}A_1$ symmetry can occur. The $^{11}A_1$ states do not mix with the GS, thus their energies do not undergo any CI but their energies will be used to help determine matrix elements. The 4 × 4 matrix, eq 17, necessary to describe the $^{11}B_2$ HS mixing for these d^5–d^5 Fe–oxo dimers, cannot be solved explicitly for the six unknowns. Therefore each individual CT/GS interaction will first be considered separately. The zeroth order CT transitions would therefore be

$$\Delta = [\Delta E(^{11}A_1{}^{CT} - ^{11}B_2{}^{GS})] - [\Delta E(^{11}B_2{}^{CT} - ^{11}A_1{}^{CT})] \quad (19)$$

for each possible CT transition. The energies of $^{11}A_1{}^{CT}$ and $^{11}B_2{}^{CT}$ are determined directly from transition state calculations (Table 5). An estimate for $h_{d_ip_j}$ results from the following equation:[39]

$$2\sqrt{(\Delta/2)^2 + h_{d_ip_j}{}^2} = [\Delta E(^{11}A_1{}^{CT} - ^{11}B_2{}^{GS})] + [\Delta E(^{11}B_2{}^{CT} - ^{11}A_1{}^{CT})] \quad (20)$$

If the values obtained from eqs 19 and 20 are used as a starting point in eq 17, the $^{11}B_2$ CT energies obtained are much larger in energy than those from the HS calculation. This is due to the contribution of more than one pathway to the CI with the GS. Therefore, the initial $h_{d_ip_j}$ and Δ values were decreased in order to reproduce the $^{11}B_2$ CT transition state energies. The values estimated for $h_{d_ip_j}$ and Δ are given in Table 8. The two $^{11}B_2$ π CT transitions ($p_x \rightarrow d_{xz}$ and $p_y \rightarrow d_{yz}$), which are nearly degenerate in the transition state calculations, mix and split in energy in the VBCI matrices. In this case the average energies of the two mixed states were fit. The effects of the complete CI on the $^{11}B_2$ states relative to the unmodified $^{11}A_1$ states are illustrated in Figure 17, right. The $^{11}B_2$ GS is stabilized by 8455 cm^{-1}, while the $^{11}B_2$ CT states are all raised in energy. The Δ and $h_{d_ip_j}$ values determined above can now be used in the singlet CI matrices.

For the $^1A_1$ matrix, states of $^1A_1$ symmetry also exist for MMCT and DCT states. These are included in the matrix given in eq 21. The symbol U represents the MMCT transition energy and 2Δ represents the DCT state energy. The MMCT or DCT state is reached from each CT state by a new d to p one electron transition. The mixing element is given as a multiplicative factor (A) times the CT–GS mixing since the same type of transition $p \rightarrow d$ is involved. In the d^1–d^1 or d^9–d^9 case, the off-diagonal matrix element describing the mixing of the CT states into the GS is identical to the element describing the mixing of the MMCT states into the CT states, i.e. $A = 1$.[39] In d^5–d^5 dimers, this is no longer the case. The off-diagonal elements connecting the CT and MMCT states are weighted differently for each spin state. This difference is the source of the spin state splittings (Landé interval rule or exchange ladder) predicted by the spin Hamiltonian formalism. The A value for

Table 9. VBCI Results (cm^{-1})

	1′	2′
	GS VBCI Energies	
$^1A_1$	−10 465	−10 530
$^{11}B_2$	−8 345	−8 460
J_{GS}	−71	−69
	Oxo $p_x \rightarrow d_{xz}$ CT	
$^1A_1$	26 040	16 290 (π_1)
$^1B_2$	24 410	25 130 (π_1)
$^{11}B_2$	35 000	34 230
J_{CT}	−300	−600
$^1A_1 \rightarrow {}^1A_1$	36 915	26 820
$^1A_1 \rightarrow {}^1B_2$	34 875	35 660
% CT character in GS	34	39.8
	Oxo $p_y \rightarrow d_{yz}$ CT	
$^1A_1$	17 530	22 090 (π_2)
$^1B_2$	21 050	25 190 (π_2)
$^{11}B_2$	43 030	39 590
J_{CT}	−850	−590
$^1A_1 \rightarrow {}^1A_1$	28 000	32 620
$^1A_1 \rightarrow {}^1B_2$	31 515	35 720
% CT character in GS	28	44.6
	Oxo $p_z \rightarrow d_{z^2}$ CT	
$^1A_1$	93 050	111 460
$^1B_2$	101 745	113 130
$^{11}B_2$	84 230	122 520
J_{CT}	+295	−368
$^1A_1 \rightarrow {}^1A_1$	103 515	121 990
$^1A_1 \rightarrow {}^1B_2$	112 210	123 660
% CT character in GS	21	13.8
	Oxo $p_y \rightarrow d_{z^2}$ CT	
$^1A_1$	55 860	- - -
$^1B_2$	55 860	- - -
$^{11}B_2$	60 335	- - -
J_{CT}	−150	- - -
$^1A_1 \rightarrow {}^1A_1$	66 325	- - -
$^1A_1 \rightarrow {}^1B_2$	66 325	- - -
% CT character in GS	4	- - -
	Oxo $p_z \rightarrow d_{yz}$ CT	
$^1A_1$	72 765	- - -
$^1B_2$	89 330	- - -
$^{11}B_2$	71 240	- - -
J_{CT}	+50	- - -
$^1A_1 \rightarrow {}^1A_1$	83 230	- - -
$^1A_1 \rightarrow {}^1B_2$	99 795	- - -
% CT character in GS	12	- - -

$$\begin{vmatrix}
0-E & h_{d_{xz}p_x} & h_{d_{yz}p_y} & h_{d_{z^2}p_z} & 0 & 0 & 0 & 0 & 0 & 0 \\
h_{d_{xz}p_x} & \Delta_{p_x-d_{xz}}-E & 0 & 0 & Ah_{d_{xz}p_x} & 0 & 0 & A\sqrt{2}h_{d_{xz}p_x} & 0 & 0 \\
h_{d_{yz}p_y} & 0 & \Delta_{p_y-d_{yz}}-E & 0 & 0 & Ah_{d_{yz}p_y} & 0 & 0 & A\sqrt{2}h_{d_{yz}p_y} & 0 \\
h_{d_{z^2}p_z} & 0 & 0 & \Delta_{p_z-d_{z^2}}-E & 0 & 0 & Ah_{d_{z^2}p_z} & 0 & 0 & A\sqrt{2}h_{d_{z^2}p_z} \\
0 & Ah_{d_{xz}p_x} & 0 & 0 & U_{d_{xz}-d_{xz}}-E & 0 & 0 & 0 & 0 & 0 \\
0 & 0 & Ah_{d_{yz}p_y} & 0 & 0 & U_{d_{yz}-d_{yz}}-E & 0 & 0 & 0 & 0 \\
0 & 0 & 0 & Ah_{d_{z^2}p_z} & 0 & 0 & U_{d_{z^2}-d_{z^2}}-E & 0 & 0 & 0 \\
0 & A\sqrt{2}h_{d_{xz}p_x} & 0 & 0 & 0 & 0 & 0 & 2\Delta_{p_x-d_{xz}}-E & 0 & 0 \\
0 & 0 & A\sqrt{2}h_{d_{yz}p_y} & 0 & 0 & 0 & 0 & 0 & 2\Delta_{p_y-d_{yz}}-E & 0 \\
0 & 0 & 0 & A\sqrt{2}h_{d_{z^2}p_z} & 0 & 0 & 0 & 0 & 0 & 2\Delta_{p_z-d_{z^2}}-E
\end{vmatrix} = 0 \quad (21)$$

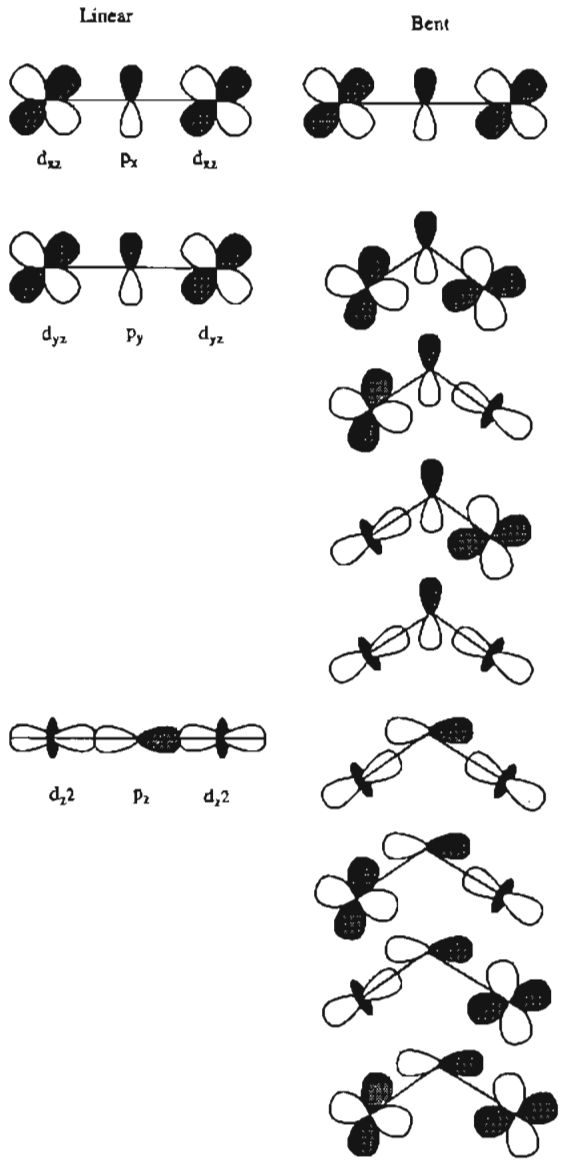

Figure 18. Diagrams of the major superexchange pathways in the Fe(III)−O−Fe(III) unit. The linear pathways are given on the left and the bent pathways are given on the right.

the singlet, which can be determined from the wave functions discussed above, is given by:

$$\langle {}^1B_2{}^{CT}|H|{}^1B_2{}^{MMCT}\rangle = \langle {}^1A_1{}^{CT}|H|{}^1A_1{}^{MMCT}\rangle = \frac{2\sqrt{3}}{5}h_{d_i p_j} \quad (22)$$

Due to the fact that there is no delocalization of the DCT states, a factor of $\sqrt{2}$ is also introduced in the CT−DCT mixing.

The Δ and $h_{d_i p_j}$ values in Table 8 were used in the $^1A_1$ matrix of eq 22. A value for U can be obtained from photoelectron spectroscopy.[39] A value of 7 eV has been used in these calculations.[86] The DCT energies are approximated by doubling the LMCT energies (Table 8). When the matrix is solved, the splitting for the $^1A_1$ states on the left side of Figure 17 is obtained. The $^1A_1{}^{GS}$ has been stabilized to $-10\,530$ cm^{-1}. The $^1A_1$ π CT states are also stabilized relative to the original Δ value, but the oxo p_z → Fe d_{z^2} energy has actually been destabilized since it is higher in energy than the MMCT value (Figure 17). The energy difference of the GS of this matrix and of the $^1B_2$ matrix gives an estimate of the GS J value: $^1B_2{}^{GS} - {}^1A_1{}^{GS} = -30J_{GS}$. The calculated energies for the linear Fe−O−Fe unit gives $J_{GS} = -69$ cm^{-1} which can be compared to the experimental value for **2**, with an angle of 165°, of -95 cm^{-1}. In an analogous manner, the charge transfer J_{CT} is defined to be $^1B_2{}^{CT} - {}^1A_1{}^{CT} = -30J_{CT}$. These values are included in Table 9. The eigenvectors determined from the matrix gives the breakdown of each state's contribution to each eigenvalue. The amount of each CT mixed into the resulting GS eigenvector are normalized for easier comparison and are listed in Table 9 (Structure **2'**). These values should also give an estimate of the antiferromagnetic pathway which also depends on metal ligand overlap. All three CT states mix into the GS with the π mixing larger than the σ (40 and 45% for the π CT transitions compared to 14% for the σ CT transition). This is similar to the results from the energy differences of the HS d orbital splittings described above in the Calculations Results section.

While the above matrices offer insight into the relative efficiencies of the pathways and the source of GS and CT antiferromagnetism, the $^1A_1$ CT states are not the states that dominate the observed CT spectra. The parallel polarized singlet CT states are the $^1A_1$ → $^1B_2$ transitions, so states of $^1B_2$ symmetry also need to be considered. The $^1B_2$ CI matrix is given in eq 23. Note that this matrix is similar to that for $^1A_1$, eq 21, except that there is no singlet GS or DCT state of B_2 symmetry. Using the CT zeroth energies and $h_{d_i p_j}$ values described above, the $^1B_2$ energies are obtained. The derived CT values are included in Figure 17, left, with the energies listed in Table 9. Consistent with experiment, the π CT states are stabilized in energy. The energy of the CT transitions observed in parallel polarization can be obtained from the energy difference between the $^1B_2$ CT and $^1A_1$ GS. The VBCI calculated energies for the $^1A_1$ → $^1B_2$ components of the p_x → d_{xz} and p_y → d_{yz} transitions are 35 660 and 35 720 cm^{-1} respectively. While there are no linear experimental transition energies to compare to, these values are within the range of the lowest observed CT transitions in structures **1** and **2** at ~21 000 cm^{-1}. The values are somewhat larger than experiment, as has been previously observed in the VBCI analysis of CT transitions of Cu dimers.[39] They are, however, a considerable improvement (~20 000 cm^{-1} lower in energy) over the BS calculations which do not include ESAF.

This VBCI analysis can now be extended to the bent Fe−O−Fe dimer. The linear pathways are shown on the left in Figure 18 for reference, while those on the right give the new orbital pathways that occur upon bending. The out of plane π interactions are identical, but the in plane π (d_{yz}) and σ (d_{z^2}) orbital interactions become mixed. For the in plane π oxo p_y orbital, there are two possible CT transitions: p_y → d_{yz} and p_y → d_{z^2}. Thus a new CT transition, the p_y → d_{z^2} CT needs to be added to the VBCI matrices described above. Assuming that the CT transition is localized on the left side of the dimer, the resulting unpaired electron on the oxo can then overlap either the d_{yz} or d_{z^2} orbital on the right side of the dimer. This latter interaction with the right side of the dimer is described by the MMCT or DCT mixing with the CT states in the VBCI matrices. If the new interactions are considered, a new MMCT state can be obtained from this CT transition, formally a d_{yzA} → d_{z^2B} transition. Inspection of the p_z pathways in Figure 18 also shows that another CT transition (p_z → d_{yz}) needs to be considered. In parallel, a new MMCT transition, d_{z^2A} → d_{yzB} is also obtained. The matrices for the bent structure are constructed in a manner analogous to that for the linear structure, and that for the $^1B_2$ state is given in eq 24 with the $^1A_1$ and $^1B_2$ matrices included as supplementary material. The linear $h_{d_i p_j}$ values in Table 9

(86) Fujimori, A.; Saeki, M.; Kimizuka, N.; Taniguchi, M.; Suga, S. *Phys. Rev. B* **1986**, *34*, 7318−7328.

$$\begin{vmatrix} \Delta_{p_x-d_{xz}} - E & 0 & 0 & Ah_{d_{xz}p_x} & 0 & 0 \\ 0 & \Delta_{p_y-d_{yz}} - E & 0 & 0 & Ah_{d_{yz}p_y} & 0 \\ 0 & 0 & \Delta_{p_z-d_{z^2}} - E & 0 & 0 & Ah_{d_{z^2}p_z} \\ Ah_{d_{xz}p_x} & 0 & 0 & U_{d_{xz}-d_{xz}} - E & 0 & 0 \\ 0 & Ah_{d_{yz}p_y} & 0 & 0 & U_{d_{yz}-d_{yz}} - E & 0 \\ 0 & 0 & Ah_{d_{z^2}p_z} & 0 & 0 & U_{d_{z^2}-d_{z^2}} - E \end{vmatrix} = 0 \quad (23)$$

$$\begin{vmatrix} 0 - E & h_{d_{xz}p_x} & h_{d_{yz}p_y} & h_{d_{z^2}p_z} & h_{d_{z^2}p_y} & h_{d_{yz}p_z} \\ h_{d_{xz}p_x} & \Delta_{p_x-d_{xz}} - E & 0 & 0 & 0 & 0 \\ h_{d_{yz}p_y} & 0 & \Delta_{p_y-d_{yz}} - E & 0 & 0 & 0 \\ h_{d_{z^2}p_z} & 0 & 0 & \Delta_{p_z-d_{z^2}} - E & 0 & 0 \\ h_{d_{z^2}p_y} & 0 & 0 & 0 & \Delta_{p_y-d_{z^2}} - E & 0 \\ h_{d_{yz}p_z} & 0 & 0 & 0 & 0 & \Delta_{p_z-d_{yz}} - E \end{vmatrix} = 0 \quad (24)$$

will be used as starting points to evaluate the above matrices for the bent calculation. The $h_{d_{xz}p_x}$ is set equal to that of the linear case, 10 710 cm^{-1}. The off-diagonal elements for the p_y and p_z orbitals need to be distributed among the new CT transitions, e.g. the linear $h_{d_{yz}p_y}$ ($p_y \rightarrow d_{yz}$) will be divided into the bent $h_{d_{yz}p_y}$ ($p_y \rightarrow d_{yz}$) and $h_{d_{z^2}p_y}$ ($p_y \rightarrow d_{z^2}$) elements. This is done according to the angular overlap model.[87] For an Fe–O–Fe angle of 120°, the overlap of the oxo p_y orbital and Fe d_{yz} orbital is 0.75 and that of the oxo p_y and Fe d_{z^2} is 0.25. Since it is the square of the off-diagonal element that is important in perturbation theory, the initial $h_{d_ip_j}$ values used were $h_{d_{z^2}p_y} = (0.25(h_{d_{yz}p_y})_{linear}^2)^{1/2}$ and $h_{d_{yz}p_y} = (0.75(h_{d_{yz}p_y})_{linear}^2)^{1/2}$. These values led to a much larger value for J_{GS} which does not match the experimental trend observed in Fe–oxo dimers.[88,89] Therefore, these values were then varied (lowered) to reproduce the lack of angle dependence of the GS J value. Once $h_{d_ip_j}$ values were obtained (Table 8), the Δ energies were then varied to reproduce HS $^{11}B_2$ CT transition energies for the SCF–Xα–SW bent calculation (Table 5). The U values were those used previously with the new $d_{yz} \rightarrow d_{z^2}$ MMCT at 15 000 cm^{-1} ($\sim 10Dq$) higher energy and the $d_{z^2} \rightarrow d_{yz}$ MMCT lower in energy by the same amount. The DCT values were again assumed to be twice the Δ values. A summary of all matrix element energies are given in Table 8.

Using the Δ and $h_{d_ip_j}$ values determined above, the bent matrices were evaluated and the splitting pattern for the CT transitions shown in Figure 19 is obtained. The energies of the $^1A_1$, $^1B_2$, and $^{11}B_2$ CT states are given in Table 9. The GS state energies are used to give an estimate of J_{GS} of -71 cm^{-1} which is somewhat lower than the experimental value of -120 cm^{-1} for **1**. The J_{CT} values estimated for the five oxo CT transitions are listed in Table 9 and are addressed below. The calculated singlet charge transfer energies ($^1A_1 \rightarrow {}^1B_2$, and $^1A_1 \rightarrow {}^1A_1$) are also listed in Table 9. The values for the two lowest energy parallel polarized transitions are 31 515 and 34 875 cm^{-1} which are much lower than that predicted by BS calculations which neglect ESAF (47 960 and 58 880 cm^{-1}), but somewhat larger than the experimentally observed values of 21 000 and 25 960 cm^{-1}.

The coefficients of the GS eigenvector give the amount of mixing of each CT transition into the GS. This should reflect the relative efficiencies of the antiferromagnetic pathways. These have been normalized to 100% and are listed in Table 9. Comparison to the linear calculations shows that the out of plane

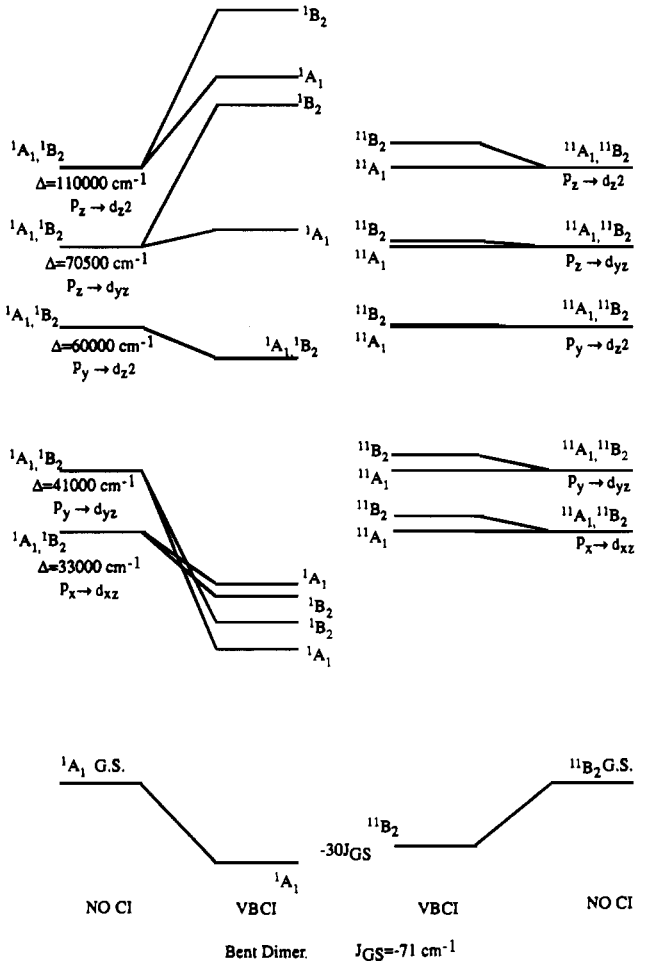

Figure 19. Energy level diagram giving the result of the VBCI analysis on the bent structure **1'**. The $S = 0$ states are given on the right and the $S = 5$ states are given on the left.

π oxo $p_x \rightarrow$ Fe d_{xz} CT mixing into the GS is mostly unaffected by bending. The in plane π CT ($p_y \rightarrow d_{yz}$) mixing has decreased from the linear value and the σ CT ($p_z \rightarrow d_{z^2}$) mixing has increased somewhat. The two new mixed π/σ CT transitions ($p_y \rightarrow d_{z^2}$ and $p_z \rightarrow d_{yz}$) also make contributions, with the $p_z \rightarrow d_{yz}$ CT transition making a larger contribution.

This VBCI analysis also provides a framework to describe the CT excited state antiferromagnetism. The excited state splitting is due to CI mixing of MMCT and DCT states. This stabilizes the singlet (and triplet) CT transitions and accounts for their low transition energy. *Due to larger excited state*

(87) Larsen, E.; La Mar, G. N. *J. Chem. Educ.* **1974**, *51*, 633–640.
(88) Haselhorst, G.; Wieghardt, K.; Keller, S.; Schrader, B. *Inorg. Chem.* **1993**, *32*, 520–525.
(89) Gorun, S. M.; Lippard, S. J. *Inorg. Chem.* **1991**, *30*, 1625–1630.

Table 10. Oxo CT Assignments (cm^{-1})

assignt	structure **1**	structure **2** (glass)	structure **2** (solid)
	Oxo $p_y \rightarrow d_{yz}$ CT Manifold		
$^1A_1 \rightarrow {}^1A_1$	18 400	not obs	not obs
$^1A_1 \rightarrow {}^1B_1$	20 500	25 600	20 750
$^3B_1 \rightarrow {}^3A_1$	not obs	29 350	~25 000
J_{CT}		−1 970	(−2 000) est.
	Oxo $p_x \rightarrow d_{xz}$ CT Manifold		
$^1A_1 \rightarrow {}^1B_1$	25 960	32 700	28 000
$^3B_1 \rightarrow {}^3A_1$	28 370	36 650	31 750
J_{CT}	−1 325	−2 070	−1 875
	Oxo $p_y \rightarrow d_{z^2}$ CT Manifold		
$^1A_1 \rightarrow {}^1B_1$	39 100	42 000	35 530

exchange, the in plane $\pi p_y \rightarrow d_{yz}$ *CT transition is stabilized below the out of plane* π *transition* (Table 9 and Figure 19). This is contrary to what is predicted in Figure 15B from the BS−SCF−Xα−SW calculations which do not include dimer effects. The experimental transition energy ordering predicted from the above VBCI analysis is $p_y \rightarrow d_{yz} < p_x \rightarrow d_{xz} < p_y \rightarrow d_{z^2}$. The results of the above analysis, in particular the new experimental CT ordering, will now be used in the assignment of the experimental excited state CT spectrum.

The solution spectrum of **2**, with Fe−O−Fe angle = 165° (Figure 2B), exhibits the cleanest temperature dependence throughout this CT region, so the transitions in Figure 2B will be analyzed first. These assignments will then be applied to the single crystal CT spectrum of **1** (Figures 11A and 6). The two lowest energy CT transitions in Figure 2B occur at 25 600 cm^{-1} and 29 350 cm^{-1}. These transitions follow singlet and triplet temperature dependence respectively and are assigned as the excited state exchange split components of the in plane π oxo $p_y \rightarrow$ Fe d_{yz} transition, since this is the transition predicted to be lowest in energy from the VBCI analysis. Only the parallel polarized features are observed ($^1A_1 \rightarrow {}^1B_2$ and $^3B_2 \rightarrow {}^3A_1$), since the corresponding perpendicular transitions are predicted to be much lower in intensity from eq 16. This singlet/triplet splitting can be used to obtain an experimental estimate of the excited state exchange parameter J_{CT} of -1995 cm^{-1}, where J_{CT} is defined to be half the energy difference between the $^1A_1 \rightarrow {}^1B_2$ and $^3B_2 \rightarrow {}^3A_1$ transitions, and accounting for the GS splitting. (Note that the sym/antisym splitting has not been taken into account since the $^1A_1 \rightarrow {}^1A_1$ and $^3B_2 \rightarrow {}^3B_2$ components are not observed.) This experimental J_{CT} value for **2** is 20 times greater than its experimental J_{GS} of -95 cm^{-1}. As described above, this can be attributed to the direct overlap of the unpaired oxo p electron with the half-filled Fe orbitals not involved in the CT transition. This above CT assignment for **2** can now be applied to the lowest energy CT transitions of **1**. From Table 1, there are two low energy singlet CT transitions very close in energy. The most intense singlet transition at 20 500 cm^{-1} can be assigned to the parallel polarized ($^1A_1 \rightarrow {}^1B_2$) oxo $p_y \rightarrow$ Fe d_{yz} transition, with the in plane perpendicular polarized transition at 18 400 cm^{-1} assigned to the corresponding $^1A_1 \rightarrow {}^1A_1$ CT. This gives an experimentally determined sym/antisym splitting of 2100 cm^{-1}. The correct experimental trend, with the $^1A_1 \rightarrow {}^1A_1$ transition lowest in energy, is also predicted from the VBCI analysis (Table 10, $p_y \rightarrow d_{yz}$) but with a somewhat larger splitting of 3515 cm^{-1}. The corresponding triplet transition overlaps the higher energy CT transitions.

The next higher energy transitions of **2** in Figure 2B occur at 32 500 and 36 650 cm^{-1}, respectively, and are assigned as components of the out of plane oxo $p_x \rightarrow$ Fe d_{xz} transitions. Again these two transitions follow singlet and triplet temperature dependence, respectively, and yield an experimentally determined J_{CT} of -2070 cm^{-1}. In parallel, the band at 26 000 cm^{-1} in structure **1** (Figure 11A) is assigned as a singlet and the next highest energy parallel polarized transition at 28 500 cm^{-1} assigned as the corresponding triplet. These features do not show the marked temperature dependence exhibited by **2**. This difference in temperature dependence between the two compounds is likely due to overlapping features, i.e. the bridging acetate $\rightarrow Fe^{3+}$ CT transition in structure **1** (Figure 11A, *x* polarization). This singlet/triplet energy splitting for **1** yields an out of plane π J_{CT} estimate of -1325 cm^{-1}. Even though the VBCI derived J_{CT} values are lower than the observed experimental values, they do predict the correct experimental trends of a decrease in excited state splitting for the oxo $p_x \rightarrow$ Fe d_{xz} CT on decreasing the Fe−O−Fe angle. The last feature in Figure 2B at 42 000 cm^{-1} shows singlet temperature dependence and is assigned to the oxo $p_y \rightarrow$ Fe d_{z^2} transition. No higher energy features can be unambiguously identified from the data obtained. A similar feature at 39 100 cm^{-1} is assigned in the spectrum of **1** (Figure 11A). A summary of these assignments is given in Table 10.

The CT assignment for **2** described above is based on the solution spectrum since variable temperature data could not be obtained for the crystalline sample in the higher energy region. But the LiCl glass gives rise to band shifts, as exhibited in the crystal/glass comparison of structure **2** in Figure 10. Therefore, the above assignment will also be applied to the structurally characterized solid spectrum. The first CT transition occurs at 21 000 cm^{-1} in Figure 10 (crystal). Since the temperature dependence of this transition is singlet in nature, this band is assigned as the $^1A_1 \rightarrow {}^1B_2$ component of the $p_y \rightarrow d_{yz}$ transition. The corresponding triplet is overlapped by the large intense features in this region (~25 000 cm^{-1} using the splitting from the glass spectrum). The next highest energy parallel polarized transition occurs at 28 000 cm^{-1} and is assigned as the $^1A_1 \rightarrow {}^1B_2$ component of the $p_x \rightarrow d_{xz}$ transition with the triplet transition occurring at 31 750 cm^{-1}. This gives an excited state exchange estimate of -1970 cm^{-1}. The next highest polarized transition occurs at 35 530 cm^{-1} and analogous to the assignment of the feature at ~42 000 cm^{-1} in the solution spectrum of **2** can be assigned to the $^1A_1 \rightarrow {}^1B_2$ component of $p_y \rightarrow$ Fe d_{z^2} transition.

A summary of the experimentally determined J_{CT} values are also given in Table 10. Note that the symmetric/antisymmetric splittings are not factored out of the observed state splittings since they are not obtained experimentally for most of these transitions. These CT excited state exchange values are an order of magnitude greater than the GS *J* values. This large excited state J_{CT} accounts for the low energy of these CT transitions relative to those of Fe^{3+} monomers. Qualitatively, these J_{CT}, which depend on metal ligand overlap, should reflect the individual orbital pathway contributions in the GS as well. This relationship is explored in the Discussion.

Discussion

The Iron−Oxo Dimer Bond. A combination of complementary experimental and theoretical methods have been employed to obtain a detailed description of the electronic structure of the Fe(III)−O−Fe(III) bond. A key feature of the experimental work has been the identification and assignment of oxo $\rightarrow Fe^{3+}$ CT transitions which dominate the absorption spectrum in regions II and III in Figure 2. The excited state splittings present in these CT transitions can also be used to probe the antiferromagnetism present in the CT excited states and its relationship to ground state antiferromagnetism (GSAF). The low energy of the oxo $\rightarrow Fe^{3+}$ CT transitions also accounts

for the increased intensity of the LF transitions in these dimers compared to monomeric species. Excited state splitting of the LF transitions have also been analyzed and related to GSAF.

The intense low energy absorption bands present in the spectra of oxo-bridged ferric dimers have been assigned as components of the bridging oxo-CT manifold. These features are much lower than monomeric CT transitions and from what is predicted from BS−SCF−Xα−SW calculations. This stabilization is due to CT excited state antiferromagnetism (ESAF). ESAF not only accounts for the energy stabilization of these transitions, but it also explains the observed temperature dependence and excited state splittings. In the valence bond configurational interaction (VBCI) model, this ESAF is the result of CI from higher energy excited states, i.e. MMCT and DCT states. These CT states are also the intermediate states involved in the superexchange coupling of the two Fe atoms. Figure 18 delineates the superexchange pathways involved in both linear (left) and bent (right) structures. The superexchange pathway involves an oxo p → metal d_A transition, followed by either a metal d_B → oxo p transition, or oxo p → metal d_B transition, Scheme 1. These latter MMCT and DCT states mix into the lower spin states to varying degrees to give the observed spin ladder (Figure 3). There is no MMCT or DCT state of $S = 5$, so the high spin CT state is not stabilized in energy. The observation of exchange-stabilized CT transitions therefore allows one to probe individual superexchange pathways involved in ground state antiferromagnetism.

The VBCI analysis gives insight into the relative strength of the antiferromagnetic pathways in the ground state. The amount of each CT transition mixed into the GS for the linear (**2′**) and bent (**1′**) case are included in Table 10. In the linear case the three oxo CT transitions should reflect the efficiencies of the three antiferromagnetic pathways. The π CT transitions mix dominantly into the GS with mixing values of 40 and 45% compared to 13% for the σ pathway. This is consistent with the orbital splitting in the high spin/high symmetry calculations and the amount of delocalization of wave functions from the BS calculations (see Results above). As the Fe−O−Fe is bent, two new CT transitions are introduced: $p_y \rightarrow d_{z^2}$ and $p_z \rightarrow d_{yz}$. The out of plane π ($p_x \rightarrow d_{xz}$ CT transition) still reflects the out of plane π superexchange pathway, but the other four possible CT transitions each reflect two pathways. This is illustrated in Figure 18. For example, the $p_y \rightarrow d_{yz}$ CT transition reflects both the in plane π superexchange pathway and a mixed $\pi-\sigma$ pathway. From inspection of the amount of each CT mixed into the GS for the bent structure in Table 10, the contribution of the out of plane pathway decreases slightly upon bending from 41% to 34%. The in plane π CT contribution, on the other hand, decreases from 44% to 28%. This net loss is compensated by the σ and mixed π/σ CT transitions. The σ CT mixing increases from 14% to 21%. This increase is due to the lower energy of the CT transition from 111 000 to 89 000 cm^{-1} (Table 10) and from the fact that it also reflects a π/σ exchange pathway. The two mixed π/σ CT transitions increase from 0% in the linear case (no overlap) to 4% and 12% in the bent case. The importance of the π/σ mixed pathway is consistent with the results of the analysis of the excited state LF splitting of the $^6A_1 \rightarrow {}^4A_1$ transition. The π/σ pathways as major pathways of exchange are necessary to account for the observed ferromagnetism in the $^4A_1$ excited state. Upon excitation ($^6A_1 \rightarrow {}^4A_1$) the mixed π/σ pathways are the only antiferromagnetic pathways whose contribution to exchange is expected to decrease in this excited state and thus promote ferromagnetism. Since the change in their contribution in the excited state makes a significant change in the exchange coupling, these pathways must make a sizable contribution to J. These mixed interactions only become important upon bending and help explain the lack of angle dependence observed in Fe−O−Fe dimer systems.[88,89]

Following ref 39, in the perturbation limit, the ground state exchange can be related to the VBCI parameters to obtain a physical picture of these effects. The ground state J can be written

$$-2J^{GS} = \frac{c h_{d_i p_j}^{\ 4}}{\Delta^2}\left(\frac{1}{U} + \frac{1}{(E_{DCT}/2)}\right) \qquad (25)$$

for each individual pathway, where c is a constant. The two major contributions to ground state exchange are the $h_{d_i p_j}$ and Δ values. The $h_{d_i p_j}$ can be thought of as a one-electron transition and depends on overlap. The Δ CT value is the energy of the state that mixes into the GS to stabilize it. For example, in the linear calculation, the $h_{d_z^2-p_z}$ is larger than that of the two π transitions. This larger $h_{d_i p_j}$ value is mitigated, though, by the larger CT energy Δ in the denominator of eq 25. Thus even though the $p_z-d_{z^2}$ overlap is large, because of the high energy of the transition, it is not as efficient at mixing into the GS as the π CT transitions. These concepts can also be easily extended to the bent case to explain the observed contributions to the GS exchange. The lower energy of the out of plane π and its larger h_{dp} value accounts for it being the CT state that mixes most into the excited state.

The lowest energy CT transitions at 20 500 cm^{-1}, assigned to the in plane π oxo $p_y \rightarrow$ Fe d_{yz} transition, is the CT transition subject to the largest excited state exchange which is the origin of its lower energy. The experimental singlet/triplet splitting for structure **2** with an angle of 165° is 4000 cm^{-1}. The value does not appear to decrease upon bending to 120°. Even though the triplet transition cannot be assigned with certainty in **1**, it is not observed within 4000 cm^{-1} of the singlet transition in Figure 2A. When the Fe−O−Fe angle is bent, the overlap of the oxo p_y orbital with the Fe d_{yz} orbitals decreases which would lead to a decrease in exchange, but the oxo p_y orbital now overlaps the Fe d_{z^2} orbital. This latter interaction compensates for the decrease. In the VBCI matrix this is described by the mixing of the oxo $p_y \rightarrow$ Fe d_{yz} transition with not only the Fe $d_{yz} \rightarrow$ Fe d_{yz} MMCT transition, but also with the Fe $d_{z^2} \rightarrow$ Fe d_{yz} MMCT transition (Figure 18). Even though this CT state experiences the largest ESAF, it is not the state which mixes the most with the GS (see above). This is due to a combination of effects as described in eq 25. The $h_{d_i p_j}$ value is smaller for this CT compared to the out of plane π CT transition, which makes a larger contribution to the GS. Also the Δ of the out of plane CT is lower in energy.

The above "inverted" assignment of the lowest energy CT transition as the oxo $p_y \rightarrow$ Fe d_{yz} transition accounts for the curious experimental features observed in this transition. The lowest energy oxo CT transitions features in Figure 2A, region II, are at least a factor of 2 lower in intensity than the higher energy CT transitions, i.e. the transitions assigned to the out of plane π CT transition at 26 000 and 28 400 cm^{-1} in Figure 3. Yet these lower energy features show the most Raman enhancement.[30,35,36] The decrease in absorption intensity for the $p_y \rightarrow d_{yz}$ transition relative to $p_x \rightarrow d_{xz}$ is due to the loss of overlap of the p_y orbital with the d_{yz} orbital. This can be seen in the contours shown in Figure 20 of the in plane oxo p_π orbital in the linear and bent case. Figure 20A shows the strong π overlap which decreases upon bending as in Figure 20B. The contour of the bent out-of-plane oxo p_π orbital (Figure 20C) still has

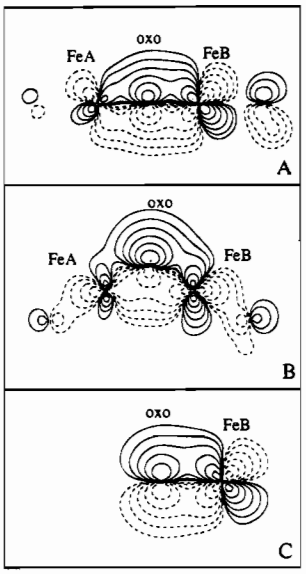

Figure 20. Broken symmetry contour plots of the oxo π bonding interactions for **1′** and **2′**. Part A gives the linear p_π bonding interactions which are identical for the in plane and out of plane orbitals. Part B gives the bent in plane π bonding interactions. Part C gives the bent out of plane bonding interactions. Note that the slice in part C is along the Fe−O bond and perpendicular to the Fe−O−Fe plane and thus only shows one Fe.

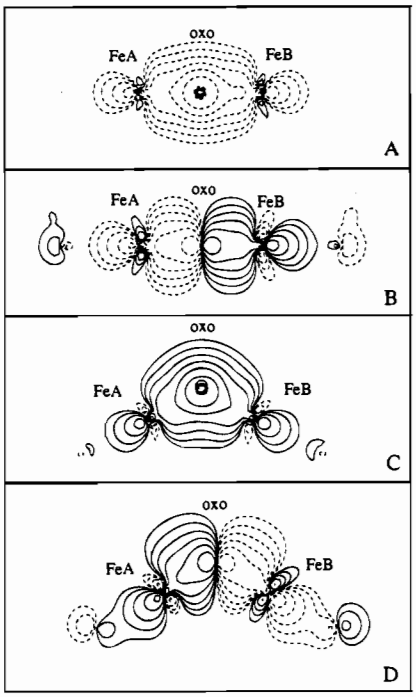

Figure 21. Broken symmetry contour plots of the oxo σ-bonding interactions for **1′** and **2′**. Parts A and B give the 2s and p_σ bonding interactions respectively for the linear dimer. Parts C and D give the 2s and p_σ bonding interactions for the bent dimer.

the strong π overlap. (Note that the orientation in Figure 20C differs from previous contours. The contour slice is taken along one of the Fe−O bonds and perpendicular to the Fe−O−Fe plane.) Figure 20B also shows some σ-bonding interaction with the d_{z^2} orbital. This results in stabilization of this orbital below that of the corresponding out of plane π orbital (Figure 15B). Since the acceptor d orbitals for the oxo $p_\pi \rightarrow d_{xz}$, d_{yz} are almost identical in energy and both involve π-antibonding interactions (see contours in Figure 16B, where the out of plane π interaction does not change upon bending, and Figure 16D), a transition from the more bonding orbital, the in plane p_π, should result in a larger distortion in the excited state and thus lead to greater resonance Raman enhancement.

The low energy of this transition also has a profound effect upon the intensity of the LF transitions. The increased intensity of the LF transitions in the dimeric unit over that of corresponding monomers is attributed to two intensity gaining mechanisms: a spin−orbit (SO) mechanism and an exchange mechanism. At low temperature where only the $S = 0$ component of the GS is populated, only the SO mechanism can lead to intensity enhancement. From the large intensity of the LF transitions (relative to a monomer transition) at low temperature, the SO intensity mechanism is the dominant mechanism. The spin orbit mixing is enhanced by the covalency of the Fe−oxo bond which leads to efficient mixing of the LF bands with these low energy CT transitions.

The results of this study can be used to address the nature of the Fe−oxo dimer bond. The main bonding interactions in the linear dimer involve the oxo bridging 2s, and oxo 2p orbitals. Figure 21A,B shows the delocalized strong σ bonding interactions of the oxo 2s and $2p_\sigma$ orbitals with the Fe's. The p_π bonding interactions were given previously in Figure 20A. The amount of oxo and Fe character in these orbitals and the breakdown of the contributions of the Fe into 3d, 4s, and 4p components is given Table 11A. While the Fe component mixed in the oxo 2p π orbitals is mainly d in character, the oxo 2s and the more covalent oxo $2p_\sigma$ orbitals contain a significant amount of Fe 4s and 4p character. Thus while the σ bonding to the Fe d orbitals with the oxo 2s and $2p_\sigma$ orbitals is partially canceled by the half-occupied antibonding d_{z^2} orbitals, the participation of the unoccupied Fe 4s and 4p orbitals leads to a much stronger σ bonding interaction for the Fe−oxo dimer unit and thus the short Fe−oxo bond. The experimental observation of the high intensity of the 1s → 3d X-ray absorption pre-edge feature in oxo-bridged Fe^{3+} dimers supports significant 4p mixing into the Fe 3d valence orbitals.[90] The lack of 4s and 4p character in the oxo 2p π orbitals indicates that upon first inspection, the bonding π interactions would be effectively canceled by the half-occupied π antibonding Fe d orbitals (d_{yz}, d_{xz}) orbitals. However, the oxo p_π orbitals are stabilized due to bonding interactions with both Fe ions, while each metal d electron has only one oxo antibonding interaction. The net greater π stabilization of the oxo p_π orbitals results in an additional π-bonding interaction. The effect of bending of the Fe−O−Fe unit is addressed in the contours in Figure 21C,D showing the oxo 2s and oxo $2p_\sigma$ orbitals respectively with Figure 20B,C showing the oxo p_π orbitals. The orbital breakdown in terms of oxo and Fe (3d, 4s, 4p) character is given in Table 11A. In the linear structure, the main bonding interaction is due to the oxo p_σ orbital. Upon bending, this orbital does not change markedly; while it loses some Fe 4p character, the oxo p_π (in plane) orbital picks up some Fe 4p character. There is however an increase in charge on the oxo upon bending.[91,92] This would help make the oxo more prone toward protonation in the bent structure. In summary, the strength of the Fe−oxo bond can be attributed to the strong σ bonding of the oxo p_σ orbital (Figure 21B, linear, and Figure 21D, bent) which is enhanced by participation of the unoccupied Fe 4s and 4p in bonding.

Since it has recently been shown that the active site of MMOH has a hydroxide bridge instead of an oxo bridge, it is

(90) Westre, T. G.; Hedman, B.; Hodgson, K. O.; Solomon, E. I. Unpublished results, 1994.
(91) The method developed by Case, et al. was used to determine the charge on the oxo bridge.
(92) Case, D. A.; Huynh, B. H.; Karplus, M. *J. Am. Chem. Soc.* **1979**, *101*, 4433−4453.

Table 11

A. Charge Breakdown and Fe Orbital Contributions for the Oxo Bonding Orbitals

	% oxo	% FeA	% FeB	sum Fe	FeA % s	FeA % p	FeA % d
			Linear Calculation (**2'**)				
oxo p_π (out of plane)	34	45	4	49	0	3	97
oxo p_π (out of plane)	35	44	4	48	1	2	96
oxo p_σ	51	25	23	48	20	30	50
oxo s	71	15	13	28	22	38	40
			Bent Calculation (**1'**)				
oxo p_π (out of plane)	14[a]	44	2	46	0	2	98
oxo p_π (in plane)	47	33	9	42	5	4	91
oxo p_σ	51	26	19	45	20	19	60
oxo s	70	16	14	30	21	37	42

B. Charge Breakdown and Fe Orbital Character of a Hydroxo-Bridged Fe^{3+} Dimer Calculation

	% O (hydroxo)	% FeA	% FeB	sum Fe	FeA % s	FeA % p	FeA % d
hydroxo p_π (out of plane)	31	20	10	30	0	8	92
hydroxo p_σ	35	30	12	42	11	3	86
hydroxo p_π (in plane)	40	9	6	15	0	29	71
hydroxo s	67	1	1	2	21	39	40

[a] The differences between linear and bent π orbitals is an artifact of the spin unrestricted calculations which makes the out of plane π orbital delocalized over a number of orbitals which is not observed experimentally.

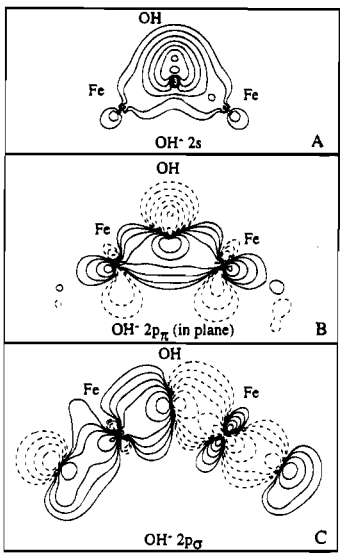

Figure 22. Broken symmetry contour plots of the bonding hydroxo orbitals of a hydroxo dimer calculation: (A) hydroxo 2s orbital; (B) hydroxo in plane p_π orbital; (C) hydroxo p_σ orbital.

important to consider the differences in bonding between oxo- and hydroxo-bridged binuclear ferric complexes. The contour plots of the hydroxide oxygen 2s, $2p_\sigma$, and $2p_\pi$ (in plane) orbitals from BS−SCF−Xα−SW calculations on a hydroxide-bridged ferric dimer are given in Figure 22.[93,94] The orbital breakdown of the amount of O (hydroxide) and Fe character in these orbitals is given in Table 11B. The hydroxo 2s orbital does not participate in bonding with the Fe orbitals and is instead involved in bonding with the H. The p_π (in plane) orbital shown in Figure 22B has now been stabilized below the oxo p_σ (Figure 22C) energetically due to bonding with the H as well. The Fe character of this orbital has also decreased leading to weaker π bonding compared to the oxo. The hydroxo p_σ has also lost some Fe character compared to the oxo bridge (Table 11A), and now possesses less 4p and 4s character. Since the 4s and 4p character of the oxo makes a key contribution to strong σ bonding, this also leads to a weaker σ bond. Overall, the OH should be a much weaker bridging ligand as experimentally indicated by the longer Fe−OH bond length and indirectly by the reduced exchange coupling ($J = -16$).[94]

Scheme 2

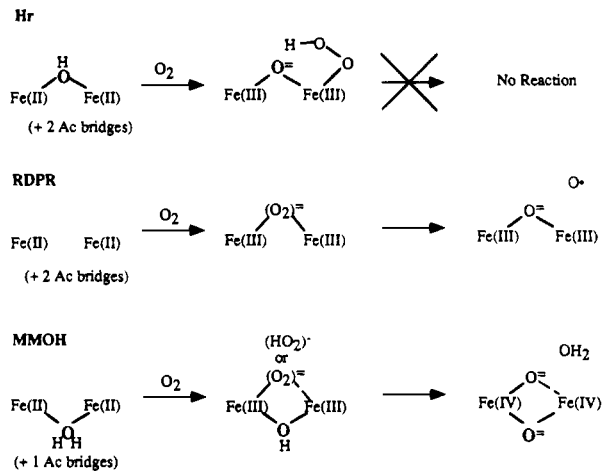

Relevance to the Reactivity of Binuclear Non-Heme Iron Proteins. These studies provide insight into the possible role of the strong iron−oxo dimer bond in the differences in reactivity of the different binuclear non-heme iron proteins. In Hr an oxo bridge exists in the peroxide bound oxy form. Since from our studies the oxo bridge forms an extremely stable bond, the presence of this bridge should help stabilize this species, oxyHr, toward further activation of peroxide as shown in Scheme 2. This behavior can be contrasted to that of RDPR and MMOH which are involved in O_2 activation at the peroxide binuclear ferric level. Like Hr, the binuclear ferric site of RDPR contains an oxo bridge. As first shown in MCD studies, there are open coordination positions at both irons in the Fe(II)−Fe(II) (active) form of RDPR; thus the possibility of the dioxygen intermediate (i.e. peroxide) bridging at the oxo site was

(93) Brown, C. A.; Solomon, E. I. Unpublished results, 1994. The Fe−OH distance was 1.96 Å, based on a crystal structure of the hydroxide bridged dimer. The sphere radius on each Fe was 2.80 Å.

(94) Armstrong, W. H.; Lippard, S. J. *J. Am. Chem. Soc.* **1984**, *106*, 4632−4633.

suggested.[95] Further evidence that the dioxygen intermediate bridges the two iron comes from rR studies which have recently demonstrated that the oxo bridge in the met form of RDPR comes from dioxygen.[96] This site should therefore be unstable toward formation of the strong Fe(III)−O^{2-}−Fe(III) unit. Thus heterolytic cleavage of the μ-peroxo intermediate would ensue to form the μ-oxo binuclear ferric unit and produce an oxygen radical then capable of generating the tyrosine radical necessary for catalysis[11,96] (Scheme 2). In contrast to Hr and RDPR which have an oxo bridge to stabilize the ferric species, in MMOH the binuclear ferric site does not appear to form an oxo bridge. Therefore reaction of the binuclear ferrous site with O_2 will produce a hydroxide bridged binuclear ferric−peroxy-bound intermediate which should be unstable toward further oxidation of the Fe(III) ions to form a (μ-oxo)ferryl species, i.e. the high valent intermediate identified as Compound Q[17] (Scheme 2). Thus the stability of the strong Fe−oxo dimeric unit should make a significant contribution to the different reactivities of these binuclear non-heme iron protein active sites.

The spectroscopic and theoretical analyses presented here have given significant insight into the nature of the oxo−Fe dimer bond and how this bonding dominates the absorption spectrum of these species. A complete spectral assignment has been made of all the LF and CT transitions in the model complexes studied. This assignment has been used to gain insight into the exchange coupling in the ground, LF, and oxo CT excited states. A VBCI analysis was used to account for the excited-state antiferromagnetism of the oxo CT transitions and relate this to the ground state antiferromagnetism. SCF−Xα−SW calculations have been used to complement the spectroscopic analysis and define specific contributions to the strength of the Fe−oxo dimer bond. This strong iron oxo dimer bond seems to provide significant insight into the differences in reactivity of the binuclear non-heme iron proteins with O_2. It will now be important to extend these studies to putative oxygen and high valent Fe intermediates to further understand the geometric and electronic structural contributions to the different reactivities of binuclear non-heme iron proteins.

Acknowledgment. This work was supported by the NSF-Biophysics Program Grant MCB 9316768 (E.I.S.), by the donors of the Petroleum Research Fund, administered by the American Chemical Society, Grant PRF-28948B (R.L.M.), and by the NSF Grant CHE-9213251 (R.L.M.). R.L.M. would like to thank Glenn W. Shaffer and Lisa Christopher for their help in obtaining the reflectance data. C.A.B. and E.I.S. would like to thank Prof. David Richardson for recording some of the data on structure **2**.

Supplementary Material Available: Tables of the input parameters for the SCF−Xα−SW calculations, a table of the ground state valence bond wave functions, two VBCI matrices ($^1A_1$) and ($^1B_2$) for the bent dimer, a figure of variable temperature mull MCD data for **2**, and a figure of the raw specular reflectance data are available as supplementary material (9 pages). Ordering information is given on any current masthead page.

IC941249I

(95) Solomon, E. I.; Zhang, Y. *Acc. Chem. Res.* **1992**, *25*, 343−352.
(96) Ling, J.; Sahlin, M.; Sjöberg, B.-M.; Loehr, T. M.; Sanders-Loehr, J. *J. Biol. Chem.* **1994**, *269*, 5595−5601.